NORTHWESTERN UNIVERSITY

Study of CP Violation in $B_s^0 \to J/\psi\phi$ Decays at DØ

A DISSERTATION

SUBMITTED TO THE GRADUATE SCHOOL
IN PARTIAL FULFILLMENT OF THE REQUIREMENTS

for the degree

DOCTOR OF PHILOSOPHY

Field of Physics and Astronomy

By

Derek A. Strom

EVANSTON, ILLINOIS

December 2008

ABSTRACT

Study of CP Violation in $B_s^0 \to J/\psi\phi$ Decays at DØ

Derek A. Strom

In a universe dominated by matter, the source of CP violation may explain one of the greatest mysteries in particle physics: what happened to the antimatter? The Standard Model successfully describes CP violation in the B^+ and B_d^0 systems, yet insufficiently accounts for the observed matter-antimatter asymmetry. The Standard Model predicts a small value of CP violation in the B_s^0 meson system, which has only recently been experimentally tested. A measurement of large, anomalous CP violation in the B_s^0 system would be a clear indication of new physics sources beyond the Standard Model. This dissertation describes a study of CP violation in approximately 2000 $B_s^0 \to J/\psi\phi$ decays reconstructed in a 2.8 fb^{-1} data sample collected by the DØ Run II detector at Fermi National Accelerator Laboratory in Batavia, Illinois. This data was provided by $p\bar{p}$ collisions at $\sqrt{s} = 1.96$ TeV delivered by the Tevatron accelerator between April 2002 and August 2007. Flavor-tagged $B_s^0 \to J/\psi(\mu^+\mu^-)\phi(K^+K^-)$ decays and an angular analysis are used to study the time evolution of the final state angular distributions. From this analysis, we measure the width difference between the heavy and light mass eigenstates, B_s^L and B_s^H, to be $\Delta\Gamma_s = 0.19 \pm 0.07$ and the CP-violating phase $\phi_s = -0.57^{+0.24}_{-0.30}$.

Acknowledgements

To begin, I would like to express sincere gratitude to my academic advisor, David Buchholz. Thank you for your constant encouragement, insightful guidance, and caring mentoring throughout this endeavor! You have exposed me to the awesome fascinations of particle physics, and provided me the opportunity and freedom to explore this exciting field. The countless things you have taught me about physics, particle detectors, and most importantly, myself, will surely be carried with me long past my graduate years.

To my friends and fellow graduate students at Northwestern, especially Tim Andeen, Meghan Anzelc, Sahal Yacoob, and Sungwoo Youn, I am indebted to your eagerness to help, endless support, and thoughtful insight you have provided over the years. I feel great honor to have shared in this experience with each of you, and am grateful for our lasting companionship.

Dedicated thanks is due to my friend and DØ colleague, Avdhesh Chandra, who provided significant guidance in this analysis effort. You have taught me so much about the fine details of physics analysis and the value of hard work. I have greatly enjoyed our time working together, and cannot express enough thankfulness for the amount of support and patience you have offered.

I would like to thank Heidi Schellman, Andre de Gouvea, and Brendan Casey for your role as teacher, advisor, and mentor. You each have contributed significantly to my academic development, and I appreciate your sincere dedication to students.

I have found great joy while working on the DØ Experiment, which is due largely to the wonderful people I have worked with most closely. To the entire Silicon Operations Group, especially Masato Aoki, Linda Bagby, Sergey Burdin, Satish Desai, George Ginther, Kazu

Hanagaki, Kristian Harder, Marvin Johnson, Mike Kirby, Ron Lipton, Andrei Nomerotski, Dmitri Tsybychev, Mike Utes, and Michele Weber, I am grateful for the opportunity to have worked with such a dedicated, passionate, and inspiring team of researchers. You each have taught me invaluable skills, aided in my professional development, and clearly demonstrated that when you put your mind to something, anything is possible.

Friendships, new and old, are invaluable to me, and I would like to especially thank Bob Tilden, Justin List, Greg Faleskin, Pete Olson, Janeane Koebbe, Matt Wetstein, Dan Duggan, Dan Krop, and the Boomers softball team for your cordial support and entertaining breaks from the rigors of research.

To the many teachers who have instructed me down this path, especially my high school physics teacher Paula Mytych and my undergraduate professors Cecilia Vogel, David Renneke, Bruce McCart, Lee Carkner, and Jon Clauss, I thank you for the inspiration you have provided me, and for your commitment to education.

To my parents, Leland and Twyla, I give deep thanks for providing me the freedom and encouragement to pursue a childhood dream. This dissertation is a product of your devotion to my education, and for that I am blessed. From the beginning, you have been all things: teacher, supporter, cheering squad, family, and friend. Most importantly, your love has guided me at every stage, and I thank you for all you have done to prepare me for this accomplishment.

To my siblings, Amber and Tyler, I thank you for your constant well-wishes and blessings over the years.

Finally, I would like to thank Kim, my wife and eternal love, for whom this dissertation is dedicated. Your unwavering support has been there throughout, and you are the source of all my happiness and joy. I truly could not have met and fallen in love with a more beautiful, intelligent, affectionate, and devoted woman.

I don't paint things. I only paint the difference between things. – Henri Matisse

Table of Contents

List of Tables

List of Figures

CHAPTER 1

Introduction

Modern particle physics explores properties of nature at its smallest and fastest scale. It seeks to experimentally discover and theoretically describe the elementary constituents of matter and the forces through which they interact. Through a continuous exchange of information between experimental and theoretical developments, an elegant mathematical formulation of particle physics has emerged. This theory, known as the Standard Model, describes elementary particles and their interactions with astounding precision. Despite its current success, the Standard Model leaves some pressing questions regarding the nature of the universe unresolved.

It is well understood in particle physics that for every fundamental matter particle there exists an antimatter particle, or antiparticle, with equal mass but opposite internal quantum numbers. For example, the positron is the antiparticle companion to the electron. Both have mass equal to 0.511 MeV/c^2, but as the name implies the positron has a positive electric charge, while the electron has a negative charge. More subtle differences between particles and antiparticles may reveal insight to one of the most intriguing questions in particle physics: why is the universe presently dominated by particles?

It is thought particles and antiparticles existed in equal numbers immediately following the creation of the universe. Yet it appears from observational data that the universe has evolved into a state where the number of particles greatly exceeds the number of antiparticles. The universe, it seems, has as an inherit preference for particles over antiparticles. What, then, became of the antiparticles? What underlying mechanism is responsible for this particle-antiparticle asymmetry? These are questions at the forefront of particle physics research, and are being addressed at particle physics laboratories today.

This asymmetry suggests the laws of physics are different for particles than they are for antiparticles. This is known to be true, in fact, and is manifested through the violation of a certain symmetry known as CP, the combined charge conjugation (C) and parity (P) symmetry. A symmetry refers to a property of a particular system that remains unchanged, or conserved, as it undergoes a specific transformation. The transformation can be many things: translations through space or time, rotations about an axis, or in this case the combined conversion of a particle into an antiparticle (C) and reversal of spatial coordinates (P), as if one were looking into a mirror.

Each symmetry of a system implies the conservation of a physical property of that system. This is known as Noether's theorem [**1**]. For example, linear momentum is the conserved property corresponding to the symmetry of translations in space. More familiarly this is known as conservation of linear momentum. Similarly, conservation of energy corresponds to the symmetry of translations in time. As a consequence of Noether's theorem, the same experiment can be performed at two different points in space under the exact same laws of physics (conservation of linear momentum). The same holds true for similar experiments performed at two different points in time (conservation of energy).

If CP were a conserved symmetry, that is there were no violation of the symmetry, every reaction that produces a particle would be accompanied by a reaction which produces its antiparticle at precisely the same rate, and hence no particle-antiparticle asymmetry. CP, as it turns out, is not a conserved symmetry. Experimental evidence demonstrates that it is violated in certain particle systems, namely the neutral kaon and B meson systems. That CP violation is believed to be one of the necessary conditions for the generation of the observed particle-antiparticle asymmetry was first introduced by Andrei Sakharov in 1967 [**2**].

One of the great successes of the Standard Model is that it provides a description, known as the Cabibbo-Kobayashi-Maskawa (CKM) mechanism [**3**], that allows a small amount of CP violation in these neutral meson systems. A problem arises, however, when noting that the amount of CP violation allowed by the Standard Model is insufficient to account for the level of asymmetry observed in the universe by many orders of magnitude. Our best understanding of CP violation and the subtle differences between particles and antiparticles is incomplete. We must, therefore, further investigate systems which exhibit CP-violating effects. Of particular interest are systems in which CP violation is predicted to be small and experimental tests for large, anomalous CP violation not described by the Standard Model can be made. For this, we examine the B_s^0 meson system.

CP violation in the B_s^0 system is described within the framework of the Standard Model by the 3 × 3 CKM quark mixing matrix. It has three real parameters and one complex phase, ϕ_s, which is the only source of CP violation in the Standard Model. The Standard Model predicts ϕ_s to be small ($\phi_s^{SM} \sim 0.04$) in the B_s^0 system. The measurement of a large ϕ_s, therefore, would be a clear indication of new physics beyond the Standard Model, and may provide insight into the particle-antiparticle asymmetry dilemma.

The B_s^0 meson is composed of one b-type quark (also known as the "bottom" or "beauty" quark) and one s-type quark (the "strange" quark). The convention used throughout this dissertation is that a B_s^0 meson is composed of an anti b-quark and an s-quark ($\bar{b}$, s), while its charge conjugate state $\bar{B}_s^0$ is composed of a b-quark and an anti s-quark (b, $\bar{s}$). The B_s^0 meson exhibits an interesting feature, called mixing, allowing for a matter B_s^0 meson to change into an antimatter $\bar{B}_s^0$ meson, and back again. In fact, the frequency of this mixing has recently been measured to be roughly three trillion times per second! Since mixing in the B_s^0 system introduces continuous conversions between matter and antimatter, it is the ideal place to probe for CP violation.

Mixing in the B_s^0 system is related to the two physically observable mass eigenstates, called the Light (B_s^L) and Heavy (B_s^H), which are different from the flavor eigenstates (B_s^0 and $\bar{B}_s^0$). The Light and Heavy states have distinct masses, denoted as m_L and m_H. The frequency of oscillation, Δm_s, is related to the mass splitting between these eigenstates: $\Delta m_s \equiv m_H - m_L$. They also have distinct widths, which are related to their lifetimes as $\Gamma_L = 1/\tau_L$ and $\Gamma_H = 1/\tau_H$. From these widths a width difference relation can be formed: $\Delta\Gamma_s \equiv \Gamma_L - \Gamma_H$.

The experiment described in this dissertation seeks to measure the CP-violating phase ϕ_s in the B_s^0 meson system using decays of the type $B_s^0 \to J/\psi(\mu^+\mu^-)\phi(K^+K^-)$. Since mixing is known to occur in the B_s^0 system, and both B_s^0 and $\bar{B}_s^0$ decay to the $J/\psi\phi$ final state, interference can enter between the direct decay ($B_s^0 \to J/\psi\phi$) and the decay involving mixing ($B_s^0 \to \bar{B}_s^0 \to J/\psi\phi$). This interference provides a sensitive probe for ϕ_s.

One complication in the analysis is that the final state products are not pure CP eigenstates, but rather an admixture of CP-even ($\sim 75\%$) and CP-odd ($\sim 25\%$) components. By assuming CP is conserved in the B_s^0 system ($\phi_s = 0$) for this experiment, the Light and Heavy mass eigenstates are expected to be CP eigenstates, such that B_s^L is CP-even and B_s^H is CP-odd. An angular analysis of the final state particles helps disentangle the CP components into their separate states, and thus allows the measurement of the distinct Light and Heavy widths. A combined opposite and same-side flavor tag is applied to determine the initial state of the B_s^0 meson (whether it is produced as a B_s^0 or $\bar{B}_s^0$ at time $t = 0$), which further increases the sensitivity to ϕ_s.

This experiment was performed at the DØ detector at Fermi National Accelerator Laboratory in Batavia, Illinois where the Tevatron accelerator provides proton-antiproton collisions at $\sqrt{s} = 1.96$ TeV. It uses a 2.8 fb^{-1} data set collected by the DØ Run II detector between April 2002 and August 2007. The CP-violating phase in the B_s^0 meson system is experimentally measured to be $\phi_s = -0.57^{+0.24}_{-0.30}$, which is in disagreement with the Standard Model prediction at the level of 1.7σ. These results were published in Physical Review Letters [**4**].

The dissertation is organized as follows: Chapter two describes the main theoretical points relevant to this study. Chapter three provides a brief description of the Fermilab Tevatron accelerator and the DØ Run II detector. Chapter four discusses the analysis method employed using the angular analysis, flavor-tagging, and a likelihood fit to extract information on the width difference $\Delta\Gamma_s$ and CP-violating phase ϕ_s. Chapter five concludes this dissertation with a summary of the main results.

CHAPTER 2

Theory

2.1. Introduction

In 1972 theorists Makoto Kobayashi and Toshihide Maskawa, extending previous work by Nicola Cabibbo, predicted the existence of a third generation of heavy quarks[1] [**3**]. A seemingly unnecessary description of particle physics at the time, their paper was largely ignored. Nevertheless, the prediction was necessary to complete their new theoretical description of CP violation within the framework of the Standard Model (SM).

CP is the combined charge conjugation (C) and parity (P) operation. If CP were conserved, all physical processes in nature would occur in precisely the same manner if all particles were transformed into their antiparticles ($C|p\rangle = |\bar{p}\rangle$), and all spatial coordinates were reversed ($P|x,y,z\rangle = |-x,-y,-z\rangle$). The fact nature does not observe this in some processes means that the CP symmetry is violated. CP violation was first observed in 1964 in weak decays in the neutral kaon system.

Neutral kaons are observed as two states, $|K_1\rangle$ and $|K_2\rangle$, which are mixtures of the flavor eigenstates $|K^0\rangle$ and $|\bar{K^0}\rangle$:

$$\begin{aligned} |K_1\rangle &= p|K^0\rangle - q|\bar{K^0}\rangle, \\ |K_2\rangle &= q|K^0\rangle + p|\bar{K^0}\rangle. \end{aligned} \tag{2.1}$$

---

[1] At the time, only three quarks were known to exist: the up and down quarks which make up most ordinary matter in the universe, and the strange quark.

Assuming CP is conserved in this system, $q = p = 1/\sqrt{2}$ and $|K_1\rangle$ and $|K_2\rangle$ are CP eigenstates, such that:

$$\begin{aligned} CP|K_1\rangle &= +|K_1\rangle, \\ CP|K_2\rangle &= -|K_2\rangle. \end{aligned} \tag{2.2}$$

Under this assumption, K_1 would only be allowed to decay to CP-even final states, such as $\pi^+\pi^-$, while K_2 would be restricted to CP-odd three body final states. The lifetime of the K_1 and K_2 states[2] are found [**5**] to be consistent with this model:

$$\begin{aligned} \tau(K_1) &= (0.8953 \pm 0.0005) \times 10^{-10} s, \\ \tau(K_2) &= (5.116 \pm 0.020) \times 10^{-8} s. \end{aligned} \tag{2.3}$$

Then, in a landmark experiment in 1964 at Brookhaven National Laboratory, Christenson, Cronin, Fitch, and Turlay observed the K_2 particle occasionally decaying ($\sim 0.2\%$ of the time) to CP-even $\pi^+\pi^-$ final states, providing the first evidence for CP violation [**6**]. Separately, C and P symmetries were known to be broken in physical processes. Violation of the combined CP symmetry came as a big surprise, however. What mechanism was responsible for breaking the CP symmetry? Why was it broken in such a small amount, and in only one system? There was no theoretical explanation for such surprising behavior. A framework did not emerge until 1972, when Kobayashi and Maskawa released their paper. Unfortunately, there was no other system exhibiting this feature to make further experimental studies at the time.

Then in 1977, Leon Lederman (spokesperson of Experiment 288 at the National Accelerator Laboratory[3]) lead a team that discovered the Upsilon meson[4] [**7**], which he subsequently referred to as "one of the most expected surprises in particle physics". The discovery of the Upsilon and its associated long lived b-quark confirmed the existence of

---

[2] The K_1 and K_2 were later renamed the K_S (K-short) and K_L (K-long) to identify them by their lifetimes.

[3] It has since been named Fermi National Accelerator Laboratory, in honor of Italian physicist Enrico Fermi.

[4] The Upsilon is a quarkonium state (bottomonium) comprised of a quark and its own antiquark pair (in this case $b\bar{b}$).

the third generation of quarks predicted by Kobayashi and Maskawa, and opened a new window of opportunity for the study of CP violation. It was thought neutral B-mesons would exhibit similar behavior to their lighter kaon counterparts, thus enabling further studies of these CP-violating effects.

Evidence did not come quickly, however, as it took roughly four decades from the time CP violation was first detected in the kaon system to confirm its presence in the B meson system. Experiments dedicated to producing B mesons (B "factories") have now provided measurements in agreement with the theoretical predictions given by Kobayashi and Maskawa. In honor of their theoretical work, Kobayashi and Maskawa were awarded the 2008 Nobel Prize in Physics. The relevant features of this theoretical framework for a study of CP violation in the relatively uncharted B_s^0 meson system is presented here.

2.2. The Standard Model

The Standard Model[5] (SM) is a theoretical framework that describes interactions between the known elementary particles in nature. These particles can be broadly cast into two groups: those with half-integer spin (fermions) and those with integer spin (bosons). Quarks and leptons are two classes of fermions[6], and can be simply arranged into three generations according to their mass. Quarks can bind into groups of three (qqq or $\bar{q}\bar{q}\bar{q}$) called baryons, or quark-antiquark pairs ($q\bar{q}$) called mesons[7].

General properties of the quarks and leptons are listed in tables 2.1 and 2.2. All of the visible matter in the universe is made of only the first generation of particles[8]. Today, heavier generation particles must be created and studied at accelerator laboratories, such as the one described in the next chapter.

---

[5] This description follows texts [**8**], [**9**] and [**10**].

[6] For each quark and lepton particle there is an antiparticle counterpart, with the same mass and all internal quantum numbers (charge, baryon number, strangeness, etc.) reversed. The positron, the antiparticle of the electron, was the first known antiparticle. It was postulated by Paul Dirac in 1928, and discovered by Carl Anderson in 1932.

[7] Baryons and mesons are subsets of the broader class of bound quark states, called hadrons.

[8] Protons (uud), neutrons (ddu), and electrons make up all of the known elements.

Quarks (spin=$\frac{1}{2}$)	Symbol	Charge	Mass (MeV/c^2)	Generation
up	u	2/3	$1.5 - 5$	1
down	d	$-1/3$	$3 - 9$	
charm	c	2/3	$(1.0 - 1.4) \times 10^3$	2
strange	s	$-1/3$	$60 - 170$	
top	t	2/3	$(178.0 \pm 4.3) \times 10^3$	3
bottom	b	$-1/3$	$(4.0 - 4.5) \times 10^3$	

Table 2.1. The Elemental Quarks.

Leptons (spin=$\frac{1}{2}$)	Symbol	Charge	Mass (MeV/c^2	Generation
electron	e	-1	0.511	1
electron neutrino	ν_e	0	$< 3 \times 10^{-6}$	
muon	μ	-1	105.66	2
muon neutrino	ν_μ	0	< 0.19	
tau	τ	-1	1776.99 ± 0.29	3
tau neutrino	ν_τ	0	< 18.2	

Table 2.2. The Elemental Leptons

Gauge bosons, listed in table 2.3, are responsible for mediating forces, three of which are described by the SM: the weak, electromagnetic, and strong forces. Gravity is not included in the SM description because its effects on quarks and leptons are too weak to be measured. The massive $W^{\pm}$ and Z^0 bosons mediate the weak force between particles of different flavor (quarks and leptons), the massless photon mediates the electromagnetic force between electrically charged particles, and 8 gluons mediate the strong force between color charged particles (quarks). The undiscovered graviton mediates the gravitational force. This chapter will focus on the charged weak and strong quark interactions.

Bosons (spin=0)	Force	Range (cm)	Strength	Mass (GeV/c^2)	Charge	Spin
graviton	Gravity	infinite	10^{-40}	0	0	2
W^+ W^- Z^o	Weak	10^{-16}	10^{-6}	80.4 80.4 91.2	1 -1 0	1 1 1
γ	EM	infinite	10^{-2}	0	0	1
gluons	Strong	10^{-13}	1	0	0	1

Table 2.3. The Gauge Bosons.

2.3. CP Violation and the Unitary CKM Matrix

The discussion of CP violation and the CKM matrix begins with an examination of the charged-current weak interactions involving the coupling of the $W^{\pm}$ boson to quarks. An example of this process is found in neutron beta decay

$$n \rightarrow p + e + \bar{\nu}_e$$

where a d quark in the neutron decays to a u quark by emitting a W^-, which immediately decays to an electron and electron-type antineutrino, as shown in Fig. 2.1.

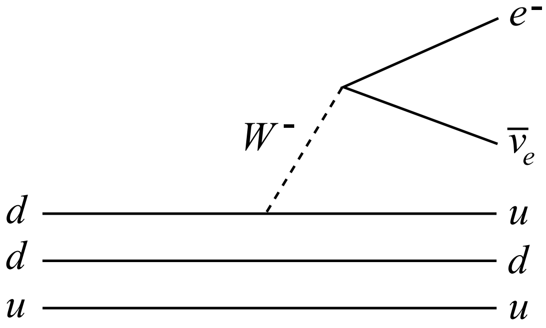

Figure 2.1. A Feynman diagram of the charged-current interaction in neutron beta decay.

Charged-current weak transitions in quarks are not restricted to their own generation, and can occur between any of the three quark flavors with different charge, as illustrated in Fig. 2.2. This is referred to as flavor changing.

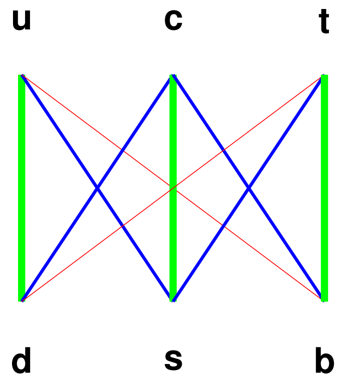

Figure 2.2. An Illustration showing allowed quark transitions and relative strengths, where allowed transitions are denoted by green (thick) lines, suppressed transistions by blue (medium) lines, and highly suppressed transitions by red (thin) lines.

Nine weak couplings between quarks with positive charge (u, c, t) and those with negative charge (d, s, b) completely describe the couplings of these quark transitions, and can be represented as a 3×3 matrix, known as the Cabibbo-Kobayashi-Maskawa (CKM) quark mixing matrix. This matrix is expressed in its most general form in Eq. 2.4, where V_{ij} denotes the coupling between quarks $i = u, c, t$ and $j = d, s, b$.

$$V_{CKM} = \begin{pmatrix} V_{ud} & V_{us} & V_{ub} \\ V_{cd} & V_{cs} & V_{cb} \\ V_{td} & V_{ts} & V_{tb} \end{pmatrix} \tag{2.4}$$

The CKM matrix can also be represented as a rotation from the weak flavor eigenstates (d', s', b') to the strong mass eigenstates (d, s, b).

$$\begin{pmatrix} d' \\ s' \\ b' \end{pmatrix} = \begin{pmatrix} V_{ud} & V_{us} & V_{ub} \\ V_{cd} & V_{cs} & V_{cb} \\ V_{td} & V_{ts} & V_{tb} \end{pmatrix} \cdot \begin{pmatrix} d \\ s \\ b \end{pmatrix} \tag{2.5}$$

Assuming three generations of quarks, the CKM matrix contains a complete set of transformations and is unitary: $VV^\dagger = 1$. After removing unphysical phases, it can be described by four parameters: three quark mixing rotation angles and one complex phase responsible for CP violation in the SM. The following is the standard representation:

$$V = \begin{pmatrix} c_{12}c_{13} & s_{12}c_{13} & s_{13}e^{-i\delta} \\ -s_{12}c_{23} - c_{12}s_{23}s_{13}e^{i\delta} & c_{12}c_{23} - s_{12}s_{23}s_{13}e^{i\delta} & s_{23}c_{13} \\ s_{12}s_{23} - c_{12}c_{23}s_{13}e^{i\delta} & -c_{12}s_{23} - s_{12}c_{23}s_{13}e^{i\delta} & c_{23}c_{13} \end{pmatrix}, \tag{2.6}$$

where the three angles are denoted as $s_{ij} = \sin\theta_{ij}$, $c_{ij} = \cos\theta_{ij}$, $i < j = 1, 2, 3$ and the complex phase δ is responsible for all CP-violating effects in flavor-changing processes in the SM.

The experimental observation that interactions between quarks of the same generation are found to be strongly favored, while those between different generations are suppressed is equivalent to saying diagonal elements of the CKM matrix are nearly equal to one, while off-diagonal elements become smaller the farther they are from diagonal. The Wolfenstein parameterization [**11**] of the CKM matrix, expanded in powers of four independent terms (λ, A, ρ, and η) as shown in Eq. 2.7, illustrates this observation. Experiments have determined $\lambda \approx 0.22$, $A \approx 0.8$, and $\sqrt{\rho^2 + \eta^2} \approx 0.4$. In this representation, CP violation is given by a non-zero value of η to order λ^3.

$$V = \begin{pmatrix} 1 - \frac{1}{2}\lambda^2 & \lambda & A\lambda^3(\rho - i\eta) \\ -\lambda & 1 - \frac{1}{2}\lambda^2 & A\lambda^2 \\ A\lambda^3(1 - \rho - i\eta) & -A\lambda^2 & 1 \end{pmatrix} + \mathcal{O}(\lambda^4)\,. \tag{2.7}$$

The unitary condition of the CKM matrix results in a total of twelve equations, six of which are orthogonality relations:

$$
\begin{aligned}
V_{ud}^*V_{cd} + V_{us}^*V_{cs} + V_{ub}^*V_{cb} &= 0, & (2.8)\\
V_{ud}^*V_{td} + V_{us}^*V_{ts} + V_{ub}^*V_{tb} &= 0, & (2.9)\\
V_{cd}^*V_{td} + V_{cs}^*V_{ts} + V_{cb}^*V_{tb} &= 0, & (2.10)\\
V_{ud}V_{us}^* + V_{cd}V_{cs}^* + V_{td}V_{ts}^* &= 0, & (2.11)\\
V_{ud}V_{ub}^* + V_{cd}V_{cb}^* + V_{td}V_{tb}^* &= 0, & (2.12)\\
V_{us}V_{ub}^* + V_{cs}V_{cb}^* + V_{ts}V_{tb}^* &= 0. & (2.13)
\end{aligned}
$$

These six relations can be represented as triangles which all have the same area [**12**]. Only two of these triangles have sides with comparable length. The other four triangles are "squashed", having one side considerably smaller than the other two, as in the case of the triangle related to the B_s^0 meson. The following equations provide the most useful restrictions on the matrix elements:

$$
\begin{aligned}
V_{ud}\,V_{ub}^* + V_{cd}\,V_{cb}^* + V_{td}\,V_{tb}^* &= 0, & (2.14)\\
V_{ud}^*\,V_{td} + V_{us}^*\,V_{ts} + V_{ub}^*\,V_{tb} &= 0. & (2.15)
\end{aligned}
$$

These conditions are represented as normalized triangles in the complex plane in Fig. 2.3. In the Wolfenstein parameterization, the triangles are identical up to λ^3 and are referred to as *the* unitary triangle. One side lies on the real axis from points (0,0) to (1,0) in the complex $(\bar{\rho}, \bar{\eta})$ plane, as shown in the top triangle in Fig. 2.3. The apex of the triangle is at point $(\bar{\rho}, \bar{\eta})$, where

$$
\begin{aligned}
\bar{\rho} &= \rho(1 - \lambda^2/2), & (2.16)\\
\bar{\eta} &= \eta(1 - \lambda^2/2). & (2.17)
\end{aligned}
$$

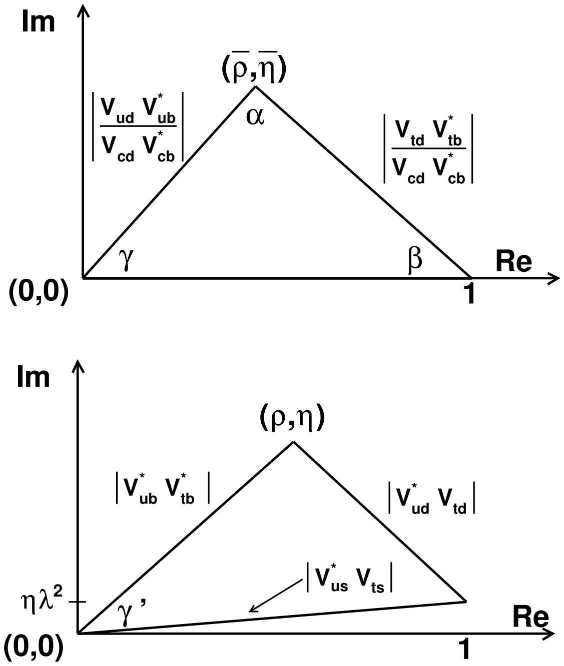

Figure 2.3. The rescaled unitary triangles formed from the orthogonal relations given in Eqs. 2.14 (top) and 2.15 (bottom).

CP violation is generally discussed in terms of this plane.

The angles of the unitary triangle are defined in terms of the matrix elements as,

$$\begin{aligned} \alpha &\equiv \phi_2 \equiv \arg\left[-\frac{V_{td}V^*_{tb}}{V_{ud}V^*_{ub}}\right], \\ \beta &\equiv \phi_1 \equiv \arg\left[-\frac{V_{cd}V^*_{cb}}{V_{td}V^*_{tb}}\right], \qquad (2.18) \\ \gamma &\equiv \phi_3 \equiv \arg\left[-\frac{V_{ud}V^*_{ub}}{V_{cd}V^*_{cb}}\right], \end{aligned}$$

or in terms of $\bar{\rho}$ and $\bar{\eta}$ as

$$\begin{aligned}\alpha &= \tan^{-1}\left(\frac{\bar{\eta}}{\bar{\eta}^2+\bar{\rho}(\bar{\rho}-1)}\right),\\ \beta &= \tan^{-1}\left(\frac{\bar{\eta}}{1-\bar{\rho}}\right),\\ \gamma &= \tan^{-1}\left(\frac{\bar{\eta}}{\bar{\rho}}\right).\end{aligned} \tag{2.19}$$

The unitary triangle is a useful representation of the CKM mechanism. The CKM matrix elements are fundamental parameters of the SM and it is important to measure them precisely. Today's high energy experiments seek to verify the SM picture of CP violation, which can be achieved by separately measuring each side and angle of the unitary triangles in an effort to over constrain them. For the SM description to be valid, these measurements should agree with one another. Processes not described by the SM would be apparent if two sides of the triangle were found not to return to the same point, or "close". The 90% confidence limits on the magnitude of the CKM matrix elements, using tree level[9] constraints and unitarity, are given in Equation 2.20.

$$V^{SM}_{CKM} = \begin{pmatrix} 0.9739-0.9751 & 0.221-0.227 & 0.0029-0.0045 \\ 0.221-0.227 & 0.9730-0.9744 & 0.039-0.044 \\ 0.0048-0.014 & 0.037-0.043 & 0.9990-0.9992 \end{pmatrix} \tag{2.20}$$

The most recent experimental results [**5**], showing agreement with the SM predictions[10], are given in Eq. 2.21.

$$V^{exp}_{CKM} = \begin{pmatrix} 0.97419\pm0.00022 & 0.2257\pm0.0010 & 0.00359\pm0.00016 \\ 0.2256\pm0.0010 & 0.97334\pm0.00023 & 0.0415^{+0.0010}_{-0.0011} \\ 0.00874^{+0.00026}_{-0.00037} & 0.0407\pm0.0010 & 0.999133^{+0.000044}_{-0.000043} \end{pmatrix} \tag{2.21}$$

---

[9] Feynman diagrams come in two varietys: tree level diagrams, in which particle interactions are connected simply, like branches of a tree, and loop diagrams which involve virtual short-lived particles.

[10] Only $|V_{ub}|$ and $|V_{td}|$ have theoretical uncertainty comparable to the theoretical value.

2.4. B_s^0 Lifetime

The spectator quark model, where interfering effects from nearby "spectator" quarks are neglected, is the simplest way to calculate B-meson lifetimes. An example is shown in Fig. 2.4, where a b-quark decays to a c-quark through the weak interaction with a virtual W boson. The b-quark couples predominantly to the c-quark and its lifetime depends on the CKM matrix element V_{cb}.

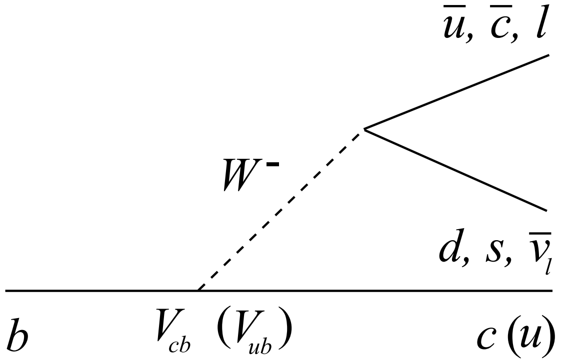

Figure 2.4. A Feynman diagram showing a b-quark decaying to a lighter $c(u)$-quark.

According to the spectator model, all B hadrons should have the same lifetime. Experimentally, however, it is observed that they have significantly different lifetimes, as given in table 2.4 (from the Heavy Flavor Averaging Group (HFAG) [**13**]). The B hadron lifetimes are observed to have the following relationship:
$\tau(B_c^+)^{11} < \tau(\Lambda_b^0) < \tau(B_s^0) < \tau(B_d^0) < \tau(B_u^+)$.

This demonstrates that spectator model calculations are not sufficient to describe the decay of B hadrons. For higher precision, it is necessary to include QCD effects into the spectator model. One approach which successfully describes the decay of hadrons containing a heavy quark ($m_Q >> \Lambda_{QCD} \sim 0.2$ GeV) and a light quark is the Heavy Quark Effective Theory(HQET) [**14**] [**15**].

---

[11] The B_c has a significantly shorter lifetime because both quarks can decay via the weak interaction.

B hadron	Average lifetime (in pico second)
B^+	1.639 ± 0.009
B^0	1.530 ± 0.008
B_s^0 ($\rightarrow$ flavor specific)	1.456 ± 0.030
B_s^0 ($\rightarrow J/\psi\phi$)	1.477 ± 0.046
B_s^0 $(1/\bar{\Gamma}_s)$	$1.478^{+0.020}_{-0.022}$
B_c^+	0.461 ± 0.036
Λ_b^0	1.379 ± 0.051

Table 2.4. Summary of B hadron lifetimes, as given by HFAG [**13**].

In the HQET the Lagrangian is expanded in powers of $1/m_Q$, usually referred to as the Operator Product Expansion (OPE). HQET is most effective at describing bound states containing a b-quark, but also works for those containing a c-quark, although it requires additional corrections due to the lower mass of the c-quark. The theory does not apply to top quarks since they decay before forming bound states.

The leading term in the $1/m_Q$ expansion describes the decay of a free quark, producing the same results as the spectator model. Differences in the B-meson lifetimes appear in the $1/m_Q^3$. A summary of HQET predictions of the B hadron lifetime ratios and their experimental values are given in Table 2.5.

Ratios	HFAG value	HQET predicted range
$\tau(B_u^+)/\tau(B_d^0)$	1.073 ± 0.008	1.04 – 1.08
$\bar{\tau}(B_s^0)/\tau(B_d^0)$	0.966 ± 0.015	0.99 – 1.01
$\tau(\Lambda_b^0)/\tau(B_d^0)$	0.901 ± 0.034	0.86 – 0.95
$\tau(b\text{-baryon})/\tau(B_d^0)$	0.857 ± 0.026	0.86 – 0.95

Table 2.5. Summary of theoretical predictions of the B hadron lifetime ratios from HQET and their experimental values.

This thesis describes a measurement of the average lifetime for the B_s^0 meson, providing an important test of HQET predictions and a probe for any possible sources of new physics beyond the SM.

2.5. B_s^0 Mixing

Neutral B_q mesons[12], where q can be either a d or s quark, exhibit an oscillatory phenomenon, similar to the neutral kaon system, known as B meson mixing. Mixing allows an initially produced (i.e. at time $t = 0$) B_q state to evolve into a time-dependent superposition of the two flavor[13] eigenstates, B_q and $\bar{B}_q$.

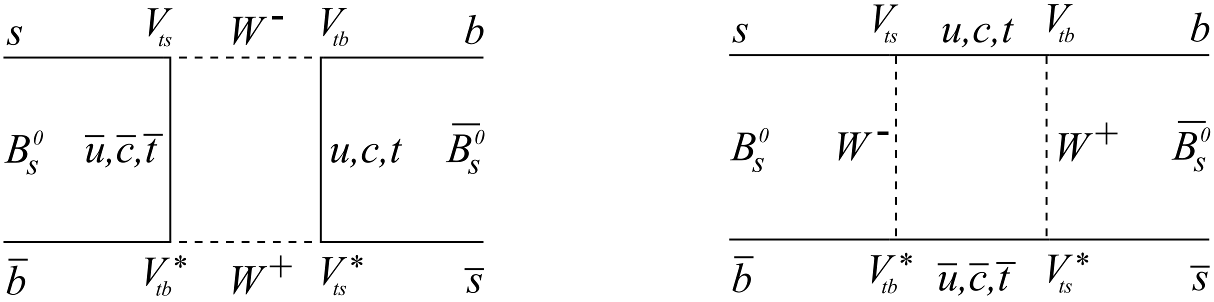

Figure 2.5. Lowest order Feynman diagrams for B_q–$\bar{B}_q$ mixing.

Initially produced $|B_q\rangle$ and $|\bar{B}_q\rangle$ flavor states evolve as a funtion of time ($|B_q(t)\rangle$ and $|\bar{B}_q(t)\rangle$) according to the time dependent Schrödinger equation:

$$i\,\frac{\partial}{\partial t}\begin{pmatrix}|B_q(t)\rangle\\|\bar{B}_q(t)\rangle\end{pmatrix}=\left(\mathbf{M}-\frac{i}{2}\mathbf{\Gamma}\right)\begin{pmatrix}|B_q(t)\rangle\\|\bar{B}_q(t)\rangle\end{pmatrix}, \tag{2.22}$$

where the mass matrix $\mathbf{M}$ and decay matrix $\mathbf{\Gamma}$ are 2×2 Hermitian matrices. Rewriting Eq. 2.22 to show all its terms gives us:

$$i\,\frac{\partial}{\partial t}\begin{pmatrix}|B_q(t)\rangle\\|\bar{B}_q(t)\rangle\end{pmatrix}=\begin{pmatrix}M_{11}-\frac{i}{2}\Gamma_{11} & M_{12}-\frac{i}{2}\Gamma_{12}\\ M_{21}-\frac{i}{2}\Gamma_{21} & M_{22}-\frac{i}{2}\Gamma_{22}\end{pmatrix}\begin{pmatrix}|B_q(t)\rangle\\|\bar{B}_q(t)\rangle\end{pmatrix}. \tag{2.23}$$

Since $\mathbf{M}$ and $\mathbf{\Gamma}$ are hermitian matrices,

$$\begin{aligned}M_{12}&=M_{21}^*,\\ \Gamma_{12}&=\Gamma_{21}^*,\end{aligned} \tag{2.24}$$

---

[12] The standard convention where B ($\bar{B}$) meson contains a $\bar{b}$ (b) quark is used.

[13] Weak and flavor eigenstates are used interchangeably.

and CPT invariance[14] requires

$$\begin{aligned} M_{11} &= M_{22}, \\ \Gamma_{11} &= \Gamma_{22}. \end{aligned} \tag{2.25}$$

The off-diagonal elements $M_{12} = M_{21}^*$ and $\Gamma_{12} = \Gamma_{21}^*$ are responsible for mixing. In the SM, major contributions to M_{12} and Γ_{12} come from the lowest order SM Feynman diagrams[15,16] for B_q–$\bar{B}_q$ mixing, shown in Fig. 2.5. They suggest the mass eigenstates of the neutral B_q meson are different from the flavor eigenstates. Diagonalizing the matrix gives two physically observable mass eigenstates, called the "Light" eigenstate $|B_L\rangle$ and the "Heavy" eigenstate $|B_H\rangle$. These can be expressed in terms of the flavor eigenstates as

$$\begin{aligned} |B_L\rangle \ &= p|B_q\rangle + q|\bar{B}_q\rangle, \\ |B_H\rangle \ &= p|B_q\rangle - q|\bar{B}_q\rangle, \end{aligned} \tag{2.26}$$

with

$$|p^2| + |q^2| = 1. \tag{2.27}$$

The time evolution of $|B_L\rangle$ and $|B_H\rangle$ can be expressed in terms of their eigenvalues (M_L–$i\frac{\Gamma_L}{2}$ and M_H–$i\frac{\Gamma_H}{2}$) as:

$$\begin{aligned} |B_L(t)\rangle \ &= e^{-(iM_L+\frac{\Gamma_L}{2})t}\ |B_L\rangle, \\ |B_H(t)\rangle \ &= e^{-(iM_H+\frac{\Gamma_H}{2})t}\ |B_H\rangle, \end{aligned} \tag{2.28}$$

where $|B_L\rangle$ and $|B_H\rangle$ denotes the mass eigenstates at time $t = 0$.

The following definitions are used for the average mass and width and the mass and width differences, where M_L, M_H, Γ_L, and Γ_H are the masses and widths of the mass eigenstates:

---

[14] While processes can separately violate charge (C), parity (P), and time (T) symmetries, the combined CPT symmetry is thought to be conserved by all physical phenomenon.

[15] These are also sometimes referred to as box diagrams due to their drawn structure.

[16] The top quark dominates this interaction due to its mass and, in general, only the two diagrams involving the top quark interactions and the V_{ts} and V_{tb} CKM matrix elements are relevant.

$$\begin{aligned} m &= \frac{M_H + M_L}{2},\ \Gamma = \frac{\Gamma_L + \Gamma_H}{2}, \\ \Delta m &= M_H - M_L,\ \Delta\Gamma = \Gamma_L - \Gamma_H. \end{aligned} \tag{2.29}$$

The mass difference Δm is positive by definition. $\Delta\Gamma$ can be either positive or negative.

The mass difference and width difference can be related to the matrix elements as follows:

$$\begin{aligned} \Delta m &= 2\left|M_{12}\right|, \\ \Delta\Gamma &= 2\left|\Gamma_{12}\right|\cos\phi, \end{aligned} \tag{2.30}$$

where the phase ϕ is defined as

$$\phi = Arg\left(-\tfrac{M_{12}}{\Gamma_{12}}\right) \tag{2.31}$$

The width difference is then related to the phase of the mixing.

The time evolution of the flavor eigenstates expressed in terms of the mass eigenstates are

$$\begin{aligned} \left|B_q(t)\right\rangle &= \tfrac{1}{2p}\left(e^{-(iM_L+\frac{\Gamma_L}{2})t}\left|B_L\right\rangle + e^{-(iM_H+\frac{\Gamma_H}{2})t}\left|B_H\right\rangle\right), \\ \left|\bar{B}_q(t)\right\rangle &= \tfrac{1}{2q}\left(e^{-(iM_L+\frac{\Gamma_L}{2})t}\left|B_L\right\rangle - e^{-(iM_H+\frac{\Gamma_H}{2})t}\left|B_H\right\rangle\right). \end{aligned} \tag{2.32}$$

Expressing these in terms of the flavor eigenstates instead of the mass eigenstates and applying the time evolution operator gives the following:

$$\begin{aligned} \left|B_q(t)\right\rangle &= g_+(t)\left|B_q\right\rangle + \frac{q}{p}g_-(t)\left|\bar{B}_q\right\rangle, \\ \left|\bar{B}_q(t)\right\rangle &= \frac{p}{q}g_-(t)\left|B_q\right\rangle + g_+(t)\left|\bar{B}_q\right\rangle, \end{aligned} \tag{2.33}$$

where[17]

$$\begin{aligned} g_+(t) = & \quad e^{-imt}e^{-\Gamma t/2}\left[\cosh\frac{\Delta\Gamma t}{4}\cos\frac{\Delta m t}{2} + i\sinh\frac{\Delta\Gamma t}{4}\sin\frac{\Delta m t}{2}\right], \\ g_-(t) = & \quad e^{-imt}e^{-\Gamma t/2}\left[-\sinh\frac{\Delta\Gamma t}{4}\cos\frac{\Delta m t}{2} + i\cosh\frac{\Delta\Gamma t}{4}\sin\frac{\Delta m t}{2}\right]. \end{aligned} \tag{2.34}$$

The probability, written in terms Δm and $\Delta\Gamma$, that a pure state $|B_q\rangle$ at time t=0 oscillated and decayed as a $|\bar{B}_q\rangle$ state after some time t can be written as

$$\mathcal{P}_m^{B_q}(t) = \left|\left\langle \bar{B}_q \,\middle|\, B_q(t)\right\rangle\right|^2. \tag{2.35}$$

The probability that the same state did not oscillate can be written as

$$\mathcal{P}_u^{B_q}(t) = \left|\left\langle B_q \,\middle|\, B_q(t)\right\rangle\right|^2. \tag{2.36}$$

Similar equations can be written for the $|\bar{B}_q\rangle$ state, giving the full set of probability equations as,

$$\begin{aligned} \mathcal{P}_u^{B_q}(t) = & \quad \frac{e^{-\Gamma t}}{\Gamma\left(\frac{1+|q/p|^2}{\Gamma^2-\Delta\Gamma^2/4} + \frac{1-|q/p|^2}{\Gamma^2+\Delta m^2}\right)}\left(\cosh\frac{\Delta\Gamma}{2}t + \cos\Delta m t\right), \\ \mathcal{P}_m^{B_q}(t) = & \quad \frac{|q/p|^2 e^{-\Gamma t}}{\Gamma\left(\frac{1+|q/p|^2}{\Gamma^2-\Delta\Gamma^2/4} + \frac{1-|q/p|^2}{\Gamma^2+\Delta m^2}\right)}\left(\cosh\frac{\Delta\Gamma}{2}t - \cos\Delta m t\right), \\ \mathcal{P}_u^{\bar{B}_q}(t) = & \quad \frac{|q/p|^2 e^{-\Gamma t}}{\Gamma\left(\frac{1+|q/p|^2}{\Gamma^2-\Delta\Gamma^2/4} - \frac{1-|q/p|^2}{\Gamma^2+\Delta m^2}\right)}\left(\cosh\frac{\Delta\Gamma}{2}t + \cos\Delta m t\right), \\ \mathcal{P}_m^{\bar{B}_q}(t) = & \quad \frac{e^{-\Gamma t}}{\Gamma\left(\frac{1+|q/p|^2}{\Gamma^2-\Delta\Gamma^2/4} - \frac{1-|q/p|^2}{\Gamma^2+\Delta m^2}\right)}\left(\cosh\frac{\Delta\Gamma}{2}t - \cos\Delta m t\right). \end{aligned} \tag{2.37}$$

---

[17] Since $\Delta\Gamma$ is not equal to zero, $g_+(t)$ never goes to zero, and $g_-(t)$ is only zero when $t = 0$. This implies an initially pure $B_q(\bar{B}_q)$ will never evolve into a pure state again.

The asymmetry in these expressions between B_q and $\bar{B}_q$ are due to possible CP-violating effects. The CP operation on neutral B mesons can be written such that:

$$\begin{aligned} CP|B_q\rangle &= -|\bar{B}_q\rangle \\ CP|\bar{B}_q\rangle &= -|B_q\rangle \end{aligned} \tag{2.38}$$

The CP eigenstates are then:

$$\begin{aligned} |B_q^{\,even}\rangle &= \tfrac{1}{\sqrt{2}}\left(|B_q\rangle - |\bar{B}_q\rangle\right) \\ |B_q^{\,odd}\rangle &= \tfrac{1}{\sqrt{2}}\left(|B_q\rangle + |\bar{B}_q\rangle\right) \end{aligned} \tag{2.39}$$

For B_s^0 mesons, $\frac{q}{p} = 1$ is a good approximation and leads to the result that mass eigenstates are nearly CP eigenstates [**16**]. This result will be used as an important theoretical tool to separate final state products of $B_s^0 \to J/\psi(\mu^+\mu^-)\phi(K^+K^-)$ decays into CP even and CP odd components using the angular analysis method described in the next section.

2.6. Angular Distribution in $B_s^0 \to J/\psi(\mu^+\mu^-)\phi(K^+K^-)$

The relevant theory for describing the angular distributions in $B_s^0 \to J/\psi\phi$ decays, which proceeds through the quark sub-process $\bar{b} \to \bar{c}c\bar{s}$, is now examined. A Feynman diagram of this process is shown in Fig. 2.7. Both B_s^0 and $\bar{B}_s^0$ can decay to this final state, and they are expected to mix in such a way that the two physical eigenstates (mass or CP eigenstates) have a sizeable width difference. By analyzing the angular distributions of the final state products of $B_s^0 \to J/\psi(\mu^+\mu^-)\phi(K^+K^-)$ decays it is possible to separate the CP even and CP odd components[18] and, therefore, measure the width difference between the B_s^0 mass eigenstates. Other useful parameters can be exracted, such as the CP-violating phase ϕ_s, which represents a sensitive probe for CP-violating effects from physics beyond the SM [**17, 18**].

---

[18] The $J/\psi\phi$ final state has $\sim 75\%$ contribution from CP even, and $\sim 25\%$ from CP odd.

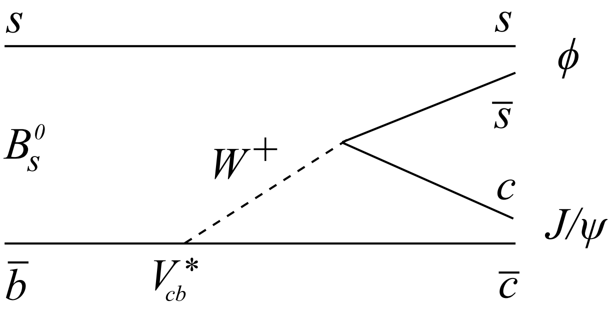

Figure 2.6. Feynman diagram for the direct decay $B_s^0 \to J/\psi\phi$.

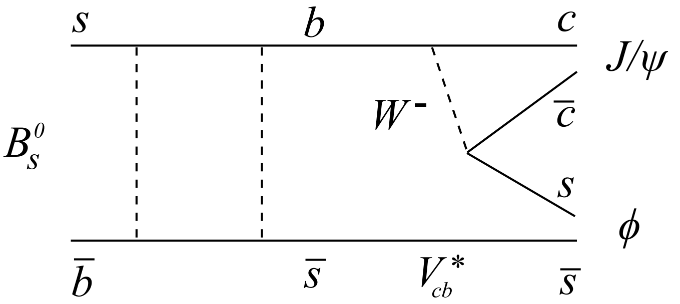

Figure 2.7. Feynman diagram for the decay with mixing $B_s^0 \to \bar{B}_s^0 \to J/\psi\phi$.

The $B_s^0 \to J/\psi\phi$ decay is an example of a pseudoscalar[19](B_s^0) meson with spin=0 decaying to two vector mesons (J/ψ and ϕ), each with spin=1. The allowed angular momentum states between the vector mesons are L=0, 1, 2. The final state will be an admixture of CP-even contributions with L=0,2 and CP-odd with L=1.

To separate the CP-even and CP-odd contributions in the final state, it is convenient to use the *transversity* basis [**19**], which describes the final state angular distributions in terms of three linear polarization states: A_0, $A_{\|}$, and $A_{\perp}$, where A_0 and $A_{\|}$ measure contributions from CP-even states and $A_{\perp}$ from CP-odd states. They are normalized such that

$$|A_0|^2 + |A_{\|}|^2 + |A_{\perp}|^2 = 1. \tag{2.40}$$

---

[19] A pseudoscalar behaves similarly to a scalar, except it changes sign under parity inversion.

The decay amplitude for a pure B_s^0 decay[20] can be expressed [**20**] in terms of these three linear polarization states as:

$$\Gamma(B_s^0(t) \to J/\psi\,\phi) = \frac{A_0(t)}{x}\,\epsilon_{J/\psi}^{*L}\,\epsilon_{\phi}^{*L} - A_{\|}(t)\,\epsilon_{J/\psi}^{*T}\cdot\epsilon_{\phi}^{*T}/\sqrt{2} - iA_{\perp}(t)\,\epsilon_{J/\psi}^{*}\times\epsilon_{\phi}^{*}\cdot\hat{\mathbf{p}}_{\phi}/\sqrt{2} \quad (2.41)$$

where $x \equiv p_{J/\psi}\cdot p_{\phi}/(m_{J/\psi}m_{\phi})$, $\hat{\mathbf{p}}_{\phi}$ is the unit vector along the direction of motion of ϕ in the rest frame of J/ψ, and the time dependences originates from B_s^0– $\bar{B}_s^0$ mixing. In this notation, an unmixed B_s^0 meson is present at $t = 0$. Since the CP-even and CP-odd components differ in both time evolution and angular correlations, the angular distribution can be used to separate them and their time evolution can be studied individually.

The full angular distribution of the four final state products from $B_s^0 \to J/\psi\phi$ can be expressed in terms of three angles (θ,φ,ψ) in the transversity basis [**20**]. For an initially produced B_s^0 meson the angular distribution can be written as:

$$\frac{d^4\Gamma[B_s^0(t) \to J/\psi(\mu^+\mu^-)\phi(K^+K^-)]}{d\cos\theta\;d\varphi\;d\cos\psi\;dt} = \frac{9}{32\pi}\Big[\;2|A_0(t)|^2\cos^2\psi(1-\sin^2\theta\cos^2\varphi)$$

$$+\sin^2\psi\{|A_{\|}(t)|^2(1-\sin^2\theta\sin^2\varphi) + |A_{\perp}(t)|^2\sin^2\theta - \text{ Im }(A_{\|}^*(t)A_{\perp}(t))\sin 2\theta\sin\varphi\}$$

$$+\frac{1}{\sqrt{2}}\sin 2\psi\{\text{ Re }(A_0^*(t)A_{\|}(t))\sin^2\theta\sin 2\varphi + \text{ Im }(A_0^*(t)A_{\perp}(t))\sin 2\theta\cos\varphi\;\}\;\Big]. \quad (2.42)$$

The three angles, displayed in the transversity basis in Fig. 2.8, are used to extract the decay amplitudes. Angles θ and ϕ are defined in the J/ψ rest-frame, where the $+x$-axis indicates the direction of travel of the ϕ meson, and the y-axis lies in the plane formed by the K^+ and K^- mesons, with the K^+ traveling in the $+y$ direction. Using the right-hand rule, the z-axis is then normal to this plane. The third angle ψ is defined in the ϕ meson rest-frame. The angles are defined as:

θ – The angle between the μ^+ and the z-axis in the J/ψ rest-frame.

ϕ – The angle between the projection of the μ^+ on the on the x-y plane and the x-axis in the J/ψ rest-frame.

---

[20] For example, a produced B_s^0 meson initially identified as a B_s^0 meson by a flavor tag.

ψ – The angle between the K^+ and the negative direction of the J/ψ in the ϕ meson rest-frame.

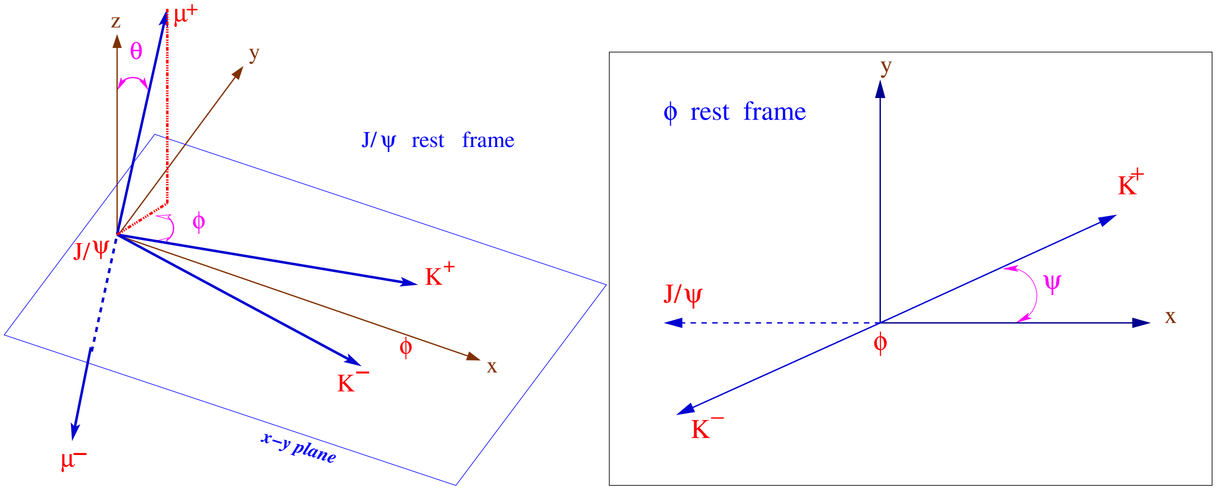

Figure 2.8. Diagrams displaying the three decay angles (θ,φ,ψ) in the transversity basis. The left diagram show angles θ and φ in the J/ψ rest-frame, and the right diagram shows angle ψ in the ϕ meson rest-frame.

With this convention:

$$\mathbf{x} = \mathbf{p}_\phi, \quad \mathbf{y} = \frac{\mathbf{p}_{K^+} - \mathbf{p}_\phi(\mathbf{p}_\phi \cdot \mathbf{p}_{K^+})}{|\mathbf{p}_{K^+} - \mathbf{p}_\phi(\mathbf{p}_\phi \cdot \mathbf{p}_{K^+})|}, \quad \mathbf{z} = \mathbf{x} \times \mathbf{y}$$
$$\sin\theta \ \cos\varphi = \mathbf{p}_{\ell^+} \cdot \mathbf{x}, \quad \sin\theta \ \sin\varphi = \mathbf{p}_{\ell^+} \cdot \mathbf{y}, \quad \cos\theta = \mathbf{p}_{\ell^+} \cdot \mathbf{z} \tag{2.43}$$
$$\cos\psi = -\mathbf{p}'_{K^+} \cdot \mathbf{p}'_{J/\psi}$$

The bold-face characters represent unit 3-vectors and everything is measured in the rest frame of J/ψ, while the primed quantities are *unit vectors* measured in the rest frame of ϕ.

The time evolution of the individual components are given in Table 2.6, where $\Delta m_s \equiv m_H - m_L > 0$ is the mass difference of the mass eigenstates B_s^H(CP-odd) and B_s^L(CP-even) of the (B_s^0, $\bar{B}_s^0$) system and $\bar{\Gamma} \equiv (\Gamma_H + \Gamma_L)/2$ denotes their average decay width.

Observable	Time evolution
$\lvert A_0(t)\rvert^2$	$\lvert A_0(0)\rvert^2 \left[e^{-\Gamma_L t} \mp e^{-\bar{\Gamma} t}\sin(\Delta m_s t)\phi_s\right]$
$\lvert A_\parallel(t)\rvert^2$	$\lvert A_\parallel(0)\rvert^2 \left[e^{-\Gamma_L t} \mp e^{-\bar{\Gamma} t}\sin(\Delta m_s t)\phi_s\right]$
$\lvert A_\perp(t)\rvert^2$	$\lvert A_\perp(0)\rvert^2 \left[e^{-\Gamma_H t} \pm e^{-\bar{\Gamma} t}\sin(\Delta m_s t)\phi_s\right]$
$\mathrm{Re}(A_0^*(t)A_\parallel(t))$	$\lvert A_0(0)\rvert\lvert A_\parallel(0)\rvert\cos(\delta_2-\delta_1)\left[e^{-\Gamma_L t} \mp e^{-\bar{\Gamma} t}\sin(\Delta m_s t)\phi_s\right]$
$\mathrm{Im}(A_\parallel^*(t)A_\perp(t))$	$\pm\lvert A_\parallel(0)\rvert\lvert A_\perp(0)\rvert\left[e^{-\bar{\Gamma} t}\sin(\delta_1-\Delta m_s t) \pm \frac{1}{2}\left(e^{-\Gamma_H t}-e^{-\Gamma_L t}\right)\cos(\delta_1)\phi_s\right]$
$\mathrm{Im}(A_0^*(t)A_\perp(t))$	$\pm\lvert A_0(0)\rvert\lvert A_\perp(0)\rvert\left[e^{-\bar{\Gamma} t}\sin(\delta_2-\Delta m_s t) \pm \frac{1}{2}\left(e^{-\Gamma_H t}-e^{-\Gamma_L t}\right)\cos(\delta_2)\phi_s\right]$

Table 2.6. Time evolution of the decay $B_s^0 \to J/\psi(\mu^+\mu^-)\phi(K^+K^-)$ where the upper (lower) sign corresponds to a pure $B_s^0 \to J/\psi\phi$ ($\bar{B}_s^0 \to J/\psi\phi$) at $t = 0$.

The phases $\delta_1 \equiv \mathrm{Arg}(A_\parallel(0)^* A_\perp(0))$ and $\delta_2 \equiv \mathrm{Arg}(A_0(0)^* A_\perp(0))$ are CP-conserving strong phases. In the absence of final-state interactions[21], they are expected to be 0 (mod π).

The quantity ϕ_s (ϕ_{CKM} in SM) is the CP-violating weak phase, which is introduced through interference effects between B_s^0–$\bar{B}_s^0$ mixing and decay processes. It can be expressed in terms of CKM matrix elements [**21**] as

$$e^{i\phi_s} = \frac{V_{ts}V_{tb}^*}{V_{ts}^*V_{tb}}\frac{V_{cs}^*V_{cb}}{V_{cs}V_{cb}^*}, \tag{2.44}$$

In terms of the Wolfenstein expansion, ϕ_s is proportional to the parameter η:

$$\phi_s = 2\lambda^2\eta = \mathcal{O}(0.03). \tag{2.45}$$

Integration of the full three-angle distributions for tagged $B_s^0 \to J/\psi(\mu^+\mu^-)\phi(K^+K^-)$ decays, given by Eq. 2.42, over the two decay angles φ and ψ, leads to the following one-angle distribution.

---

[21] Probably not a justifiable assumption for $B_s^0 \to J/\psi\phi$

$$\frac{d^2\Gamma}{d\cos\theta\ dt} = \frac{3}{8}\left[\ (|A_0(t)|^2 + |A_\parallel(t)|^2)(1+\cos^2\theta) + 2|A_\perp(t)|^2\sin^2\theta\ \right] \tag{2.46}$$

From this one-angle distribution, the observables $|A_0(t)|^2 + |A_\parallel(t)|^2$ and $|A_\perp(t)|^2$ can be determined.

The decay width Γ_L and Γ_H can be determined by fitting the separated CP even and CP odd lifetime components with exponentials. A proper treatment of detector acceptance and the results above are used to study the tagged decay of $B_s^0 \rightarrow J/\psi(\mu^+\mu^-)\phi(K^+K^-)$ and to measure the width difference $\Delta\Gamma_s$ from the decay widths Γ_L and Γ_H, and the CP-violating phase ϕ_s. A measurement of a phase which significantly deviates from the SM prediction would be a clear sign of new physics.

CHAPTER 3

The Tevatron Accelerator and the DØ Run II Detector

3.1. Introduction

The Tevatron proton-antiproton ($p\overline{p}$) collider at Fermi National Accelerator Laboratory (FNAL [**22**]), in Batavia, Illinois is currently the world's highest-energy particle collider, operating at $\sqrt{s} = 1.96$ TeV. The D0 detector is one of two general purpose detectors located along the 6.26 km (3.89 miles) circumference Tevatron ring and sits at one of the $p\overline{p}$ interaction points. This chapter briefly describes the Fermilab accelerator facility and the DØ Run II detector. Full details of the Tevatron and the DØ detector can be found in [**23, 24**].

3.2. The Tevatron Accelerator

The Tevatron synchrotron accelerator is the final and largest component in a chain of seven accelerators that make up the Fermilab accelerator facility, displayed in Fig. 3.1. It brings protons and antiprotons to their full $\sqrt{s} = 1.96$ TeV energy. Before reaching this final stage, sources of protons and antiprotons must be created and pre-accelerated. The Cockcroft-Walton, LINAC (linear accelerator), and Booster synchrotron provide a source of 8 GeV protons. The Antiproton Source, including the Debuncher and Accumulator, provides a source of antiprotons. The Main Injector serves a dual purpose: it is the final accelerating stage before proton and antiproton beams are injected into the Tevatron synchrotron accelerator, and delivers a source of protons to the Antiproton Source. The final stage is the Tevatron accelerator, which accelerates circulating beams of protons and antiprotons each to 980 GeV and collides them at the BØ and DØ interactions

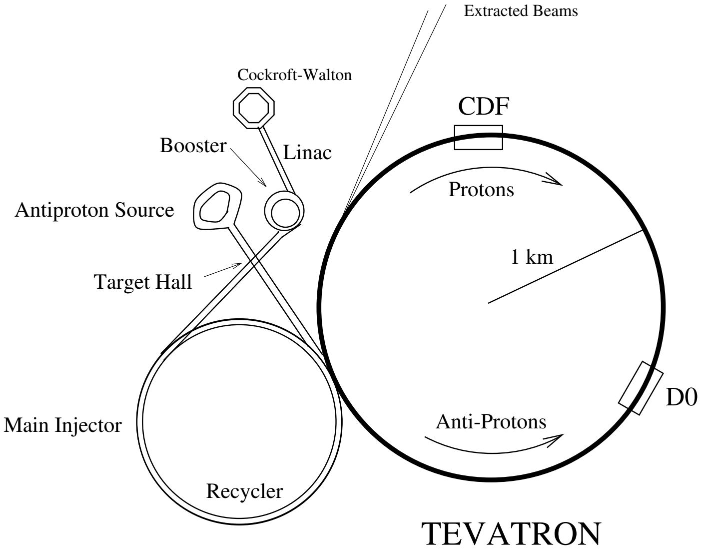

Figure 3.1. The Fermi National Accelerator Laboratory in Batavia, Illinois.

points where the Colliding Detector at Fermilab (CDF) and DØ detectors are located, respectively.

3.2.1. The Proton Source

The Tevatron proton source production and initial acceleration begins with a three stage process that produces protons from ordinary Hydrogen gas (H_2) and accelerates them to 8 GeV. Components involved in these initial stages are the Cockroft-Walton, LINAC (linear accelerator), and Booster synchrotron.

H^- ions are produced by an electrical discharge from Hydrogen gas, and accelerated by a +ve voltage to 25 keV. These 25 keV H^- ions are then released into the Cockroft-Walton, a 750 KeV DC voltage source, which accelerates the H^- ions to 750 KeV. The H^- ions are then injected into the LINAC, a 500 feet long linear accelerator, where they are accelerated to 400 MeV using Radio Frequency (RF) cavities. The 400 MeV H^- ions are transferred to the Booster, the first synchrotron in the accelerator chain. The Booster synchrotron contains a sequence of dipole and quadrapole magnets along with 17 RF cavities. The protons are produced here by passing the H^- ions coming from the LINAC through a carbon foil which strips away the two electrons. Once the Booster is filled with enough proton bunches (5-6$\times 10^{12}$ protons) and they have reached an energy of 8 GeV, they are transferred into the Main Injector for the next stage of acceleration.

3.2.2. Main Injector

The Main Injector is a 1 km diameter circular synchrotron that accelerates protons transferred by the Booster and antiprotons from the Antiproton Source from 8 GeV to 150 GeV before injecting them into the Tevatron. In addition, the Main Injector directs 120 GeV protons towards a target at the Antiproton Source for antiproton production.

3.2.3. The Antiproton Source

The Antiproton Source is made of three primary components: the Target Station, the Debuncher, and the Accumulator. The Target Station receives 120 GeV protons from the Main Injector and steers them into a target made of nickel plates. The interaction produces a shower of secondary particles (among them antiprotons) at varying angles and momentum. Using a Lithium lens and bending magnets, positively charged particles are filtered from this shower and a focused beam of negatively charged particles is produced. The spread in momentum and position of the antiprotons is reduced by a process known as Stochastic cooling, which is used in both the Accumulator and Debuncher. The Accumulator serves to store antiprotons over several hours until enough have been collected to send to the Main Injector. On average, 20 antiprotons are gathered for every 1 million protons that hit the nickel target.

3.2.4. The Tevatron

The Tevatron is the final stage of acceleration and brings the 150 GeV protons and antiprotons delivered by the Main Injector to 980 GeV, or $\sqrt{s} = 1.96$ TeV. Protons and antiprotons travel in groups of particles, called bunches, within the same beam pipe. Each beam is composed of three super-bunches, each containing 12 bunches, for a total of 36 bunches. During each store, 36 bunches of protons and 36 bunches of antiprotons circulate in opposing directions, resulting in a time interval of 396 ns between two consecutive collisions. Nearly 1000 superconducting magnets positioned along the 6.26 km circumference Tevatron ring provide magnetic fields up to 4 Tesla and steer the beams of charged particles along the circular orbit. Once both proton and antiproton beams reach their full energy the beams are squeezed in the transverse plane by low-β quadrapole magnets and collide at two crossing points: BØ (the location of the CDF detector) and DØ (the location of the DØ detector).

The number of collisions per second depends on the instantaneous luminosity, given by

$$\mathcal{L} = \frac{10^{-6}\ f\ B\ N_p\ N_{\bar{p}}\ (6\beta_r\gamma_r)}{2\pi\ \beta^*\ (\epsilon_p + \epsilon_{\bar{p}})}\ H(\sigma_l/\beta^*)\ 10^{31}\ /cm^2/s. \tag{3.1}$$

In this equation, f is the bunch revolution frequency ($\equiv$ 47.7 KHz), B is number of bunches ($\equiv$ 36 for Run II). $\beta_r\gamma_r$ ($\equiv$ 1045) is the relativistic factor, and ϵ_p and $\epsilon_{\bar{p}}$ are the transverse emittances for proton and antiproton at the interaction region. β^* is the beta function at the interaction point[1], which is designed to be equal to 35 cm. H is the hour glass factor[2] and lies in the range of 0.60-0.75. N_p and $N_{\bar{p}}$ are the number ($\sim 10^9$) of protons and antiprotons per bunch. σ_l is the bunch length, measured in centimeters. These parameters are optimized to the best possible values for obtaining the highest instantaneous luminosity.

---

[1] β^* is related with beam width (σ) in transverse plane through following relation: $\sigma^2 = \epsilon_{eff}\left(\beta^* + \frac{(z-z_0)^2}{\beta^*}\right)$, where $\epsilon_{eff} = \frac{\epsilon_p\epsilon_{\bar{p}}}{\epsilon_p+\epsilon_{\bar{p}}}$.

[2] Effective number due to increase of the β^* along the $p-\bar{p}$ bunches during collision.

3.3. The DØ Detector

The DØ detector is a general-purpose high energy particle physics detector located at one of the two interaction regions along the Tevatron accelerator ring. It is designed to record kinematic information from $p\overline{p}$ collisions by examining the position and energy of particles passing through it; both those produced directly in the collision, and those that result from particle decays. Interaction of these particles with the DØ sub-detectors, described in more detail below, results in energy loss which is measured and recorded for analysis.

The DØ detector can identify a broad spectrum of particles using its three major sub-detectors: central tracker, uranium/liquid-argon calorimeter, and a muon spectrometer. Particles relevant to this thesis are charged kaons and muons, therefore focus will be made primarily on the central tracking and muon systems. Fig. 3.2 shows a cross-sectional view of the DØ Run II detector. A full description of the DØ Run II detector can be found in [**25**].

3.4. Coordinate System

In the DØ detector right-handed Cartesian coordinate system, the $+z$-axis is defined as the direction of proton travel, the y-axis is vertical, and the $+x$-axis points towards the center of the Tevatron ring, as shown in Fig. 3.2. The standard polar coordinates (r, θ, ϕ) are also useful in the detector description. The coordinate r is the perpendicular distance from the z axis,

$$r = \sqrt{x^2 - y^2}, \tag{3.2}$$

and ϕ is the azimuthal angle

$$\phi = \arctan \frac{y}{x}. \tag{3.3}$$

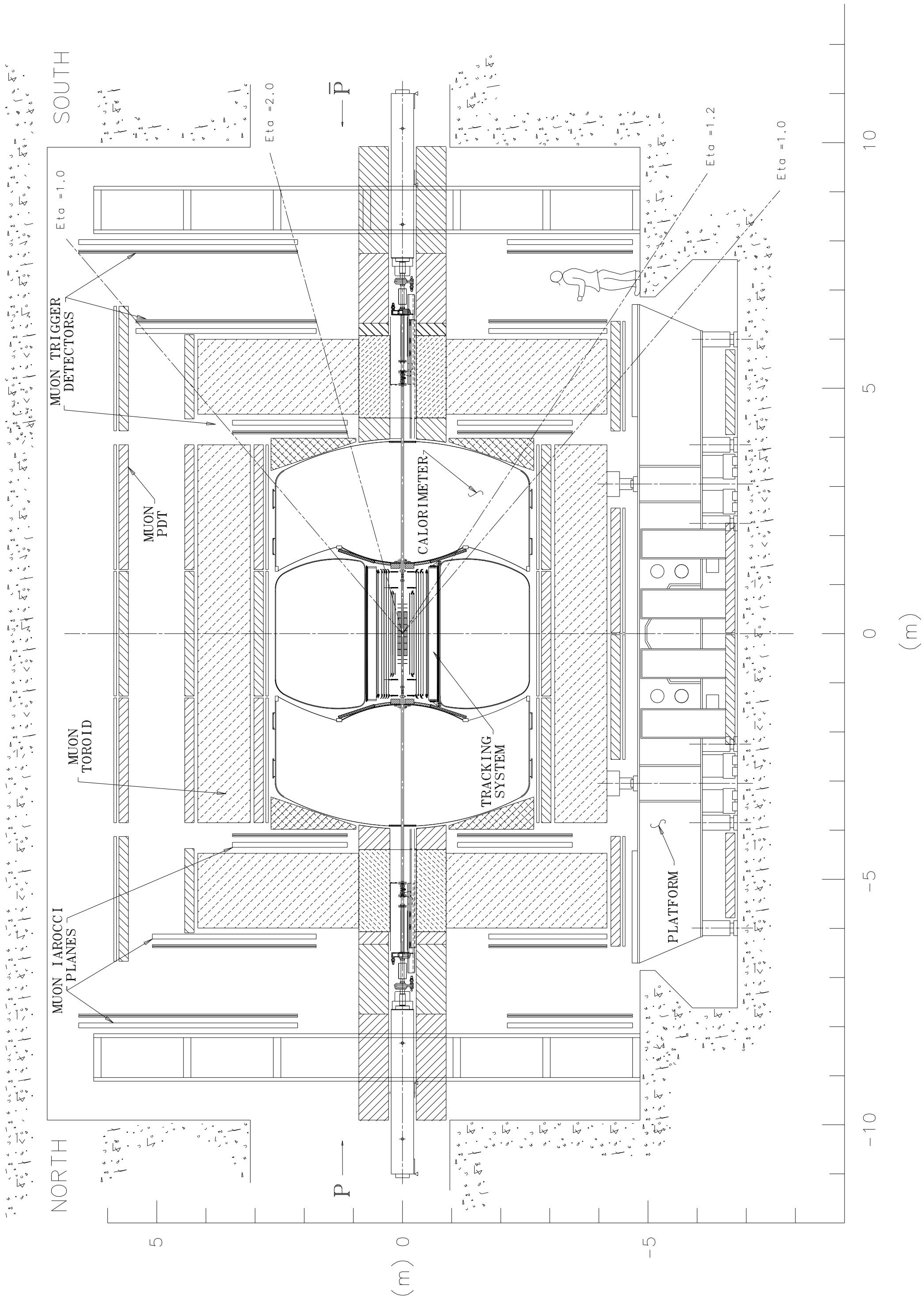

Figure 3.2. Cross-sectional view of the DØ RunII detector.

The pseudorapidity, η, is defined as

$$\eta = -\ln\left(\tan\frac{\theta}{2}\right) \tag{3.4}$$

and is obtained from the rapidity, y, where

$$y = \frac{1}{2}\ln\left(\frac{E+p_z}{E-p_z}\right), \tag{3.5}$$

when particle masses are neglected. Pseudorapidity approximates the true rapidity for finite angles in the limit $m << E$, where m is the particle's mass and E is its energy. It is a convenient measure at hadron colliders where the multiplicity of energetic particles remains approximately constant in η.

Often times it is not possible to measure the z-axis component of the momentum accurately when particles escape detection as they travel down the beam pipe. Additionally, since partons carry only a fraction of the proton or antiproton momentum, the initial longitudinal momentum of the collision is unknown. It is convenient, then, to use the momentum vector projected onto a plane perpendicular to the beam axis. This is known as transverse momentum, defined as

$$p_T = p \cdot \sin\theta. \tag{3.6}$$

3.5. Central Tracking

Tracking detectors provide the first layers of particle detection at DØ and are designed to measure particle positions with minimal energy loss. The DØ central tracking system, composed of a Silicon Microstrip Tracker (SMT) and Central Fiber Tracker (CFT), surrounded by a nearly uniform 2 Tesla solenoidal magnet, measures the momentum, distance of closest approach, and the sign of the charge for particles produced in a collision. The DØ Run IIb upgrade added an additional innermost layer of silicon tracking, called Layer 0, to its SMT detector.

The combined SMT and CFT information provide excellent tracking and vertexing performance. Track momentum resolution is $\sigma(p_T)/p_T^2 \sim 0.2\%$, with track reconstruction efficiency of more than 95%. The impact parameter resolution is ∼20 microns in the transverse plane, and ∼40 microns along the beam line. A cross-sectional view of the central tracking system is shown in Fig. 3.3.

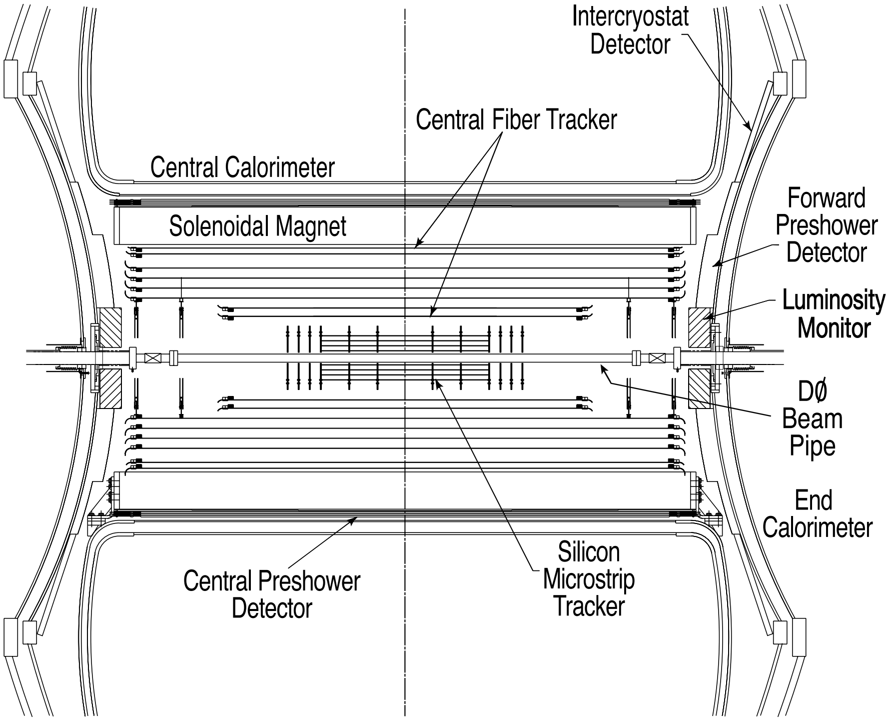

Figure 3.3. Cross-sectional view of the central tracking system in the $y-z$ plane.

3.5.1. Run IIa Silicon Microstrip Tracker (SMT)

The Silicon Microstrip Tracker (SMT) is the innermost system of the DØ detector, and allows for an accurate determination of impact parameters and identification of secondary vertices. It provides track and vertex information over nearly the full η coverage of the calorimeter and muon systems. Under ideal conditions, tracks would enter all detector surfaces perpendicularly for all regions of η. To acheive this, the SMT is composed of barrel modules interspersed with disk detectors in the central region, with larger disk detectors in the forward and backward regions, as shown in Fig 3.4.

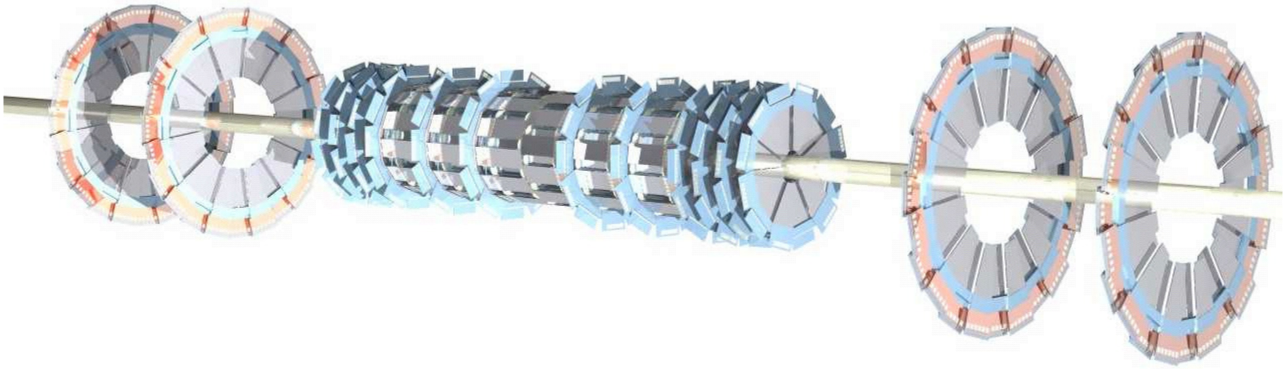

Figure 3.4. Design of the Silicon Microstrip Tracker.

Barrel detectors primarily measure the $r-\phi$ coordinate, while disk detectors measure the $r-z$ and $r-\phi$ coordinates. Vertices at small η are measured in the barrels, whereas vertices for high η particles are reconstructed in three dimensions by the disks.

There are six barrels in the central region, each having four "superlayers". Each superlayer has staggered, overlapping sub-layers to maximize coverage, as shown in Fig. 3.5. Superlayers 1 and 2 each have twelve ladder detectors, like the one shown in Fig. 3.6, while superlayers 3 and 4 have twenty-four, for a total of 432 ladders. The two outer barrels have single-sided and double-sided 2° stereo ladders. The four inner barrels have double-sided 90° stereo and double-sided 2° stereo ladders.

Twelve "F-disks" occupy the space between the barrels and the interaction region beyond the last barrel. F-disks are made of double-sided wedge detectors with 15° stereo strips, like the one shown in Fig. 3.7. In the far forward regions exists two large-diameter disks, called "H-disks," which provide tracking at high $|\eta|$. Twenty-four full wedges consisting of two single-sided "half" wedges with an effective stereo angle of 7.5°, are mounted

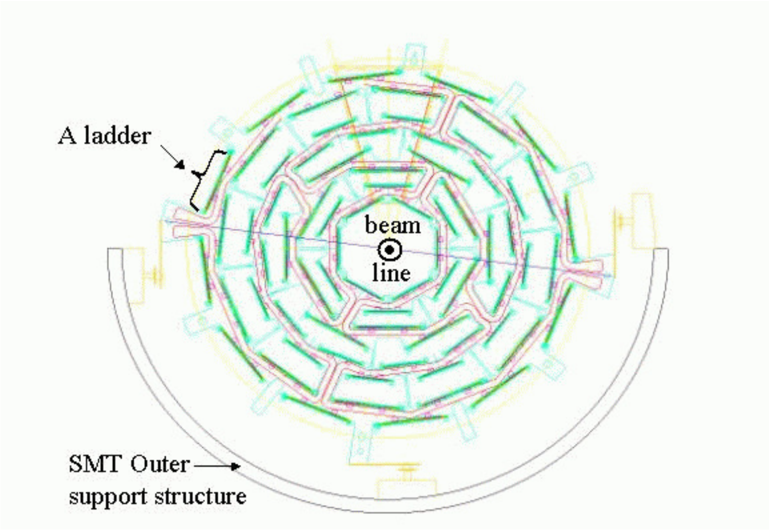

Figure 3.5. Cross-sectional view of an SMT barrel module.

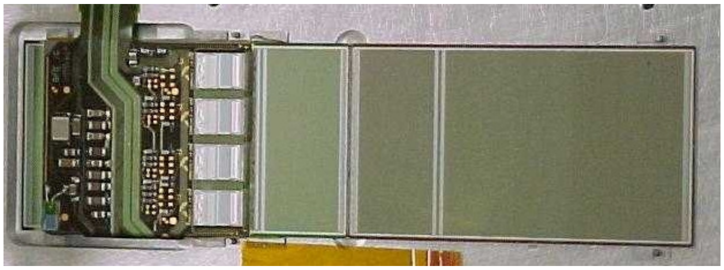

Figure 3.6. SMT Ladder detector.

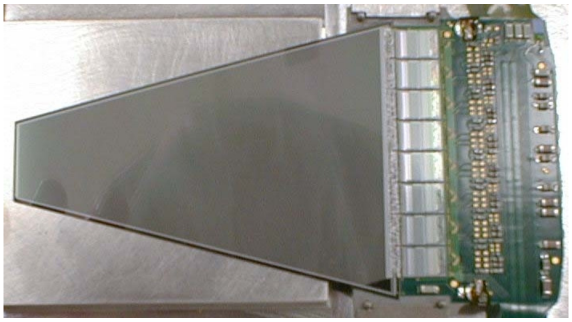

Figure 3.7. SMT F-disk wedge detector.

on each H-disk. There are 144 F-wedges and 96[3] full H-wedges in the Run IIa tracker. There is a total of 912 readout modules and 792,576 individual readout channels. Table 3.3 summarizes some specifications of the Run IIa SMT detector.

	Barrels	F-Disks	H-Disks
Channels	387,072	258,048	147,456
Modules	432	144	96
Silicon Area	1.3 m^2	0.4 m^2	1.3 m^2
Inner Radius	2.7 cm	2.6 cm	9.5 cm
Outer Radius	10.5 cm	10.0 cm	26 cm

Table 3.1. Run IIa Silicon Microstrip Tracker detector specifications.

The SMT is read out by 128-channel SVXIIe readout chips [**26**], designed to work with double-sided detectors. Assemblies made of kapton flex circuits laminated to high density interconnects (HDI) hold the SVXIIe chips and supporting electronic components in place. The SVXIIe chip features include 53 MHz read out spread, sparsification, down-loadable ADC ramp, pedestal, and bandwidth setting.

A diagram of the SMT readout chain is shown in Fig. 3.8. HDIs are connected to adapter cards (AC) by 2.5 m long low mass kapton flex cables. The ACs transfer the signal and power supplies from the HDIs to 10 m long high mass 80 conductor cables which connect to interface boards (IB). The IBs supply and monitor power to the SVXIIe chips, distribute bias voltage to the sensors and refresh data and control signals traveling between the HDIs and the sequencers. The sequencers control chip operations and covert their data into optical signals carried over 1 GB/s optical links to VME read out Buffer boards. The VME readout buffers receive and hold the data pending a Level-2 trigger decision. The SMT is operated at a temperature of 5-10° C to minimize effects from radiation damage.

---

[3] The two outermost H-disks comprising 48 readout channels were removed during the Run IIb upgrade to provide the necessary readout channels for the new Layer 0 detector.

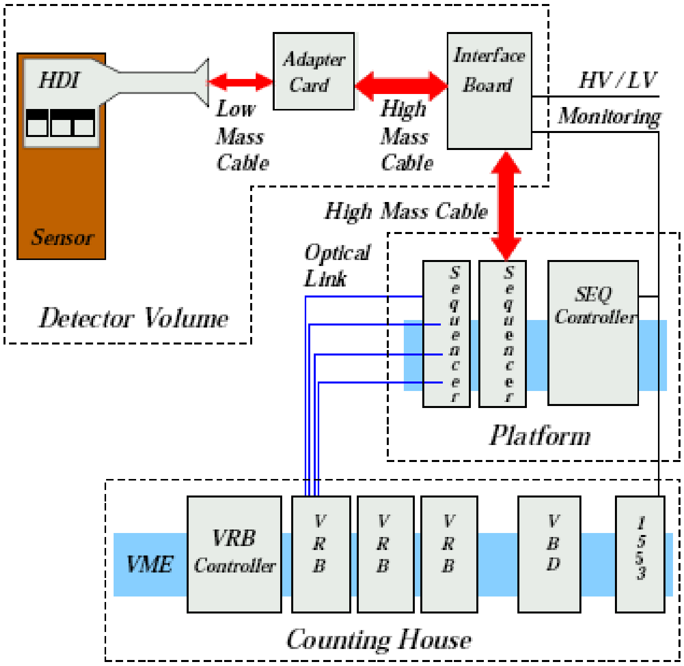

Figure 3.8. Read out chain of the SMT.

3.5.2. The Layer 0 Run IIb SMT Upgrade Detector

The Run IIa SMT detector was designed to withstand $\sim$4fb^{-1} of integrated luminosity. To mitigate tracking losses due to radiation damage to the inner SMT layers, a new innermost layer of silicon was added to the existing silicon system for the Run IIb data taking period. This new detector, called Layer 0, lies between the beam pipe and the first SMT layer. A conceptual drawing of the detector design is shown in Fig. 3.9. Two sublayers reside at $r = 16.0$ mm and $r = 17.6$ mm radii. Layer 0 is crucial for achieving improved impact parameter resolution, b-jet tagging efficiency, as well as maintaining pattern recognition capabilities for high pseudorapidity tracks during the remainder of Run II.

Layer 0 consists of a carbon fiber support structure mounted onto the Tevatron beam pipe. Low mass analog cables transfer signals from 48 radiation hard silicon sensors, as shown in Fig. 3.10, to SVX4 readout chips specifically designed for the Run IIb upgrade.

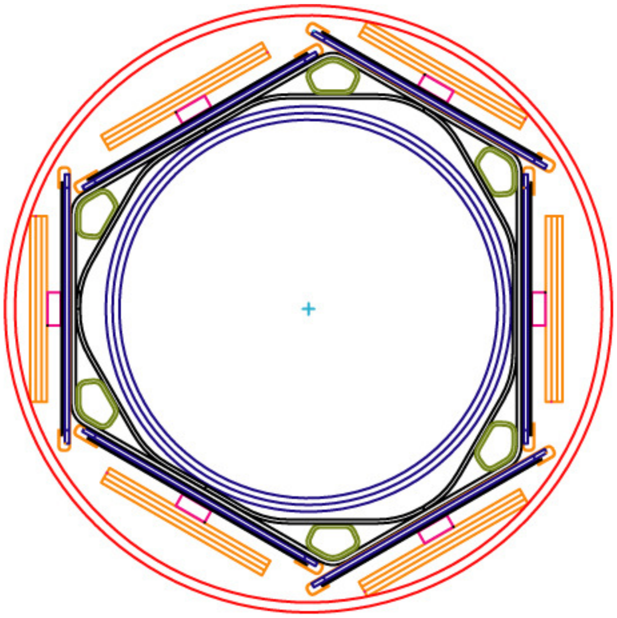

Figure 3.9. Cross-sectional view of the Layer 0 detector.

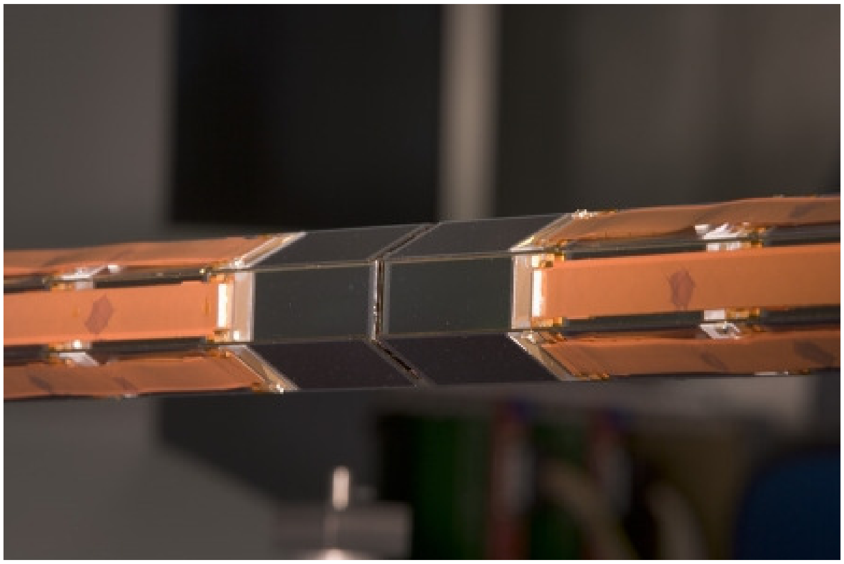

Figure 3.10. Layer 0 low mass cables connected to silicon sensors.

Chips are mounted onto ceramic hybrids, shown in Fig. 3.11, located outside of the tracking volume on the carbon fiber support structure. All downstream electronics are nearly identical to the Run IIa silicon readout.

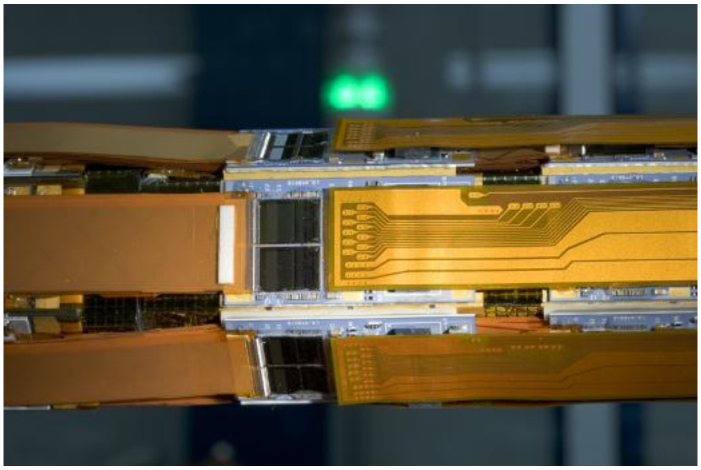

Figure 3.11. SVX4 chips mounted on ceramic hybrids.

The Layer 0 detector design is based off of that of the SMT barrel detectors. Eight barrels are lined along the z-axis, each containing six single-layer silicon ladders. The design has a six-fold symmetry. Sensors are mounted directly onto the carbon fiber structure, which is supported by the beam pipe. Each sensor has 256 channels and is read out by two 128-channel SVX4 chips. Compared to the Run IIa silicon detector, the impact parameter resolution is improved by a factor of 1.5 due to the proximity of Layer 0 to the interaction point. This tracking resolution was accomplished by keeping the signal to noise ratio higher than 10. Dedicated noise studies helped achieve a signal to noise ratio of $\sim$ 18, as shown in Fig. 3.12.

	Layer 0	Barrels	F-Disks	H-Disks
Channels	12288	387,072	258,048	73,728
Modules	48	432	144	48
Silicon Area	852.3 cm^2	1.3 m^2	0.4 m^2	0.65 m^2
Inner Radius	1.60 cm	2.7 cm	2.6 cm	9.5 cm
Outer Radius	1.76 cm	10.5 cm	10.0 cm	26 cm

Table 3.2. Run IIb Silicon Microstrip Tracker detector specifications.

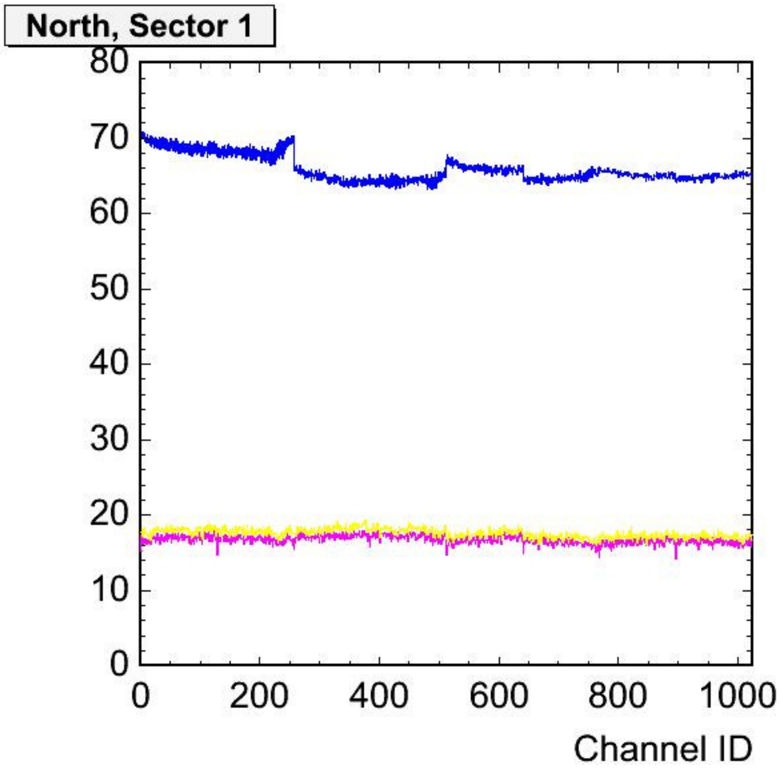

Figure 3.12. Readout of four North sector Layer 0 sensors. Blue is the pedestal, magenta is the total noise, and yellow is the random noise. Noise is multiplied by a factor of 10. Signal to noise ratio is ~ 18.

3.5.3. Central Fiber Tracker (CFT)

The CFT consists of 835 μm scintillating fibers mounted onto eight concentric support cylinders occupying the detector region from 20 to 52 cm from the center of the beam pipe. The two innermost cylinders are 1.66 m long and the outer six cylinders are 2.52 m long. The outer cylinder provides coverage up to $|\eta| < 1.7$. Charged particles passing through the scintillating material of the CFT ionize and create photons. The photons are guided through clear fiber waveguides to a Visible Light Photon Counter (VLPC), a high-efficiency photo-detector, for read out. The CFT contains 76,800 individual scintillating fibers grouped in doublet layers. One layer is oriented along the z-axis, while another is at ±3° stereo angle. This configuration allows for 3D track reconstruction with $\sim$100μm resolution.

3.5.4. Solenoidal Magnet

The central tracking system is surrounded by a 2T superconducting solenoidal magnet. It is 2.73 m in length and has an outer diameter of 1.42 m, with a thickness of $\sim$1 radiation lengths (X_0) at $\eta = 0$. It was designed [**27, 28**] to optimize the momentum resolution, $\delta p_T/p_T$, and tracking pattern recognition. The addition of the solenoidal magnet for central tracking system made a substantial improvement in the DØ low p_T program. It provides a good measurement of momentum and charge of the particles including muons, since muon momentum resolution from the central tracking system is much better than that from the stand-alone muon system. It enhances the physics reach of DØ, specially in the forward region.

3.6. Preshower Detectors

The preshower detector system consists of a central preshower (CPS) detector, located between the solenoid and the central calorimeter cryostat, and two forward preshower (FPS) detectors, mounted on the inner surface of each end calorimeter. They combine features of both calorimeters and tracking detectors, and enhance the spatial matching between tracks and calorimeter showers. The central preshower detector was designed to improve electron identification and to correct for effects in the tracking system. The CPS detector covers the region $|\eta| < 1.2$. It is located between the solenoid and the central calorimeter, with an inner radius of 71.8 cm and an outer radius of 74.2 cm. The two FPS detectors cover the range $1.5 < |\eta| < 2.5$. The preshower detectors can be seen in Fig. 3.3.

3.7. Calorimeter

The calorimeter system provides energy measurements for electrons, photons and jets. It is composed of three uranium liquid-argon calorimeters; the central calorimeter (CC) centered in the interaction region ($|\eta| \leq 1$), and two end cap (EC) calorimeters in the forward regions ($1 \leq |\eta| \leq 4$).

Both the CC and EC consists of three sections: An electromagnetic section with thin ($\sim$4 mm) depleted uranium plates, fine hadronic modules with 6 mm thick uranium-niobium alloy plates, and a course hadronic section made from $\sim$47 mm thick copper (in the CC) and stainless steel (in the EC) plates.

These sections were designed to provide energy measurements for electromagnetic particles (electrons and photons), hadronic particles (jets), as well as assist in identification of electrons, photons, jets, and muons as well as measure the transverse energy balance in events. The calorimeters themselves are unchanged from Run I, described in detail in [**24**] and are illustrated in Fig. 3.13.

3.8. Muon System

The muon system is the outermost detection layer at DØ. The layer closest to the interaction region consists of a single layer of muon detectors, followed by a 1.8T toroidal magnet, then two additional layers of muon detectors. In the central region, proportional drift tubes (PDTs) provide coverage for $|\eta| \lesssim 1.0$. Mini-drift tubes (MDTs) extend coverage in the forward region to $|\eta| \approx 2.0$, and includes trigger scintillation counters and beam pipe shielding, allowing for better trigger and muon identification coverage. During Run I, a set of scintillation counters, the cosmic cap [**29**], was installed on the top and upper sides of the outer layer of central muon PDTs. This coverage has been extended to the lower sides and bottom of the detector, to form the cosmic bottom. These trigger scintillation counters are fast enough to allow us to associate a muon in a PDT with the

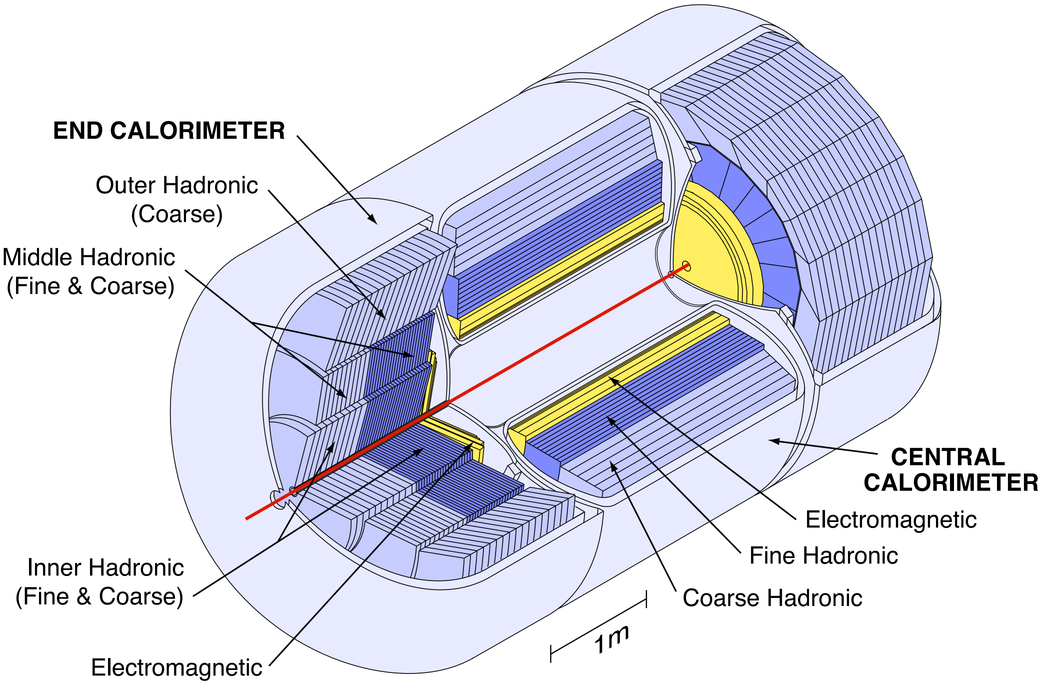

Figure 3.13. Isometric view of the central and two end calorimeters.

appropriate bunch crossing and to reduce the cosmic ray background. Additional scintillation counters, the $A\phi$ counters, have been installed on the PDTs mounted between the calorimeter and the toroidal magnet. The $A\phi$ counters provide a fast detector for triggering and identifying muons and for rejecting out-of-time background events.

The scintillation counters are used for triggering; the wire chambers are used for precise coordinate measurements as well as for triggering. Both types of detectors contribute to background rejection: the scintillator with timing information and the wire chambers with track segments.

Muon detector components are discussed in the following sections; original components are described briefly. Exploded views of the muon system are shown in Fig.s 3.14 and 3.15.

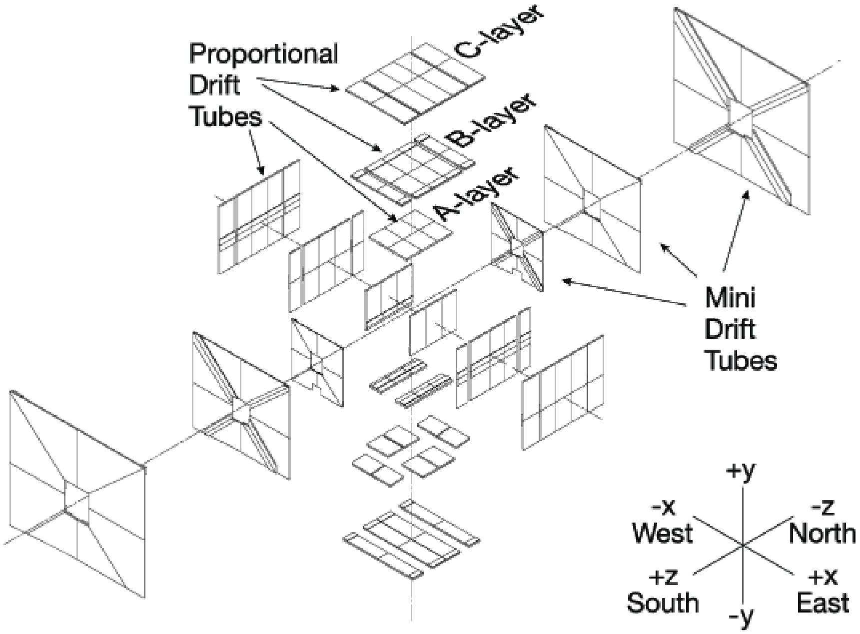

Figure 3.14. Muon wire chambers.

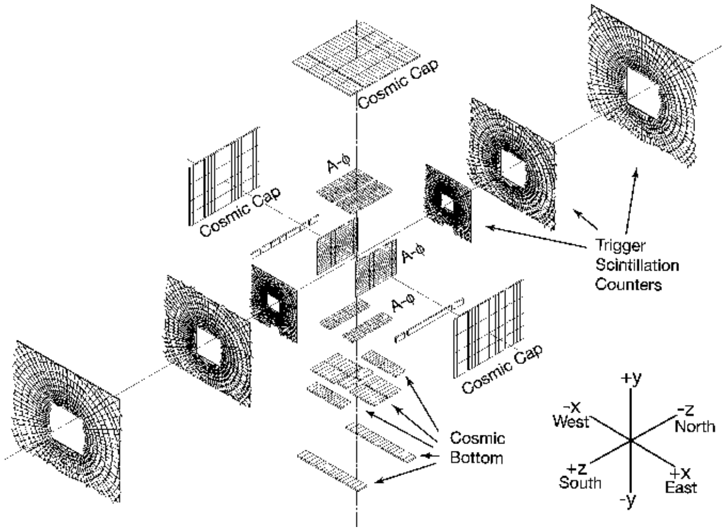

Figure 3.15. Muon scintillation counters.

3.9. Trigger System

The DØ trigger system is a three-tiered decision process optimized to select and record only the most interesting physics events. The first two levels are hardware triggers, while the third level is software based. The Level 1 trigger accepts events at a rate of about 2 kHz. At Level 2, the trigger rate is reduced by half to about 1 kHz. Events passing Level 1 and Level 2 are passed to Level 3 where software algorithms further reduced the rate to about 50 Hz, sending selected events to be recorded for offline reconstruction. An overview of the DØ trigger system and data acquisition system is shown in Fig. 3.16. A block diagram of the L1 and L2 trigger systems is shown in Fig. 3.17.

Trigger	Accept rate (Hz)	Decision time (μs)
Events	7.6×10^6	
Level 1	2×10^3	4.2
Level 2	1×10^3	100
Level 3	20-50	$100\text{-}150\times10^3$

Table 3.3. DØ Trigger rates. The accept rate is the number of events per second that are passed to the next decision level. The Level 3 accept rate is the number of events per second that are recorded to tape.

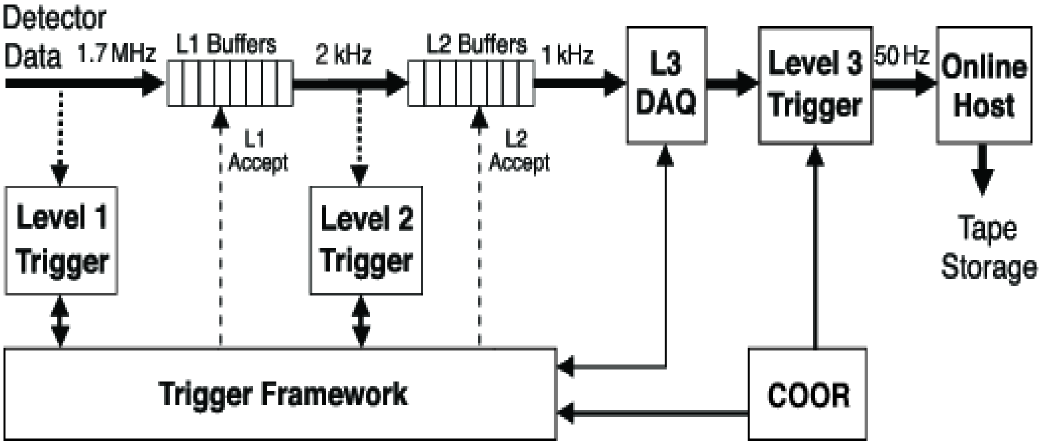

Figure 3.16. Overview of the DØ trigger and data acquisition systems.

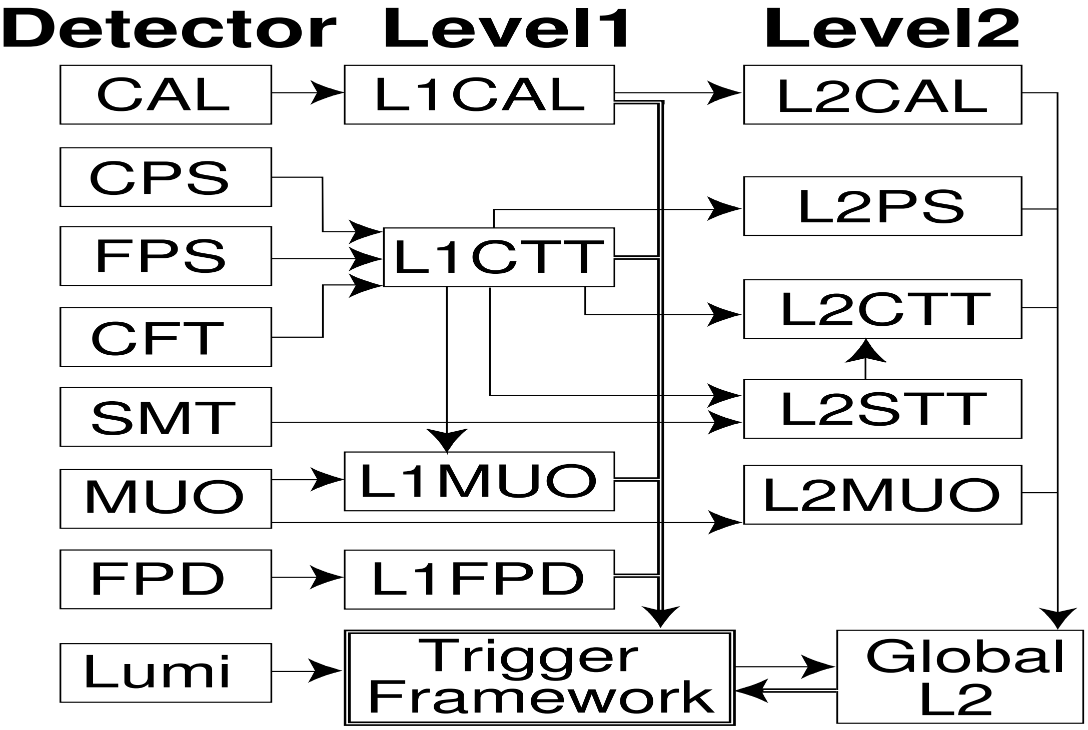

Figure 3.17. Block diagram of the DØ L1 and L2 trigger systems. The arrows show the flow of trigger-related data.

CHAPTER 4

Study of CP Violation in $B_s^0 \to J/\psi\phi$ Decays

4.1. Introduction

This chapter presents a study of CP violation in flavor-tagged $B_s^0 \to J/\psi\phi$ decays using a 2.8 fb^{-1} data sample collected by the DØ Run II detector from April 2002 to August 2007. While this is not the first study of $B_s^0 \to J/\psi\phi$ decays at the Tevatron, it is the first to use flavor tagging to improve the measurement of the CP-violating phase at DØ. It provides important tests of the CKM mechanism in the SM, as discussed in section 2.5.

This study measures the width difference $\Delta\Gamma_s$ between the Light and Heavy B_s^0 mass eigenstates, B_s^L and B_s^H, and the CP-violating phase ϕ_s in flavor-tagged $B_s^0 \to J/\psi\phi$ decays. The B_s^0 meson is reconstructed in this channel by searching for a J/ψ meson decaying to $\mu^+\mu^-$ and a ϕ meson decaying to K^+K^-. The J/ψ and ϕ are then combined to form the B_s^0 candidate. A combined opposite-side and same-side flavor tag is applied to the B_s^0 candidate to determine its flavor at the time of production (whether is was produced as a B_s^0 or $\bar{B}_s^0$ at time t = 0). Using the mass, lifetime, and polarization amplitudes of the three decay angles, a maximum likelihood fit is performed on the entire sample. From this, the width difference $\Delta\Gamma_s$ and CP-violating phase ϕ_s are measured.

This chapter is organized in the following way: First, the main contributions to B meson production at the Tevatron are presented. This is followed by a discussion of the data and Monte Carlo (MC) samples used in this study. Details of the B_s^0 event reconstruction, flavor tagging method, variables used in the fit, and the fitting procedure are then described. The final results for the width difference $\Delta\Gamma_s$ and CP-violating phase ϕ_s in the B_s^0 meson system are presented at the end of this chapter, along with a discussion of the systematic uncertainties associated with the measurement. Comparison plots between data and MC for p_T distributions of the reconstructed particles are provided in Appendix A.

4.2. B Meson Production at the Tevatron

There are thought to be three main b-quark production mechanisms in $p\bar{p}$ collisions at the Tevatron: Flavor creation, flavor excitation, and parton showers [**30**]. The Feynman diagrams showing the leading order processes for b-quark production via flavor creation are given in Fig. 4.1, where gluon-gluon fusion, $g + g \rightarrow b + \bar{b}$, is the dominant process at the Tevatron. Flavor excitation refers to the $b(\bar{b})$-quark scattering out of the initial state (proton) into the final state via a gluon or light quark. The third mechanism, parton showers, refers to b-quarks produced during fragmentation processes, rather than during the initial hard scattering process.

Once a $b\bar{b}$ pair is produced it hadronizes to form a pair of B mesons. The measured fractions of $B^{\pm}$, B_d^0, B_s^0 and b-baryons produced at the Tevatron are (assuming an equal fraction for $B^{\pm}$ and B_d^0) [**31**]:

$$\begin{aligned} f_u &= 0.375 \pm 0.023, \\ f_d &= 0.375 \pm 0.023, \\ f_s &= 0.160 \pm 0.044, \\ f_{baryon} &= 0.090 \pm 0.029. \end{aligned} \tag{4.1}$$

4.3. Di-muon Data Sample

Events containing B mesons produced inside the DØ detector which are selected by the Level 3 trigger are recorded to tape in the thumbnail format and transferred

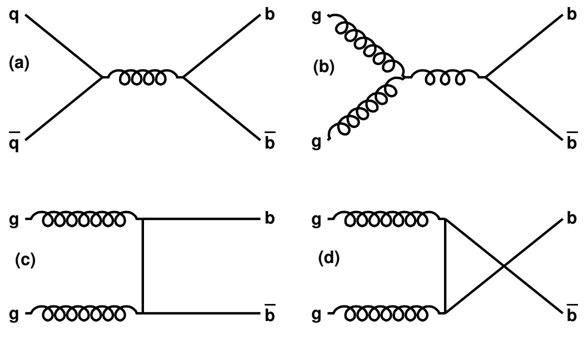

Figure 4.1. Feynman diagrams showing leading order b-quark production processes at the Tevatron. Quark annihilation is shown in (a), and gluon-gluon fusion in (b)–(d).

to Sequential data Access via Meta-data (SAM) for permanent storage. Skims for B-physics analyses of these events are created and saved in AADST format. The standard B-physics ANAlysis package (BANA) [**32**] is used in this study to reconstruct the $B_s^0 \to J/\psi(\mu^+\mu^-)\phi(K^+K^-)$ decay.

The full inclusive di-muon sample, which corresponds to 2.8 fb^{-1} of integrated luminosity collected by the DØ detector between April 2002 and August 2007 is used for this study. This sample is selected by requiring two reconstructed muons with the following requirements:

- each muon has $p_T > 1.5$ GeV/c;
- each muon is detected as a track segment in at least one layer of the muon system;
- each muon is matched to a central track;
- at least one muon is measured inside and outside the toroid.

Events where the data from the muon or central tracking systems are labelled as bad are rejected. Events are also required to satisfy a muon trigger that does not include a cut on the impact parameter. This reduces any bias on physical measurements relevant to this study.

4.4. Monte Carlo Event Samples

Generated Monte Carlo (MC) samples of decay processes using a full detector simulation give a more complete understanding of the detector response to real physical processes. They also provide a cross-check to test the validity of the procedure.

The SVV_HELAMP model [**33**] in the $EvtGen$ generator (interfaced to $Pythia$ [**34**]) is used to simulate the decay chain $B_s^0 \to J/\psi\phi$, $J/\psi \to \mu^+\mu^-$, $\phi \to K^+K^-$. The decay amplitude (A) is specified by the helicity amplitudes (H) which are given as arguments for the decay. The arguments are H_+, H_0, and H_-, specified as the magnitude and phase ($|H_+|$, H_+^{phase}, $|H_0|$, H_0^{phase}, $|H_-|$, H_-^{phase}). Three samples with different polarization states were generated:

- (0.0, 0.0, 1.0, 0.0, 0.0, 0.0) corresponding to A_0=1, $A_{||}$=0, $A_\perp$=0 in the linear polarization basis;
- With H_i parameters (1.0, 0.0, 0.0, 0.0, 1.0, 0.0) corresponding to A_0=0, $A_{||}$=1, $A_\perp$=0;
- (1.0, 0.0, 0.0, 0.0, -1.0, 0.0) corresponding to A_0=0, $A_{||}$=0, $A_\perp$=1.

The B_s^0 mean proper lifetimes for the CP-even ($A_{||}$=1 or A_0=1) and CP-odd ($A_\perp$=1) states were set to the expected SM values of 370 μm and 460 μm, respectively, in the $EvtGen$ [**33**] ptable file.

The decay $J/\psi \to \mu^+\mu^-$ is simulated using the VLL model of the PHOTOS package. The VSS model is used in the decay $\phi \to K^+K^-$. The amplitude for this decay is given by $A = \varepsilon^\mu v_\mu$ where ε is the polarization vector of the parent particle and the v is the velocity (obtained from the four momentum vector) of the first daughter. The definition of the CP-even state under `EvtGen` is given below as an example:

```
noMixing


Alias myJ/psi J/psi
Alias myphi phi
```

```
Decay anti-B_s0
1.000    myJ/psi   myphi            SVV_HELAMP 1.0 0.0 0.0 0.0 -1.0 0.0;
Enddecay
Decay myJ/psi
1.000    mu+  mu-              PHOTOS  VLL;
Enddecay
Decay myphi
1.000   K+   K-                        VSS;
Enddecay
End
```

Before passing the generated events through the chain of programs for the detector simulation, hit simulation, and track and particle reconstruction, the following "pre-GEANT" selection cuts on the event generator output are applied:

- presence of the decay chain $\bar{B}_s^0 \to J/\psi\phi$.
- $p_T(\mu) > 1.5$ GeV/c for both muons.
- $0.8 < |\eta(\mu)| < 2.0$ or $p_T(\mu) > 3$ GeV/c.
- $0.8 < |\eta(\mu)|$ for the second muon.
- $p_T(K^{\pm}) > 0.5$ GeV/c.
- $p_T(\phi) > 0.7$ GeV/c.
- $p_T(B_s^0) > 4.0$ GeV/c.

The number of reconstructed events passing the above cuts for each pure polarization state is about 18.5 K. The reconstructed events in "d0reco" format are stored in the SAM system. The dataset definition is called "DGOG_CPodd_CPeven_A0_Apara".

4.5. Vertex Reconstruction

The accurate determination of primary and secondary vertex locations in an event is an essential component of this analysis, and critical for measuring the lifetime of the

B_s^0 meson. Vertex finding algorithms, based on an interative process, are used to identify tracks originating from a vertex. For each event, the primary vertex is reconstructed using a set of selected tracks and the beam-spot position, where the beam-spot is the interaction zone of the $p\bar{p}$ beams of the Tevatron. The beam-spot is measured using events containing a vertex formed from at least 3 tracks with hits in the Silicon Microstrip Tracker detector.

4.5.1. Primary Vertex

The primary vertex position is obtained by minimizing a χ^2 funtion [**35**]. A key element of the primary vertex reconstruction is the selection of tracks, as well as the rejection of poorly measured tracks. Tracks with wrong hit associations in the SMT detector, in addition to those coming from decays of long-lived particles or from interactions in the detector material, bias the fitted primary vertex position. A special rejection procedure helps reduce this bias.

For the primary vertex computation, tracks with at least two measurements in $R\phi$ and at least one measurement in Rz are selected. A fit using all tracks selected with these requirements (N_{tr}) is performed and $\chi(N_{tr})$ is computed. Next, each track is consecutively removed and the corresponding $\chi^2(N_{tr} - 1)$ is obtained. The given track providing the maximum difference $\chi^2(N_{tr}) - \chi(N_{tr} - 1)$ is excluded from the fit if this difference exceeds a specified threshold value Δ, where Δ is set to 6. This step is repeated as long as there are tracks with a χ^2 difference exceeding Δ.

4.5.2. Secondary Vertex

A secondary vertex is searched for in each event. First, all possible combinations of pairs of tracks are selected as secondary vertex candidates. The requirement on these pairs is that they have a common vertex with the χ^2 value of the fit to be less than 4. Next, all tracks are tested individually for inclusion in a given secondary vertex candidate. The track which produces the smallest change Δ of the vertex fit χ^2 is included in the secondary vertex candidate only if this change does not exceed the threshold value $\Delta = 5$, as determined by optimising the efficiency of the secondary vertex reconstruction algorithm. This procedure is repeated until all tracks satisfying the threshold requirement are included in the secondary vertex candidate. The secondary vertex candidate is rejected if the distance to the primary vertex divided by its error is less than 3.

4.6. $B_s^0 \to J/\psi(\mu^+\mu^-)\phi(K^+K^-)$ Decay Reconstruction

The decay topology of $B_s^0 \to J/\psi(\mu^+\mu^-)\phi(K^+K^-)$ is shown in Fig. 4.2. The J/ψ and ϕ decays are governed by the electromagnetic and strong force respectively, so their decay products seem to come directly out of the B_s^0 decay vertex. B meson decays, on the other hand, are governed by the weak force and they are long-lived particles. As a result, they travel a significant distance (several hundred microns) from the primary vertex before decaying.

The J/ψ candidate is reconstructed from two oppositely charged muon tracks. The ϕ candidate is reconstructed by assigning the kaon mass to all oppositely charged track pairs, except those tracks used to form the J/ψ candidate. A B_s^0 candidate is formed by combining all pairs of J/ψ and ϕ candidates. The primary vertex is reconstructed from all tracks in the event with $p_T > 0.3$ GeV/c, except those used to form the B_s^0 candidate, with a constraint applied to the average beam spot position. An event is saved if at least one B_s^0 candidate is found.

4.6.1. Initial Event Selection

Two oppositely charged muon tracks with $p_T > 1.5$ GeV/c are used to reconstruct the J/ψ vertex. The invariant mass of the J/ψ vertex is required to be in the range 2.9 to 3.3 GeV/c^2. Successful J/ψ candidates are constrained to the world average mass of the J/ψ meson [**36**] to improve the mass resolution of the B_s^0 candidates.

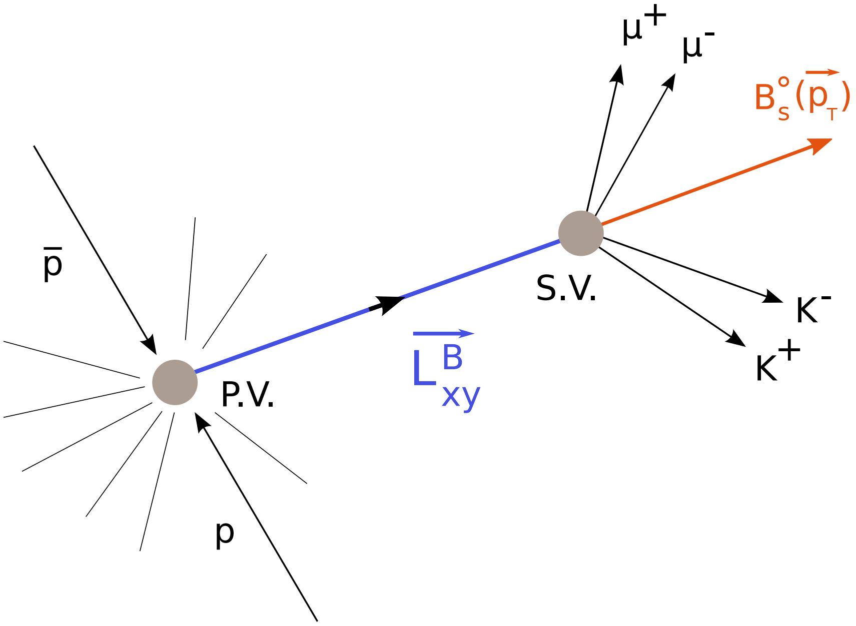

Figure 4.2. An illustration of the B_s^0 decay topology, where P.V. is the primary vertex and S.V. is the secondary vertex.

The ϕ vertex is reconstructed using all pairs of tracks with $p_T > 0.7$ GeV/c. Tracks used to form the J/ψ vertex are explicitly rejected. The invariant mass of the ϕ vertex is required to be in the range 1.01 to 1.03 GeV/c^2.

Combining successful J/ψ and ϕ candidates together gives the initial B_s^0 candidate sample. The invariant mass of the B_s^0 candidate is required to be in the range 5.0 to 5.8 GeV/c^2. The initial event selection cuts are listed in Table 4.1.

Quantity	Cut
p_T of μ^+, μ^-	> 1.5 GeV/c
p_T of K^+, K^-	> 0.7 GeV/c
J/ψ candidate mass	$2.9 < M(\mu^+, \mu^-) < 3.3$ GeV/c^2
ϕ candidate mass	$1.01 < M(K^+, K^-) < 1.03$ GeV/c^2
B_s^0 candidate mass	$5.0 < M(\psi, \phi) < 5.8$ GeV/c^2

Table 4.1. Summary of initial event selection cuts.

4.6.2. Final Event Selection

The final B_s^0 candidate sample is selected after applying further kinematic and quality cuts to the initial event sample. Transverse momentum cuts are necessary to optimize the signal to background ratio. The p_T cuts are set at 6.0 GeV/c for B_s^0 candidates, 1.5 GeV/c for ϕ candidates, and 0.7 GeV/c for each ϕ decay product.

The B_s^0 candidate sample is selected by requiring a $(J/\psi, \phi)$ pair to be consistent with that coming from a common vertex, and to have a mass in the range 5.0 to 5.8 GeV/c^2. J/ψ candidates are accepted if the unconstrained invariant mass resulting from the vertex fit is in the range 2.9 to 3.3 GeV/c^2. ϕ candidates are required to satisfy a fit to a common vertex, and to have the invariant mass in the range 1.01 to 1.03 GeV/c^2. In case of multiple ϕ meson candidates, the one with the highest p_T is selected. MC studies show that the p_T spectrum of the ϕ mesons coming from B_s^0 decay is harder than the spectrum of a pair of random tracks from hadronization.

Quantity	Cut
p_T of μ^+, μ^-	> 1.5 GeV/c
p_T of K^+, K^-	> 0.7 GeV/c
p_T of ϕ	> 1.5 GeV/c
p_T of B_s^0	> 6.0 GeV/c
J/ψ candidate mass	$2.9 < M(\mu^+, \mu^-) < 3.3$ GeV/c^2
ϕ candidate mass	$1.01 < M(K^+, K^-) < 1.03$ GeV/c^2
B_s^0 candidate mass	$5.0 < M(\psi, \phi) < 5.8$ GeV/c^2
Decay length error of B_s^0 candidate	< 0.006 cm
SMT hits on track	> 1
χ^2 of B_s^0	< 30.0

Table 4.2. Summary of final event selection cuts.

The signed decay length of a B_s^0 meson, L_{xy}^B, is defined as the vector pointing from the primary vertex (P.V.) to the secondary (decay) vertex (S.V.) projected onto the transverse momentum of the B_s^0 meson, as illustrated in Fig. 4.2. The primary vertex is reconstructed from tracks with $p_T > 0.3$ GeV/c. Tracks which are used as decay products of the B_s^0

candidate are explicitly rejected. A constraint to the average beam spot position is applied when forming the vertex.

The proper decay length, ct, is defined as:

$$ct = L_{xy}^{B} \cdot M_{B_s^0}/p_T, \tag{4.2}$$

where $M_{B_s^0} = 5.3675$ GeV/c^2 is the PDG value of the B_s^0 mass [**36**]. The distribution of the proper decay length uncertainty $\sigma(ct)$ of B_s^0 mesons peaks around 25 μm, as shown in the bottom plot in Fig 4.4. Only events with $\sigma(ct) < 60$ μm are accepted. See Appendix B for a study comparing the effects of changing the $\sigma(ct)$ cut on the results.

The invariant mass distribution of the accepted 48047 B_s^0 candidates is shown in Fig. 4.3 (top) while with $ct/\sigma(ct) > 5$ cut is shown in Fig. 4.3 (bottom). The curves are projections of the maximum likelihood fit, described in Section 4.8. The fit assigns 1967±65 (stat) events due to the B_s^0 decay. Fig. 4.4 shows the distribution of the proper decay length (top) and its error (bottom). The final event selection cuts are tabulated in Table 4.2. These events are used in this study to measure the width difference and CP-violating phase.

The background is divided into two categories based on its origin and lifetime characteristics: "Prompt" background and "non-prompt" background. Prompt background is due to directly produced J/ψ mesons associated with random tracks arising from hadronization. This background is distinguished from non-prompt background, where the J/ψ meson is a product of a $B-$hadron decay, while the tracks forming the ϕ candidate arise from a multi-body decay of the same $B-$hadron, or from the underlying event. In this study, "prompt" events are defined to have the condition $ct/\sigma(\text{ct}) < 5$. This value is chosen to minimize the number of poorly reconstructed B_s^0 candidates. The signal region is defined as $5.26 < M(B_s^0) < 5.42$ GeV/c^2 and the background region as $M(B_s^0) < 5.2$ GeV/c^2 or $M(B_s^0) > 5.5$ GeV/c^2.

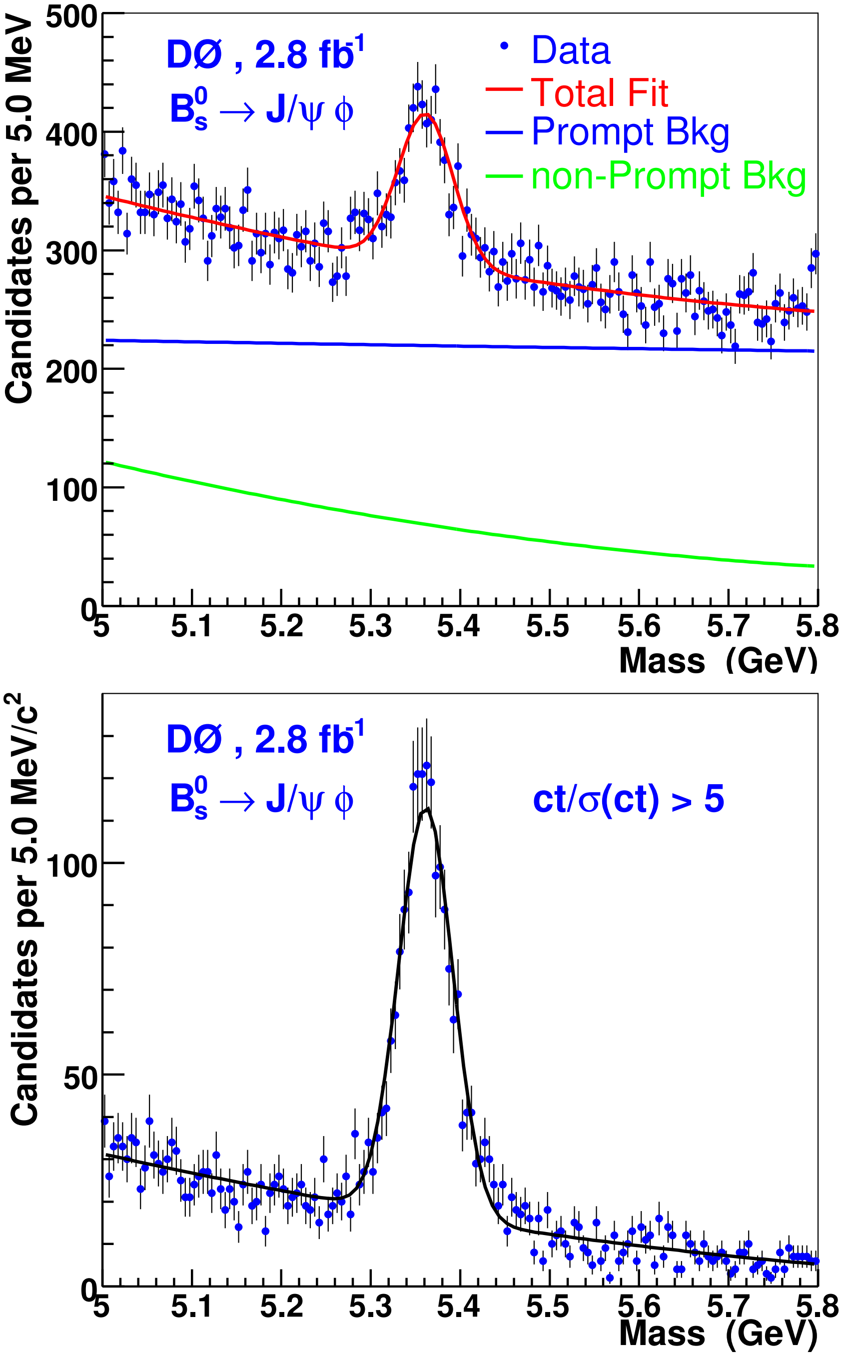

Figure 4.3. The invariant mass distribution of the $(J/\psi, \phi)$ system for B_s^0 candidates. Top: All 48047 B_s^0 candidate events. The curves are the projections of the maximum likelihood fit: Prompt background, non-prompt background, and the total. Bottom: A subsample with the prompt background suppressed. The curve is a fit to a Gaussian distribution and a quadratic background.

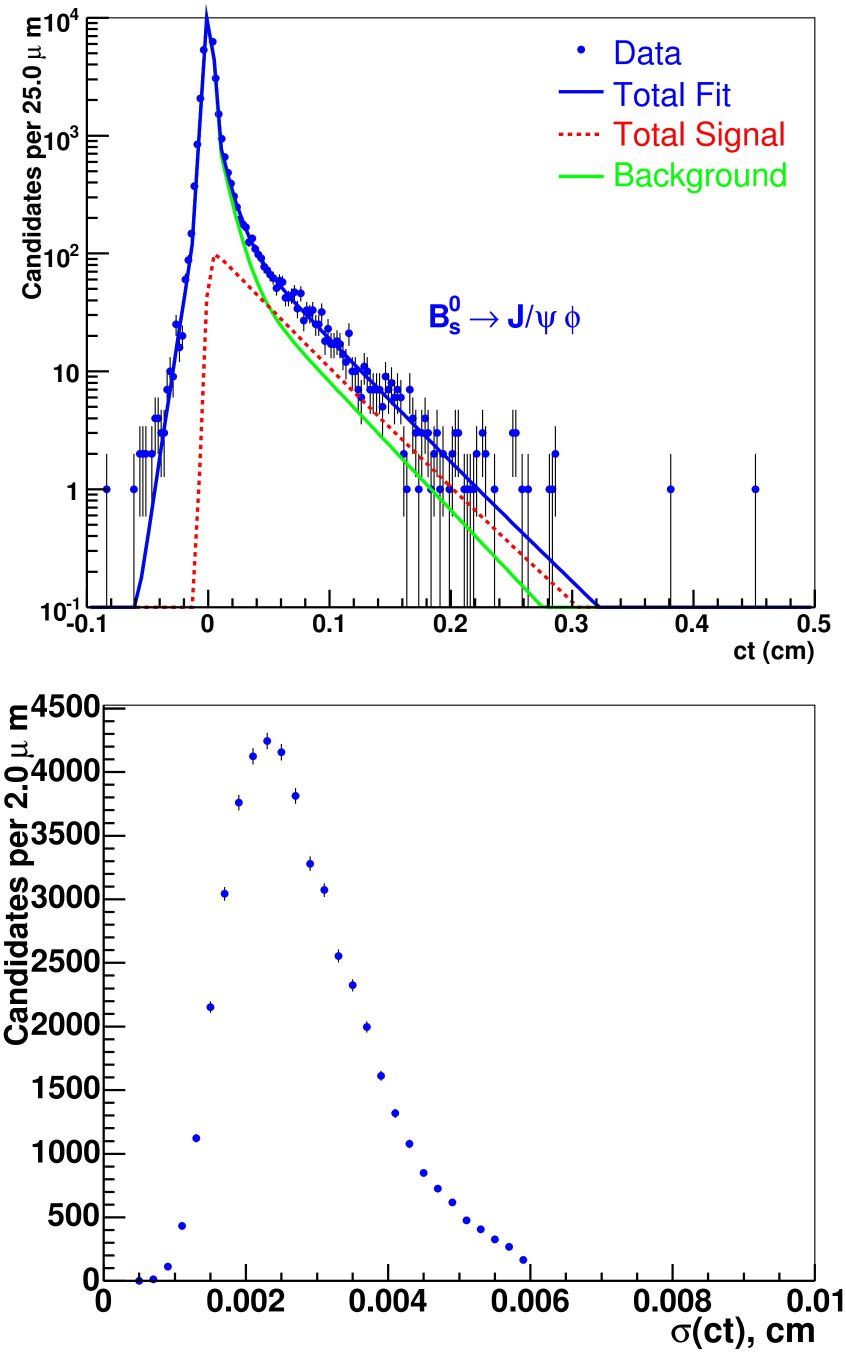

Figure 4.4. Top: The proper decay length, ct, of the B_s^0 candidates. The curves are the projections of the maximum likelihood fit: The signal contribution, dotted (red); the background, light solid (green); and total, solid (blue). Bottom: Distribution of the proper decay length uncertainty ($\sigma(ct)$) of the B_s^0 candidates.

4.7. Flavor Tagging

Flavor tagging is a method of determining the flavor (B or $\bar{B}$) of a B meson. Since b-quarks are generally produced in $b\bar{b}$ pairs at the Tevatron, decay and hadronization properties of both quarks can be used in the tagging procedure. For this study, "opposite-side tagging" and "same-side tagging" methods were combined and used to determine the initial ($t = 0$) state of the reconstructed B_s^0 meson. Here, opposite-side tagging refers to the side opposite to the reconstructed B_s^0 meson and same-side tagging refers to the side of the reconstructed B_s^0 meson, as illustrated in the reconstructed decay $B_s^0 \to J/\psi(\mu^+\mu^-)\phi(K^+K^-)$ in Fig. 4.5. The combination of these taggers gives a significant improvement over the use of individual tagging methods.

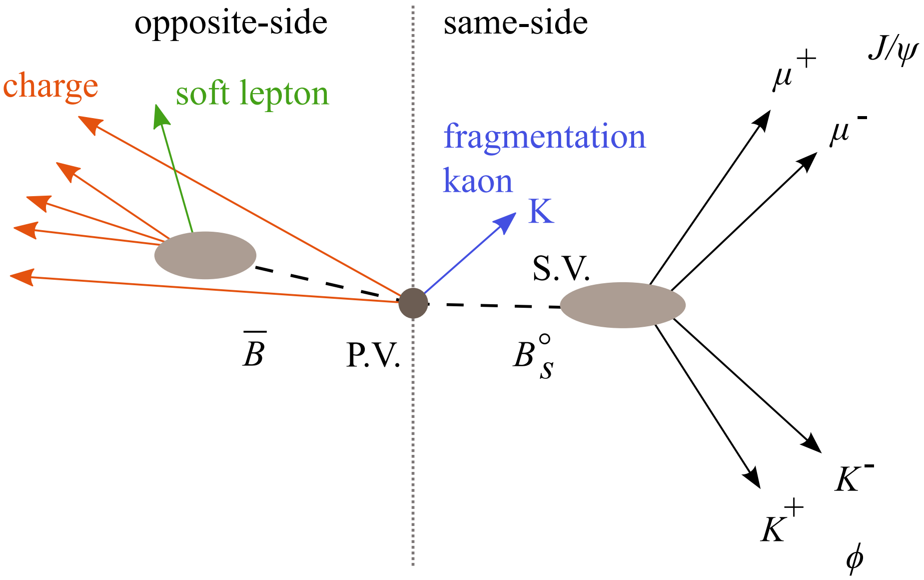

Figure 4.5. An illustration of an event with a reconstructed $B_s^0 \to J/\psi(\mu^+\mu^-)\phi(K^+K^-)$ decay.

4.7.1. Initial State Combined Flavor Tagging

The flavor of the initial state of the B_s^0 meson is determined using a likelihood ratio method described in detail in [**37**]. A set of discriminating variables $x_1, ..., x_n$, which have different distributions for b and $\bar{b}$ flavors, are constructed for each event. For the initial b quark, the probability density function (PDF) for a given variable x_i is denoted as $f_i^b(x_i)$, while for the initial $\bar{b}$ quark it is denoted as $f_i^{\bar{b}}(x_i)$. The combined tagging variable r is defined as:

$$r = \prod_{i=1}^{n} r_i;\ r_i = \frac{f_i^{\bar{b}}(x_i)}{f_i^b(x_i)}. \tag{4.3}$$

If a variable x_i cannot be defined for a given event, the corresponding variable r_i is set equal to 1. With this definition, an initial b flavor is more probable if $r < 1$, and a $\bar{b}$ flavor is more probable if $r > 1$. By construction, an event with $r < 1$ is tagged as a b quark and an event with $r > 1$ is tagged as a $\bar{b}$ quark. For convenience, the tagging variable is redefined as:

$$d = \frac{1-r}{1+r}, \tag{4.4}$$

where the variable d ranges between -1 and 1. Under this construction, an event with $d > 0$ is tagged as a b quark and with $d < 0$ as a $\bar{b}$ quark. Higher $|d|$ values correspond to higher tagging purities. For uncorrelated variables $x_1, ..., x_n$, and perfect modeling of the PDF, d gives the best possible tagging performance. Its absolute value is related with the value of dilution $\mathcal{D}$ of the flavor tagging defined as:

$$\mathcal{D} = \frac{N_{\text{cor}} - N_{\text{wr}}}{N_{\text{cor}} + N_{\text{wr}}}, \tag{4.5}$$

where N_{cor} (N_{wr}) is the number of events with correctly (wrongly) identified initial B_s^0 meson flavor. The effective tagging power $\mathcal{P}$, used as a figure of merit while comparing the performance of tagging algorithms, is given by:

$$\mathcal{P} = \varepsilon\mathcal{D}^2;\ \varepsilon = \frac{N_{\text{cor}} + N_{\text{wr}}}{N_{\text{tot}}}, \tag{4.6}$$

where N_{tot} is the total number of B_s^0 mesons, and ε gives the efficiency of the flavor tagging.

The discriminating variables are constructed using the properties of the b quark opposite to the reconstructed B meson (opposite-side tagging) and the properties of particles accompanying the reconstructed B meson (same-side tagging).

4.7.2. Opposite-side Tagging Discriminating Variables

Opposite-side tagging is used to infer the flavor of the reconstructed B meson by identifying the flavor of the B meson opposite to the reconstructed one, assuming that b and $\bar{b}$ quarks are produced in pairs[1]. One advantage of this method is that its performance does not depend on the type of reconstructed B meson. The opposite-side tagging uses charge correlations (lepton charge, secondary vertex charge, and event charge) of the opposite-side B hadron to determine its flavor.

In the case of the lepton charge, an additional muon is searched for in each event. This muon is required to have at least one hit in the muon chambers, and to satisfy the condition $\cos\phi(\mathbf{p}_\mu, \mathbf{p}_B) < 0.8$, where $\mathbf{p}_B$ is the three-momentum vector of the reconstructed B meson and ϕ is the angle between vectors $\mathbf{p}_\mu$ and $\mathbf{p}_B$. If multiple muons satisfy these conditions, the muon with the highest number of hits in the muon chambers and the highest p_T is used. Selecting a muon candidate, a *muon jet charge* Q_J^μ is constructed as:

$$Q_J^\mu = \frac{\sum_i q^i p_T^i}{\sum_i p_T^i}, \tag{4.7}$$

where q^i is the charge and p_T^i is the transverse momentum of the i^{th} particle. The sum is taken over all charged particles, including the muon, found within a cone of radius $\Delta R = \sqrt{(\Delta\phi)^2 + (\Delta\eta)^2} < 0.5$, where $\Delta\phi$ and $\Delta\eta$ are computed with respect to the muon direction. Decay products of the reconstructed B meson are explicitly excluded from this sum. In addition, any charged particle with $\cos\phi(\mathbf{p}, \mathbf{p}_B) > 0.8$ are excluded. This p_T-weighted cone charge is used to estimate the charge associated with the hadronization of a potential b or $\bar{b}$ quark.

---

[1] Due to baryon number conservation.

In addition to the muon tag, reconstructed electrons with $\cos\phi(\mathbf{p}_e, \mathbf{p}_B) < 0.8$ are also used for the opposite-side flavor tag. The electron is reconstructed by matching a track to the calorimeter and summing the energy deposited in a narrow tube around the track. Electrons are required to be in the central region ($|\eta| < 1.1$), with $p_T > 2$ GeV/c, have at least one hit in the CFT and SMT, and to have energy deposits in the EM calorimeter consistent with an electron. For this electron candidate, similar to the muon, an *electron jet charge* Q^e_J is constructed as:

$$Q^e_J = \frac{\sum_i q^i p^i_T}{\sum_i p^i_T}. \tag{4.8}$$

The sum is taken over all charged particles, including the electron, with $\Delta R < 0.5$, similar to the muon charge.

A secondary vertex corresponding to the decay of B mesons is also searched for using all charged particles in the event. The secondary vertex is required to contain at least two tracks with axial impact parameter significance greater than 3. The distance l_{xy} from the primary to the secondary vertex should satisfy the condition: $l_{xy} > 4\sigma(l_{xy})$. The details of the secondary vertex search are given in Ref. [**35**].

The three-momentum of the secondary vertex $\mathbf{p}_{SV}$ is defined as the vector sum of all momenta of tracks included in the secondary vertex. Secondary vertices used for flavor tagging are required to satisfy $\cos\phi(\mathbf{p}_{SV}, \mathbf{p}_B) < 0.8$.

A *secondary vertex charge* Q_{SV} is defined as the third discriminating variable:

$$Q_{SV} = \frac{\sum_i (q^i p^i_L)^\kappa}{\sum_i (p^i_L)^\kappa}, \tag{4.9}$$

where p^i_L is the longitudinal momentum of a given particle with respect to the direction of the secondary vertex momentum. The sum is taken over all tracks included in the secondary vertex. Decay products of the reconstructed B meson are explicitly excluded from the sum. In addition, any charged particles with $\cos\phi(\mathbf{p}, \mathbf{p}_B) > 0.8$ are excluded.

Finally, the *event charge* Q_{EV} is constructed as:

$$Q_{EV} = \frac{\sum_i q^i p_T^i}{\sum_i p_T^i}, \tag{4.10}$$

where the sum is taken over all charged particles with $0.5 < p_T < 50$ GeV/c and having $\cos\phi(\mathbf{p}, \mathbf{p}_B) < 0.8$. Decay products of the reconstructed B meson are explicitly excluded from the sum.

The combination of these discriminating variables is performed using the likelihood ratio method. The performance of the opposite side tagging is measured directly in data using $B \to \mu\nu D^{*\pm}$ events [**37**]. It has been verified that its performance in $B^\pm \to J/\psi K^\pm$ events agrees well with the results of [**37**] and with the MC. The dilution for different $|d|$ values is given in Table 4.3.

$\|d\|$	$\mathcal{D}(B^\pm \to J/\psi K^\pm)$ (%) (MC)	$\mathcal{D}(B^\pm \to J/\psi K^\pm)$ (%) (data)	$\mathcal{D}(B \to \mu\nu D^{*\pm})$ (data) [**37**]
$0.00 < \|d\| < 0.10$	0.038 ± 0.037	0.013 ± 0.054	N/A
$0.10 < \|d\| < 0.20$	0.215 ± 0.047	0.125 ± 0.057	0.084 ± 0.031
$0.20 < \|d\| < 0.35$	0.197 ± 0.035	0.153 ± 0.049	0.236 ± 0.027
$0.35 < \|d\| < 0.45$	0.372 ± 0.038	0.417 ± 0.060	0.385 ± 0.034
$0.45 < \|d\| < 0.60$	0.508 ± 0.040	0.633 ± 0.054	0.512 ± 0.032
$0.60 < \|d\| < 1.00$	0.490 ± 0.078	0.300 ± 0.120	0.597 ± 0.058

Table 4.3. Dilution of opposite-side tagging in MC and real $B^\pm \to J/\psi K^\pm$ events, and in real $B \to \mu\nu D^{*\pm}$ events for different values of the $|d|$ variable. All uncertainties are statistical.

4.7.3. Same-side Tagging Discriminating Variables

Same-side tagging is used to determine the flavor of the reconstructed B meson on the side that it is reconstructed. It is based on the expected pattern of the hadronization process producing a B meson from the initial b quark. It is assumed that the b quark picks up an u, d or s quark from the virtual $q\bar{q}$ pair, and the remaining quark in the pair forms an accompanying meson. In this pattern, a B meson produced as a B_d^0 ($\bar{b}d$) meson is likely

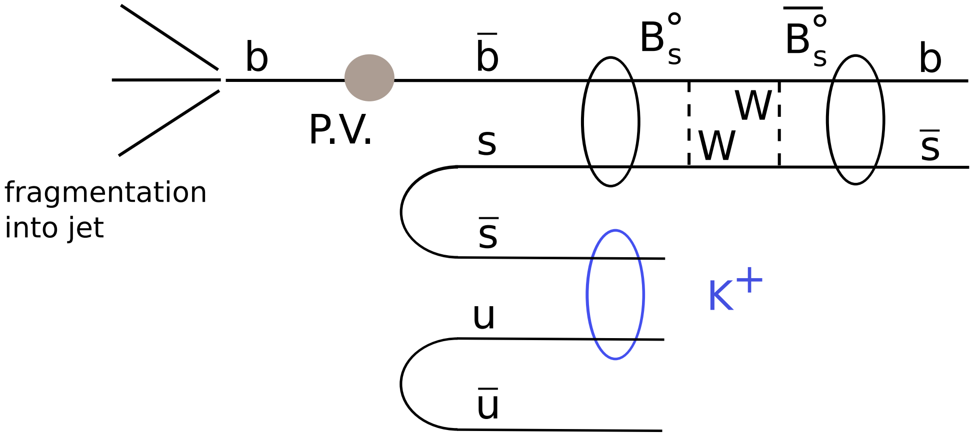

Figure 4.6. An illustration of the fragmentation product K^+ used in the same-side flavor tag to identify an initial B_s^0 meson.

to be associated with a nearby π^+ $(u\bar{d})$ meson, a B^+ $(\bar{b}u)$ meson with a π^- $(d\bar{u})$ meson, and a B_s^0 $(\bar{b}s)$ meson with a K^+ $(u\bar{s})$ meson, as illustrated in Fig.4.6. These correlations were first observed by the OPAL experiment in $e^+e^-\to Z^0\to b\bar{b}$ events [**38**].

The different methods to identify an accompanying particle can be classified into two groups: tagging using one track selected according to its kinematic properties, and tagging using some average quantity from all the tracks in the vicinity of the B meson. The best tagging method in each group is chosen, following the extensive studies with MC events. In the first group the accompanying particle is selected by requiring the minimal value of $\Delta R = \sqrt{\Delta\phi^2 + \Delta\eta^2}$, where $\Delta\phi$ $(\Delta\eta)$ is the difference of the azimuthal angle (pseudorapidity) of momentum direction between the given track and the B meson. Tracks not used in the B meson reconstruction, and with transverse momentum $p_T > 500$ MeV/c, are considered for this selection. The corresponding discriminating variable for the flavor tagging is defined as the product of the track charge and ΔR.

In the second group, the tagger is based on the p_T-weighted average charge of all tracks within a cone defined as $\cos(\Delta\phi) > 0.8$. This charge Q_{jet} is defined as:

$$Q_{\text{jet}} = \frac{\sum q \cdot (p_T)^{0.6}}{\sum (p_T)^{0.6}}. \tag{4.11}$$

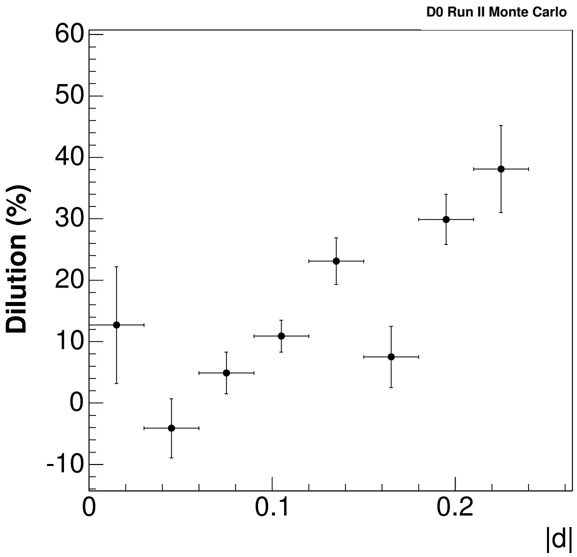

Figure 4.7. Dilution as a function of the variable $|d|$ for combined same-side tagger in the $B_s^0 \rightarrow J/\psi\phi$ MC events.

There is no cut on the p_T of track used in this definition. The decay products of the B meson are explicitly excluded from the sums.

The combination of these two discriminating variables is done by the likelihood ratio method described in Section 4.7.1. The PDF $f_i^b(x_i)$, $f_i^{\bar{b}}(x_i)$ and their ratio are obtained from the $B_s^0 \rightarrow \mu^+\nu D_s^- X$ MC events and the combined tagging variable is constructed using Eq. 4.3. The dilution of the same-side tagging as a function of the variable $|d|$, measured in the $B_s^0 \rightarrow J/\psi\phi$ MC events, is shown in Fig. 4.7. The performance of the same-side tagging is determined by computing the sum $\sum \varepsilon_i(\mathcal{D}_i)^2$ over the bins in the variable $|d|$. It is given in Table 4.4 separately for two discriminating variables and their combination. It can be seen that the combination of variables improves the tagging power.

The performance of the same-side tagging is verified using the $B^\pm \rightarrow J/\psi K^\pm$ events. Since the initial flavor of the B meson is determined by the charge of the kaon, the tagging performance in data can be measured and compared with the MC. This comparison is presented in Table 4.5 and in Figure 4.8, where the dilution of same-side tagging is given

tagger	ε (%)	$\mathcal{D}$ (%)	$\mathcal{P}$ (%)
Minimal ΔR	73.1 ± 1.5	14.1 ± 1.6	1.82 ± 0.36
Q_{jet}	84.3 ± 1.7	16.5 ± 2.2	1.05 ± 0.27
Same-side tagging	84.3 ± 1.7	13.0 ± 1.5	2.36 ± 0.40

Table 4.4. Performance of discriminating variables of same-side tagging and their combination. The dilution $\mathcal{D}$ is averaged over all values of $|d|$. The tagging power $\mathcal{P}$ is computed as the sum $\sum \varepsilon_i(\mathcal{D}_i)^2$ over the bins in the $|d|$. Uncertainties are due to the limited MC statistics.

$\|d\|$	$\mathcal{D}$(MC) (%)	$\mathcal{D}$(data) (%)
$0.00 < \|d\| < 0.10$	3.9 ± 1.1	4.9 ± 1.3
$0.10 < \|d\| < 0.20$	23.1 ± 0.9	24.2 ± 1.1
$0.20 < \|d\| < 0.35$	46.1 ± 2.3	50.5 ± 2.2

Table 4.5. Dilution of same-side tagging in MC and real $B^\pm \to J/\psi K^\pm$ events for different values of the variable $|d|$. All uncertainties are statistical.

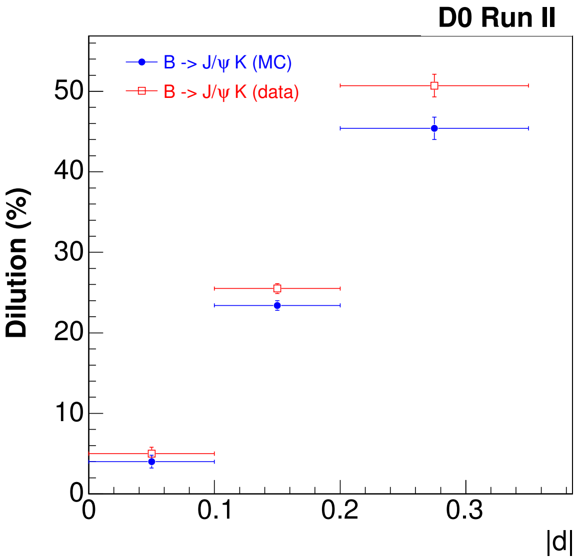

Figure 4.8. Dilution as a function of the variable $|d|$ for combined same-side tagger in $B^\pm \to J/\psi K^\pm$ events (data and Monte Carlo).

for different values of the variable $|d|$. A good agreement between data and MC indicates an adequate description of the hadronization processes by the MC.

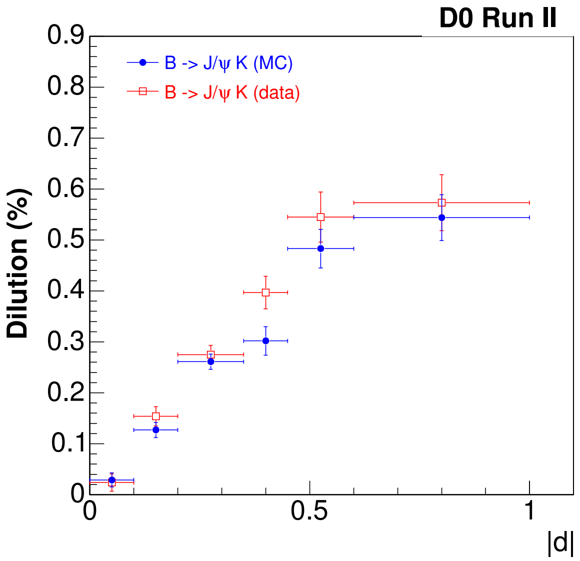

Figure 4.9. Dilution as a function of the variable $|d|$ for combined same-side and opposite-side tagger in $B^{\pm} \rightarrow J/\psi K^{\pm}$ events (data and Monte Carlo).

4.7.4. Combined Opposite-side and Same-side Tagging

The combination of the same-side and opposite-side tagging is performed using the likelihood ratio method. The efficiency of the opposite-side tagging, which is based on the identified muon, electron or secondary vertex, is about 20%, and if the opposite-side tagging for a given event is not available, we use the event charge tagger, defined in Section 4.7.2. The addition of the event charge in our tagging algorithm increases the overall performance. Table 4.6 and Figure 4.9 compare the dilution of the combined flavor tagging for MC and real $B^{\pm} \rightarrow J/\psi K^{\pm}$ events. It can be seen that the dilution for data and MC agree well, justifying the utilization of the dilution measured in the $B_s^0 \rightarrow J/\psi\phi$ MC events in the study of real data. The dilution measured for different $|d|$ values is given in Table 4.7 and in Figure 4.10. It can be seen that the combination of all available flavor taggers provides an enhanced tagging power $\mathcal{P} = 4.68 \pm 0.54$, to be compared with the opposite-side tagging power $\mathcal{P} = 2.48 \pm 0.21$ [**37**].

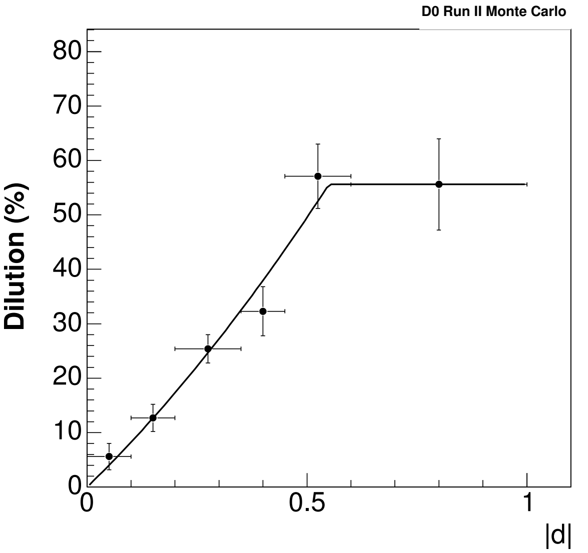

Figure 4.10. Dilution as a function of the variable $|d|$ for combined same-side and opposite-side tagger in $B_s^0 \to J/\psi\phi$ MC events.

$\lvert d\rvert$	$\mathcal{D}(B^\pm \to J/\psi K^\pm)$ (%) (MC)	$\mathcal{D}(B^\pm \to J/\psi K^\pm)$ (%) (data)
$0.00 < \lvert d\rvert < 0.10$	0.029 ± 0.014	0.024 ± 0.017
$0.10 < \lvert d\rvert < 0.20$	0.127 ± 0.015	0.154 ± 0.019
$0.20 < \lvert d\rvert < 0.35$	0.261 ± 0.015	0.275 ± 0.018
$0.35 < \lvert d\rvert < 0.45$	0.302 ± 0.028	0.397 ± 0.032
$0.45 < \lvert d\rvert < 0.60$	0.483 ± 0.038	0.545 ± 0.049
$0.60 < \lvert d\rvert < 1.00$	0.544 ± 0.045	0.573 ± 0.055

Table 4.6. Dilution of combined flavor tagging in MC and real $B^\pm \to J/\psi K^\pm$ events for different values of the variable $|d|$. All uncertainties are statistical.

The dependence of dilution on the variable $|d|$ in Figure 4.10 is parameterized by the following function:

$$|D| = 0.7895 \cdot |d| + 0.3390 \cdot d^2 \quad \text{if} \quad |d| < 0.55$$

$$|D| = 0.5957 \quad \text{if} \quad |d| > 0.55. \tag{4.12}$$

$\|d\|$	$\mathcal{D}$ (%)	$\mathcal{P}$ (%)
$0.00 < \|d\| < 0.10$	0.056 ± 0.024	0.10 ± 0.08
$0.10 < \|d\| < 0.20$	0.127 ± 0.025	0.45 ± 0.18
$0.20 < \|d\| < 0.35$	0.254 ± 0.026	1.60 ± 0.33
$0.35 < \|d\| < 0.45$	0.323 ± 0.045	0.83 ± 0.23
$0.45 < \|d\| < 0.60$	0.571 ± 0.059	1.15 ± 0.25
$0.60 < \|d\| < 1.00$	0.556 ± 0.084	0.55 ± 0.17
Total	-	4.68 ± 0.54

Table 4.7. Dilution and tagging power of combined flavor tagging in $B_s^0 \rightarrow J/\psi\phi$ MC events for different values of the variable $|d|$. All uncertainties are statistical.

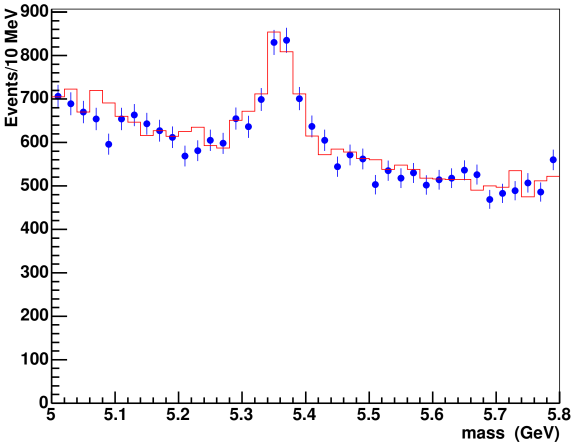

Figure 4.11. The mass of the B_s^0 candidates with $\mathcal{D} > 0$ (points) and $\mathcal{D} < 0$ (line).

There are 23817 (24051) candidates with $\mathcal{D} > 0$ ($\mathcal{D} < 0$). Figure 4.11 shows the mass distribution for events with positive and negative tags. Figure 4.12 shows the proper time distributions for events with positive and negative tags, for the signal and background region.

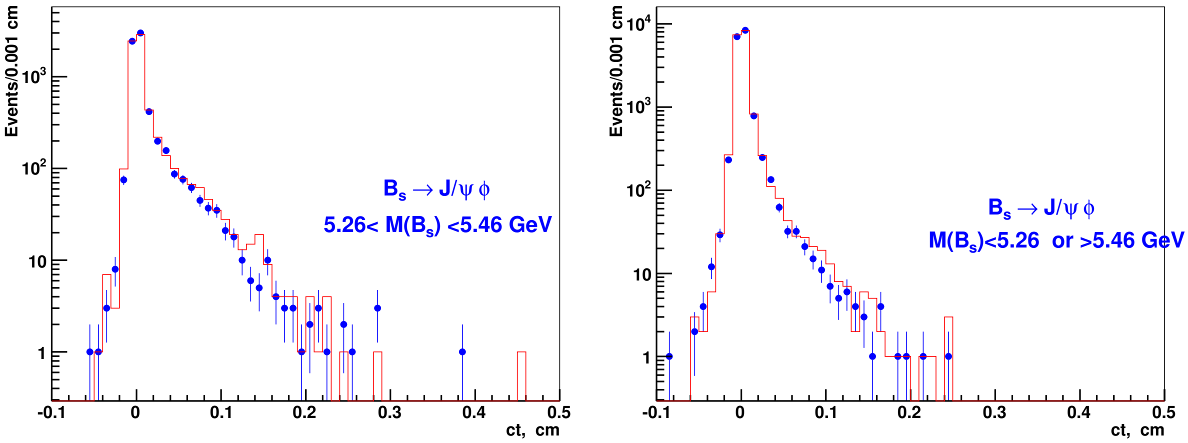

Figure 4.12. The proper decay length, ct, of the B_s^0 candidates with $\mathcal{D} > 0$ (points) and $\mathcal{D} < 0$ (line), for the signal region (left) and the background region (right).

4.8. Fit Variables and Probability Distribution Functions

A simultaneous unbinned maximum likelihood fit to the mass, proper decay length, and three decay angles is perform over the entire B_s^0 candidate sample. The likelihood function $\mathcal{L}$ is the product of probability distribution functions (PDFs) of all candidate events in the sample and is defined as:

$$\mathcal{L} \;=\; \prod_{i=1}^{N}[f_{sig}\mathcal{F}^i_{sig} + (1-f_{sig})\mathcal{F}^i_{bck}], \tag{4.13}$$

where $N = 48047$ is the total number of events and f_{sig} is the fraction of signal events. The function $\mathcal{F}^i_{sig}$ is the signal PDF and describes the distribution of the signal in mass, proper decay length, and the angular distributions. A Gaussian function with free mean and width is used to describe the signal mass distribution. The proper decay length distribution of the Light or Heavy component of the signal is parameterized by an exponential convoluted with a Gaussian function with the width taken from the event-by-event estimate of $\sigma(ct)$. $\mathcal{F}^i_{bck}$ is the background PDF and is a product of the background mass, proper decay length, and angular distributions.

4.8.1. Input Variables

- B_s^0 **Mass:** The B_s^0 mass is calculated from the J/ψ and ϕ vertex, as described in Section 4.6. In the B_s^0 invariant mass distribution shown in Fig 4.3 (top), the B_s^0 signal rises above a linear background.
- **Proper Decay Length and its Error:** The signed decay length of a B_s^0 meson is defined as the vector pointing from the primary vertex to the decay vertex projected onto the B_s^0 momentum in the transverse plane, as shown in Fig. 4.2. It is defined as:

$$L^B_{xy} = (\vec{x}_B - \vec{x}_{prim}) \cdot \vec{p}_T/p_T, \tag{4.14}$$

where $\vec{p}_T$ is the measured transverse momentum vector and p_T is its magnitude. The proper decay length, ct, is defined as:

$$ct = L_{xy}^B \cdot M_{B_s^0}/p_T, \tag{4.15}$$

where $M_{B_s^0} = 5.3675$ GeV/c^2 is the PDG value of the B_s^0 meson [**36**]. The proper decay length distribution distinquishes long lived particles from the prompt background, as shown in Fig. 4.4 (top). Along with the mass, the proper decay length variable can be used to identify signal events from the full B_s^0 candidate sample.

The B_s^0 proper decay length uncertainty ($\sigma(ct)$) distribution is shown in Fig. 4.4 (bottom). It peaks around 25 μm and has a long tail. Events with the proper decay length uncertainty below 60 μm are selected.

- **Decay Angle Distributions:** The decay angle distribution variables are used to separate the CP-even and CP-odd components in the B_s^0 signal sample. The time evolution of the angular distribution of the products of the decay of flavor tagged B_s^0 mesons, expressed in terms of the linear polarization amplitudes A_x and their relative phases δ_i is [**18**]:

$$\begin{aligned}
&\frac{d^3\Gamma\left[B_s^0(t) \to J/\psi(\to \mu^+\mu^-)\phi(\to K^+K^-)\right]}{d\cos\theta \quad d\varphi \quad d\cos\psi} \propto \\
&\quad 2\cos^2\psi(1-\sin^2\theta\cos^2\varphi) \qquad |A_0(t)|^2 \\
&+ \sin^2\psi(1-\sin^2\theta\sin^2\varphi) \qquad |A_\parallel(t)|^2 \\
&+ \sin^2\psi\sin^2\theta \qquad |A_\perp(t)|^2 \\
&+ \frac{1}{\sqrt{2}}\sin 2\psi\sin^2\theta\sin 2\varphi \quad Re(A_0^*(t)A_\parallel(t)) \\
&+ \frac{1}{\sqrt{2}}\sin 2\psi\sin 2\theta\cos\varphi \quad Im(A_0^*(t)A_\perp(t)) \\
&- \sin^2\psi\sin 2\theta\sin\varphi \qquad Im(A_\parallel^*(t)A_\perp(t)).
\end{aligned} \tag{4.16}$$

Polarization amplitudes for B_s^0 (upper sign) and $\bar{B}_s^0$ (lower sign) are given by the following equations:

$$\begin{aligned}
|A_0(t)|^2 &= |A_0(0)|^2 \left[\mathcal{T}_+ \ \pm \ e^{-\bar{\Gamma}t} \sin\phi_s \ \sin(\Delta m_s t)\right], \\
|A_\parallel(t)|^2 &= |A_\parallel(0)|^2 \left[\mathcal{T}_+ \ \pm \ e^{-\bar{\Gamma}t} \sin\phi_s \ \sin(\Delta m_s t)\right], \\
|A_\perp(t)|^2 &= |A_\perp(0)|^2 \left[\mathcal{T}_- \ \mp \ e^{-\bar{\Gamma}t} \sin\phi_s \ \sin(\Delta m_s t)\right],
\end{aligned}$$

$$Re(A_0^*(t)A_\parallel(t)) = |A_0(0)||A_\parallel(0)| \cos(\delta_2 - \delta_1) \left[\mathcal{T}_+ \ \pm \ e^{-\bar{\Gamma}t} \sin\phi_s \ \sin(\Delta m_s t)\right],$$

$$\begin{aligned}
Im(A_0^*(t)A_\perp(t)) \quad = \quad & |A_0(0)||A_\perp(0)| \Big[\ e^{-\bar{\Gamma}t} \left(\ \pm\sin\delta_2 \cos(\Delta m_s t) \ \mp\cos\delta_2 \sin(\Delta m_s t) \cos\phi_s \right) \\
& -\frac{1}{2}\left(e^{-\Gamma_H t} - e^{-\Gamma_L t}\right) \sin\phi_s \ \cos\delta_2 \Big],
\end{aligned}$$

$$\begin{aligned}
Im(A_\parallel^*(t)A_\perp(t)) \quad = \quad & |A_\parallel(0)||A_\perp(0)| \Big[\ e^{-\bar{\Gamma}t} \left(\ \pm\sin\delta_1 \cos(\Delta m_s t) \ \mp\cos\delta_1 \sin(\Delta m_s t) \cos\phi_s \right) \\
& -\frac{1}{2}\left(e^{-\Gamma_H t} - e^{-\Gamma_L t}\right) \sin\phi_s \ \cos\delta_1 \Big],
\end{aligned}$$

where,

$$\mathcal{T}_\pm = \frac{1}{2}\left\{(1 \pm \cos\phi_s)e^{-\Gamma_L t} + (1 \mp \cos\phi_s)e^{-\Gamma_H t}\right\}.$$

The two strong phase parameters, δ_1 and δ_2, are related to the phases of the polarization amplitudes as follows:

$$\begin{aligned}
\delta_1 &= -\delta_\parallel + \delta_\perp, \\
\delta_2 &= -\delta_0 + \delta_\perp.
\end{aligned}$$

4.8.2. Probability Distribution Functions (PDFs)

Signal Parameterization

The signal PDF is a product of the signal mass PDF, and a function describing the sum of the time evolution of the angular distributions of the CP-even and odd states.

- **Signal Mass PDF:** The B_s^0 mass signal peak is Gaussian in shape. The signal mass PDF is described by a single Gaussian function as:

  $$G(m_k \,|M, \sigma) = \frac{1}{\sigma\sqrt{2\pi}} exp\left(\frac{-(m_k - M)^2}{2\sigma^2}\right), \tag{4.17}$$

  where m_k is the mass of the k^{th} event, and M and σ are two free parameters for the mean and width of the B_s^0 signal, respectively.
- **Signal Proper Decay Length and Decay Angle Distributions PDF:** The proper decay length and decay angle distribution of the signal are determined by the time-dependent three-angle distribution for the decay of flavor tagged B_s^0 mesons expressed in terms of the linear polarization amplitudes $|A_x(t)|$ and their relative phases δ_i. The normalized probability distribution functions for B_s^0 and $\bar{B}_s^0$ take the general form:

  $$P_A(\theta, \phi, \psi, t) = \frac{1}{N} P(\theta, \phi, \psi, t),$$
  $$\bar{P}_A(\theta, \phi, \psi, t) = \frac{1}{N} \bar{P}(\theta, \phi, \psi, t).$$

  The detector acceptance can have an effect on these distributions, leading to modified forms of the probability distribution functions. The full distributions including detector acceptances for the three angles zre provided in Appendix C.

Background Parameterization

Independent parameters are allowed for the prompt and non-prompt background components in mass, lifetime, and anglular distributions.

- **Background Mass PDF:** A linear function is used to describe the prompt background in the mass distribution. It is defined as:

  $$P_M(M_k|a_{1p}) = 1 + a_{1p}M_k, \tag{4.18}$$

  where M_k is the mass of the k^{th} event.

  A second order polynomial is used to describe the non-prompt background, defined as:

  $$P_M(M_k|a_{1l}, a_{2l}) = 1 + a_{1l}M_k + a_{2l}M_k^2. \tag{4.19}$$

  Three free parameters are used: a_{1p} for the prompt background and a_{1l} and a_{2l} for the non-prompt background.

- **Background Proper Decay Length PDF:** The prompt component of the proper decay length background is simulated as a Gaussian function centered at zero, with the width taken from the event-by-event estimate of uncertainty in proper decay length, scaled by a factor S to account for the mis-measurement of the resolution. The non-prompt component is simulated as a superposition of one exponential for the negative decay length region ($ct < 0$), mainly due to events with mis-reconstructed B vertices, and two exponentials for the positive ct region. The slopes and normalization factors of the three exponentials are free. The six free parameters are: b_-, b_+, b_{++}, f_-, f_+, and f_{++}. The background proper decay length PDF (τ_{bkg}) is given by:

  $$\begin{aligned} &\tau_{bkg}(ct_k, \sigma(ct_k) \mid f_-, f_+, f_{++}, b_-, b_+, b_{++}, S) \\ &= (1 - f_- - f_+ - f_{++})G(ct_k, \sigma(ct_k) \,|0, S) \\ + \; f_- \; e^{(-ct_k \;|\; b_-)} \; &+ \; f_+ \; e^{(ct_k \;|\; b_+)} \; + \; f_{++} \; e^{(ct_k \;|\; b_{++})}, \end{aligned} \tag{4.20}$$

where,

$$G(ct_k, \sigma(ct_k) \mid \mu, S) = \frac{e^{\frac{1}{2}a^2}}{\sqrt{2}\ \sigma(ct_k)\ \left(\ Freq(b) - Freq(c)\ \right)}, \tag{4.21}$$

and

$$e^{(ct_k \ \mid \ \tau)} = \frac{e^{\left(-\frac{ct_k}{\tau}\right)}}{\tau\left(1 - e^{-\frac{R}{\tau}}\right)}. \tag{4.22}$$

Here, ct_k and $\sigma(ct_k)$ are the proper decay length and its uncertainty for the k^{th} event, μ is the mean value, and R is the maximum/minimum value of the range (from zero) in the exponential fit. In addition, $a = (ct_k - \mu)/(\sigma(ct_k)S)$, $b = (-1 - \mu)/(\sigma(ct_k)S)$, $\quad c = (1 - \mu)/(\sigma(ct_k)S)$, $\quad$ and the normal frequency function ($Freq(p)$) is defined as:

$$Freq(p) = \frac{1}{\sqrt{2\pi}} \int_{-\infty}^{p} e^{-\frac{t^2}{2}} dt. \tag{4.23}$$

- **Background Decay Angle PDF:**
  - **cosθ:** A fourth order polynomial is used to describe the $cos\theta$ angular distribution of the background:

    $$P_T(X_k|X_{2p}, X_{4p}) = \frac{1 + X_{2p}X_k^2 + X_{4p}X_k^4}{2\left(1 + \frac{X_{2p}}{3} + \frac{X_{4p}}{5}\right)}, \tag{4.24}$$

    where X_k is $cos\theta$ of the k^{th} event and X_{2p} and X_{4p} are free parameters. Separate parameters are allowed for the prompt and non-prompt background. The four free parameters are then: X_{2p}, X_{4p} for the prompt background and X_{2l}, X_{4l} for the non-prompt background.
  - **cos(2ϕ):** A second order polynomial is used to describe the $cos(2\phi)$ angular distribution of the background:

    $$P_T(Y_k|Y_{1p}, Y_{2p}) = \frac{1 + Y_{1p}Y_k + Y_{2p}Y_k^2}{2\pi\left(1 + \frac{Y_{2p}}{2}\right)}, \tag{4.25}$$

where Y_k is $cos(2\phi)$ of the k^{th} event and Y_{1p} and Y_{2p} are free parameters. Separate parameters are allowed for the prompt and non-prompt background. The four free parameters are then: Y_{1p}, Y_{2p} for the prompt background and Y_{1l}, Y_{2l} for the non-prompt background.

- **cos**$^2\psi$**:** A second order polynomial is used to describe the $cos^2\psi$ angular distribution of the background:

$$P_T(Z_k|Z_{2p}) = \frac{1 + Z_{2p}Z_k^2}{2 + \frac{2Z_{2p}}{3}}, \tag{4.26}$$

where Z_k is $cos^2\psi$ of the k^{th} event and Z_{2p} is a free parameters. Separate parameters are allowed for the prompt and non-prompt background. The two free parameters are then: Z_{2p} for the prompt background and Z_{2l} for the non-prompt background.

- **Background of Interfering CP-even waves:** Background terms analogous to the interference term of the CP-even waves are described with one free coefficient. Two free parameters are used: Int_p for the prompt background and Int_l for the non-prompt background.

4.8.3. Fit Parameters

In total, there are 32 free parameters in the maximum likelihood function. They are listed and summarized in Table 4.8.

Index	Parameter notation	description
1	$f_{sig}(N_{sig})$	The fraction of the signal in the total number of candidate events, defined in Eq. 4.13.
2	M	The mean value of the Gaussian function in the signal mass PDF.
3	σ	The width of the Gaussian function in the signal mass PDF.
4	$\overline{\tau}$	The inverse of the average decay width: $\bar{\tau} = 1/\bar{\Gamma}$, where $\bar{\Gamma} = (\Gamma_L + \Gamma_H)/2$.
5	$\Delta\Gamma$	Decay width difference between two CP eigenstates in the B_s^0–$\bar{B}_s^0$ system: $\Delta\Gamma = \Gamma_L - \Gamma_H$.
6	$A_\perp(0)$	The magnitude of the CP-odd linear polarization amplitude at time $t = 0$ in $B_s^0 \to J/\psi\phi$ decay.
7	$\|A_0(0)\|^2 - \|A_\parallel(0)\|^2$	The difference in square of CP-even linear polarization amplitudes at time $t = 0$ in $B_s^0 \to J/\psi\phi$ decay.
8	δ_1	$\delta_1 \equiv Arg(A_\parallel(0)^* A_\perp(0))$, CP conserving strong phase, expected to be mod π.
9	δ_2	$\delta_2 \equiv Arg(A_0(0)^* A_\perp(0))$, CP conserving strong phase, expected to be 0.
10	ϕ_s	CP-violating weak phase. It can be expressed in terms of elements of the CKM matrix as $e^{i\phi_s} = \frac{V_{ts}V_{tb}^*}{V_{ts}^*V_{tb}}\frac{V_{cs}^*V_{cb}}{V_{cs}V_{cb}^*}$, expected to be very small $\mathcal{O}(0.03)$.
11	S	A scale factor parameter multiplied to the proper decay length uncertainty $\sigma(ct)$ if it is under/over estimated.
12	a_{1p}	The coefficient of the mass term in the linear parameterization, describing the mass distribution of the prompt background.
13	a_{1l}	The coefficient of the m term in the polynomial $1 + a_{1l}m + a_{2l}m^2$, describing the mass distribution of the non-prompt background.
14	a_{2l}	The coefficient of the m^2 term in the polynomial $1 + a_{1l}m + a_{2l}m^2$, describing the mass distribution of the non-prompt background.

Index	Parameter notation	description
15	f_-	The normalization constant of the exponential for $ct < 0$ in the background lifetime PDF.
16	f_+	The normalization constant of the first exponential for $ct > 0$ in the background lifetime PDF.
17	f_{++}	The normalization constant of the second exponential for $ct > 0$ in the background lifetime PDF.
18	b_-	The slope of the exponential function for $ct < 0$ in the background lifetime PDF.
19	b_+	The slope of the first exponential function for $ct > 0$ in the background lifetime PDF.
20	b_{++}	The slope of the exponential function for $ct > 0$ in the background lifetime PDF.
21	X_{2p}	Coefficient of the $cos^2\theta$ term in the polynomial $1 + X_{2p}cos^2\theta + X_{4p}cos^4\theta$, describing the transversity polar angle distribution of the prompt background.
22	X_{4p}	Coefficient of the $cos^4\theta$ term in the polynomial $1 + X_{2p}cos^2\theta + X_{4p}cos^4\theta$, describing the transversity polar angle distribution of the prompt background.
23	X_{2l}	Coefficient of the $cos^2\theta$ term in the polynomial $1 + X_{2l}cos^2\theta + X_{4l}cos^4\theta$, describing the transversity polar angle distribution of the non-prompt background.
24	X_{4l}	Coefficient of the $cos^4\theta$ term in the polynomial $1 + X_{2l}cos^2\theta + X_{4l}cos^4\theta$, describing the transversity polar angle distribution of the non-prompt background.
25	Y_{1p}	Coefficient of the $cos(2\phi)$ term in the polynomial $1 + Y_{1p}cos(2\phi) + Y_{2p}cos^2(2\phi)$, describing the ϕ-angle distribution of the prompt background.
26	Y_{2p}	Coefficient of the $cos^2(2\phi)$ term in the polynomial $1 + Y_{1p}cos(2\phi) + Y_{2p}cos^2(2\phi)$, describing the ϕ-angle distribution of the prompt background.
27	Y_{1l}	Coefficient of the $cos(2\phi)$ term in the polynomial $1 + Y_{1l}cos(2\phi) + Y_{2l}cos^2(2\phi)$, describing the ϕ-angle distribution of the non-prompt background.
28	Y_{2l}	Coefficient of the $cos^2(2\phi)$ term in the polynomial $1 + Y_{1l}cos(2\phi) + Y_{2l}cos^2(2\phi)$, describing the ϕ-angle distribution of the non-prompt background.
29	Z_{2p}	Coefficient of the $cos^2\psi$ term in the polynomial $1 + Z_{2p}cos^2\phi$, describing the ψ-angle distribution of the prompt background.
30	Z_{2l}	Coefficient of the $cos^2\psi$ term in the polynomial $1 + Z_{2l}cos^2\psi$, describing the ψ-angle distribution of the non-prompt background.
31	Int_p	Allowing for a term analogous to line 4 of Eq.4.16 for the prompt background.
32	Int_l	Allowing for a term analogous to line 4 of Eq.4.16 for the non-prompt background.

Table 4.8. Summary of the 32 free fit parameters used in the unbinned maximum likelihood fit.

4.9. Fitting Procedure and Fit Results

The likelihood function, $\mathcal{L}$, described above is maximized to obtain the most likely values of the free parameters. This maximization is done in the ROOT [**39**] framework, using the MINUIT [**40**] program.

For a given event, the B_s^0 ($\bar{B}_s^0$) rates are multiplied by a factor $p^{B_s^0}$ and $(1 - p^{B_s^0})$, respectively, where $p^{B_s^0}$ is the probability of having a pure state B_s^0 at time zero, related to the dilution $\mathcal{D}$ of Eq. (4.12) by $p^{Bs} = (1 - \mathcal{D})/2$.

There is a high degree of correlation between Δm_s, ϕ_s, and the two CP conserving strong phases δ_1 and δ_2, making it difficult to obtain stable fits when each of parameters are allowed to vary freely. In this study, Δm_s is fixed to the value of 17.77 ± 0.12 ps^{-1}, as measured by the CDF Collaboration in Ref. [**41**].

In addition, the phases analogous to δ_1 and δ_2 have been measured for the decay $B_d^0 \rightarrow J/\psi K^*$ at the B factories. In this study, the phases δ_1 and δ_2 are allowed to vary under a Gaussian constraint around the the world-average values [**42**] for the $B_d^0 \rightarrow J/\psi K^*$ decay, where $\delta_1 = -0.46$ and $\delta_2 = 2.92$. The width of the Gaussian is chosen to be $\pi/5$, which allows for some degree of violation of the symmetry relating the two decay processes, yet constrains the signs of $\cos\delta_1$ and $\cos\delta_2$ to agree with those of Ref. [**42**]. The solution with $\cos\delta_1 < 0$ is disfavored on theoretical [**43**] and experimental [**44**] grounds.

The likelihood fit results for three different cases are presented in Table 4.9. In the first case, ϕ_s is allowed to be free. In the second case ϕ_s is set equal to the SM value, and in the third case $\Delta\Gamma_s$ is constrained by the relation $\Delta\Gamma_s^{SM} \cdot |\cos(\phi_s)|$.

4.9.1. Case 1: Free ϕ_s

In the case of a free ϕ_s, the fit yields two likelihood maxima, one with $\phi_s = -0.57^{+0.24}_{-0.30}$ rad and $\Delta\Gamma_s = 0.19 \pm 0.07$ ps^{-1}, and the other with $\phi_s = 2.92^{+0.30}_{-0.24}$ and $\Delta\Gamma_s = -0.19 \pm 0.07$ ps^{-1}. This is shown in the likelihood profile scan as a function of ϕ_s in Fig. 4.13. The errors are statistical and were obtained from the likelihood scan.

	free ϕ_s	$\phi_s \equiv \phi_s^{SM}$	$\Delta\Gamma_s^{th}$
$\bar{\tau}_s$ (ps)	1.52±0.06	1.53±0.06	1.49±0.05
$\Delta\Gamma_s$ (ps^{-1})	0.19±0.07	0.14±0.07	0.083 ± 0.018
$A_\perp(0)$	0.41±0.04	0.44±0.04	0.45±0.03
$\lvert A_0(0)\rvert^2 - \lvert A_{\lvert\lvert}(0)\rvert^2$	0.34±0.05	0.35±0.04	0.33±0.04
δ_1	−0.52±0.42	−0.48±0.45	−0.47±0.42
δ_2	3.17±0.39	3.19±0.43	3.21±0.40
ϕ_s	$-0.57^{+0.24}_{-0.30}$	$\equiv -0.04$	-0.46 ± 0.28
ΔM_s (ps^{-1})	$\equiv$ 17.77	$\equiv$ 17.77	$\equiv$ 17.77

Table 4.9. Summary of the likelihood fit results for the three cases: Free ϕ_s, ϕ_s constrained to the SM value, and $\Delta\Gamma_s$ constrained by the relation $\Delta\Gamma_s^{SM} \cdot |\cos(\phi_s)|$.

1	f_{sig} (N_{sig})	0.0409±0.0013 (1967±65)
2, 3	M , σ (in MeV/c^2)	5361.4±1.0 , 30.1±1.0
4	$\bar{\tau}$ (in μm)	456±17
5	$\Delta\Gamma$ (in ps^{-1})	0.19±0.07
6, 7	$A_\perp(0)$, $\lvert A_0(0)\rvert^2 - \lvert A_{\lvert\lvert}(0)\rvert^2$	0.41±0.04 , 0.34±0.05
8, 9	δ_1 , δ_2	-0.52±0.42 , 3.17±0.39
10	ϕ_s	$-0.57^{+0.24}_{-0.30}$
11	ΔM_s (in ps^{-1})	$\equiv$ 17.77
12	S	1.24±0.01
13, 14, 15	a_{1p} , a_{1l} , a_{2l}	-0.06±0.03 , -1.45±0.08 , 0.68±0.11
16, 17, 18	f_- , f_+ , f_{++}	0.049±0.004 , 0.155±0.004 , 0.035±0.003
19, 20, 21	b_- , b_+ , b_{++} (in μm)	65±3 , 88±3 , 399±21
22, 23	X_{2p} , X_{4p}	0.85±0.09 , -0.60±0.09
24, 25	X_{2l} , X_{4l}	0.39±0.17 , -0.23±0.19
26, 27	Y_{1p} , Y_{2p}	-0.23±0.01 , -0.10±0.02
28, 29	Y_{1l} , Y_{2l}	-0.15±0.02 , -0.00±0.04
30, 31	Z_{2p} , Z_{2l}	0.05±0.02 , 0.27±0.06
31, 32	Int_p , Int_l	-0.011±0.003 , -0.018±0.001

Table 4.10. Summary of the fit results for all free parameters (case 1).

As a result of the constraints imposed on the phases δ_1 and δ_2, the second maximum with $\phi_s = 2.92^{+0.30}_{-0.24}$ and $\Delta\Gamma_s = -0.19\pm0.07$ ps^{-1} is disfavored by a likelihood ratio of 1:29.

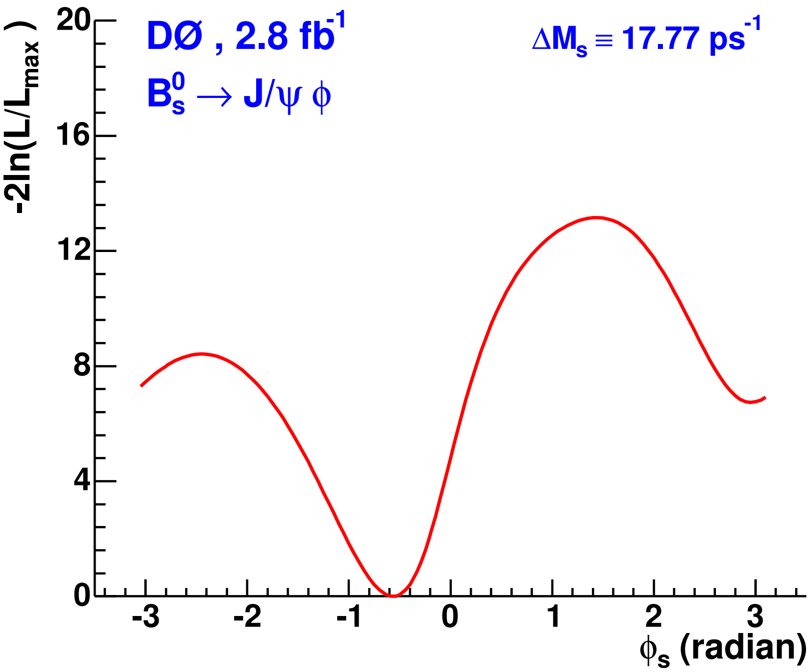

Figure 4.13. The likelihood scan as a function of ϕ_s.

Without the constraints on the phases, ϕ_s shifts by only 0.02 for the $\Delta\Gamma_s > 0$ solution. Results for all 32 parameters of this fit are presented in Table 4.10.

The likelihood scan as a function of $\Delta\Gamma_s$ is also performed, with the results shown in Fig. 4.14. Fig. 4.15 shows the 1-σ, 2-σ, and 3-σ standard deviation contours in the ($\Delta\Gamma_s$, ϕ_s) plane. It demonstrates the range of uncertainty for these correlated parameters. The correlation matrix for the physics parameters is given in Table 4.11.

A study of an ensemble test using 2000 pseudo-data events with similar statistical sensitivity was performed. The events were generated with the same parameters as shown in the first column of Table 4.11. Figures 4.16 - 4.18 show the distributions of the fitted values of $\bar{\tau}_s$, $|A_0(0)|^2 - |A_{||}(0)|^2$, $A_\perp(0)$, ϕ_s and $\Delta\Gamma_s$. As seen in these figures, there is no significant bias. Figures 4.19 - 4.23 show the distributions of the errors, and the distributions of pulls for the subset of experiments where the fitted error is close to the value obtained at DØ. The arrows at $\phi_s = -1.20$ and $\phi_s = 0.06$ in Fig. 4.18 indicate the

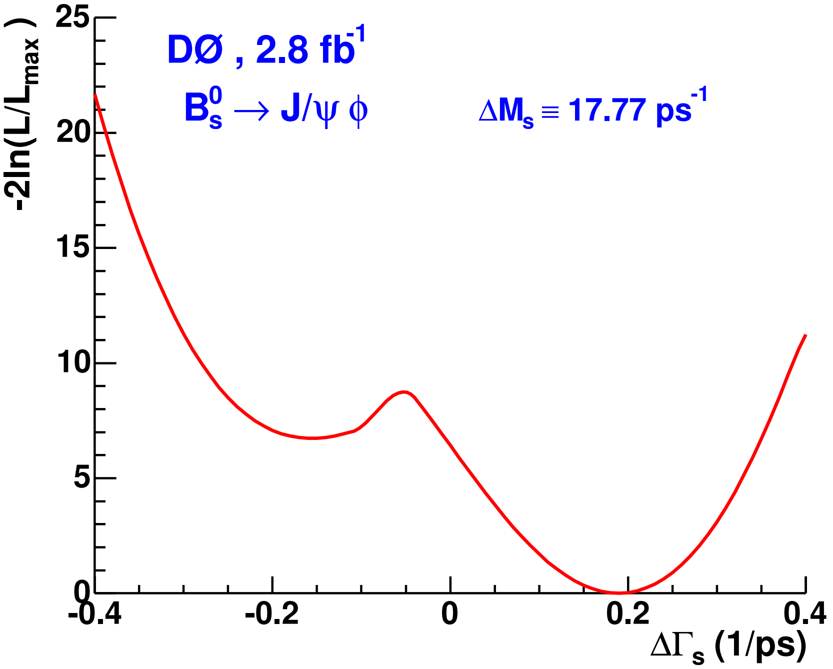

Figure 4.14. The likelihood scan as a function of $\Delta\Gamma_s$.

	δ_1	δ_2	$\bar{\tau}_s$	$A_\perp(0)$	$\Delta\Gamma_s$	ϕ_s
$\lvert A_0(0)\rvert^2 - \lvert A_{\|\|}(0)\rvert^2$	0.111	-0.053	-0.052	0.289	0.002	0.055
δ_1		0.813	-0.019	0.170	-0.131	0.072
δ_2			0.033	-0.019	-0.083	0.055
$\bar{\tau}_s$				-0.453	0.230	0.571
$A_\perp(0)$					-0.624	-0.285
$\Delta\Gamma_s$						0.042

Table 4.11. Correlation coefficients for physics parameters.

allowed interval in ϕ_s at the 90% confidence level. The arrows at $\Delta\Gamma_s = 0.06$ ps^{-1} and $\Delta\Gamma_s = 0.30$ ps^{-1} indicate the allowed 90% CL interval for $\Delta\Gamma_s$. The scatter plot of $\Delta\Gamma_s$ as a function of ϕ_s is shown in Figure 4.24.

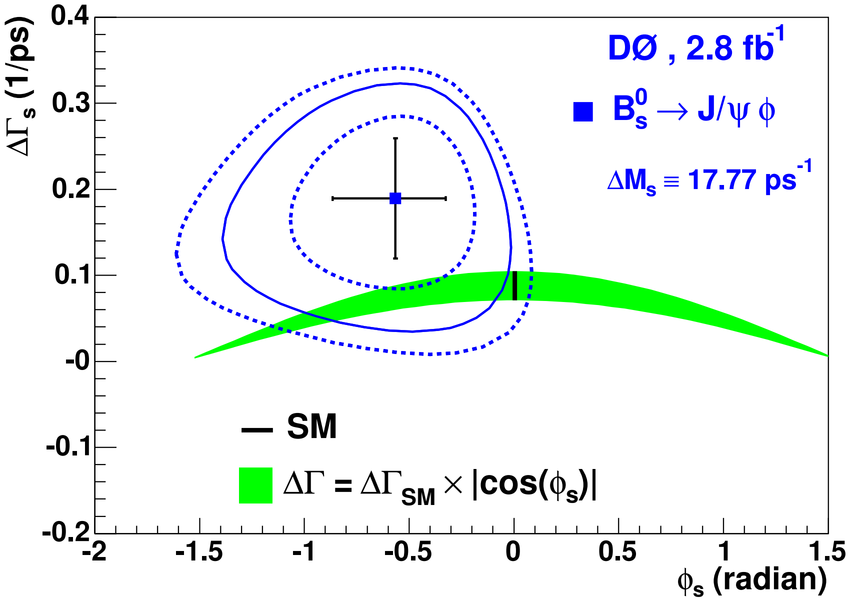

Figure 4.15. The 1-σ, 2-σ, and 3-σ 2D contours in the plane ($\Delta\Gamma_s$, ϕ_s) for the fit to the $B_s^0 \to J/\psi\phi$ (lines), the best fit (square), and 1D 1-σ uncertainties (cross). Also shown is the SM prediction, $\phi_s = -0.04$, $\Delta\Gamma_s = 0.088 \pm 0.017$ ps^{-1} [**45**].

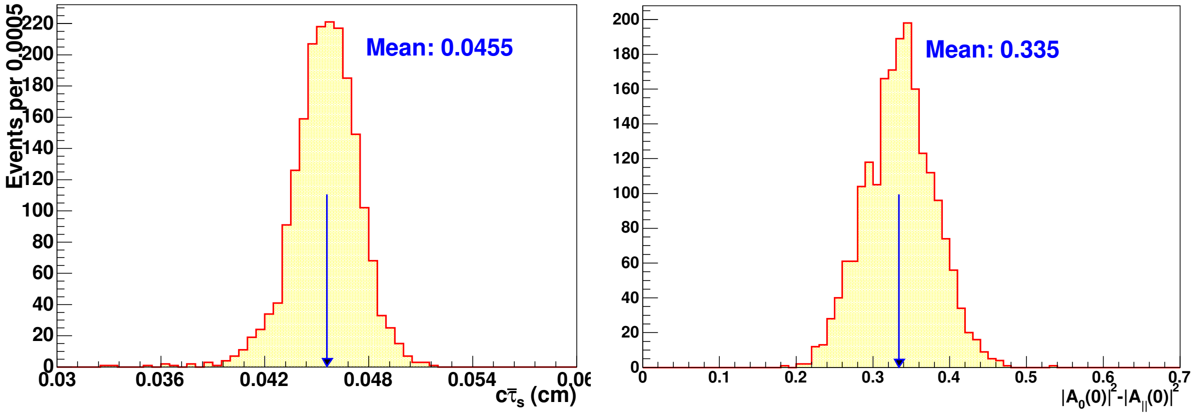

Figure 4.16. The distribution of $c\tau$ (left) and $|A_0(0)|^2 - |A_{||}(0)|^2$ (right) returned by fits to pseudo-experiments. The arrows indicate the input values.

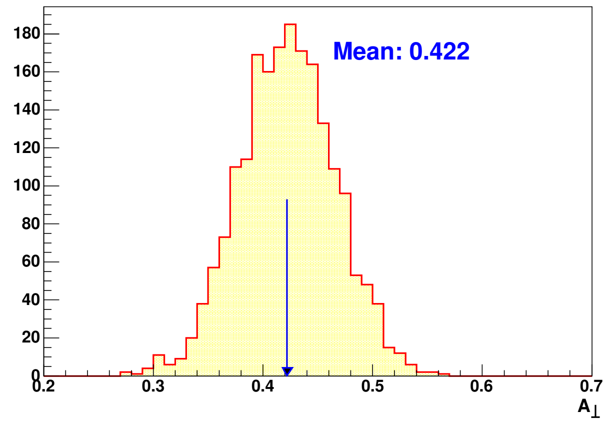

Figure 4.17. The distribution of $A_\perp(0)$ returned by fits to pseudo-experiments.

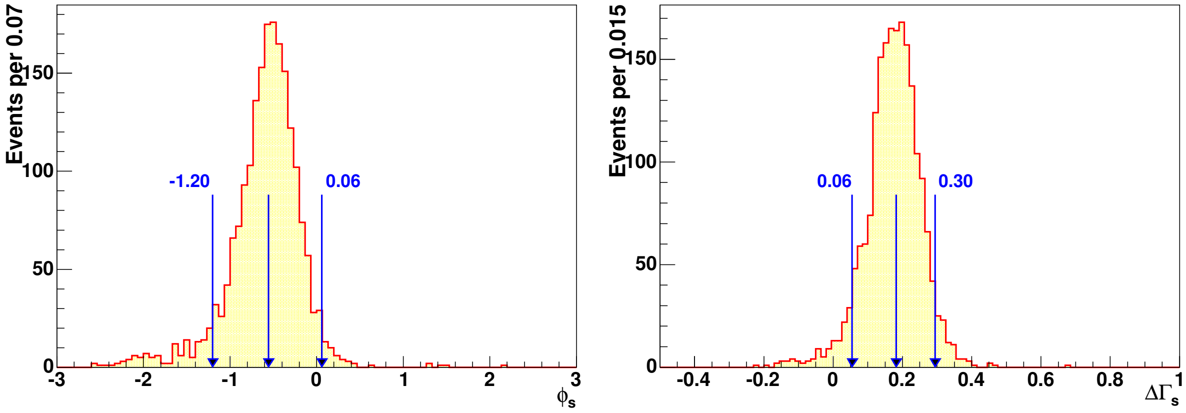

Figure 4.18. The distribution of ϕ_s (left) and $\Delta\Gamma_s$ (right) returned by fits to pseudo-experiments. The left and right arrows shown in each figure indicate the 90% exclusion region.

4.9.2. Case 2: $\phi_s \equiv \phi_s^{SM} \equiv -0.04$

In the second case, Pseudo-experiments with ϕ_s set to the SM value ($\phi_s^{SM} \equiv -0.04$) are studied to quantify the agreement with the SM prediction. The distribution of the fitted values of ϕ_s and the scatter plot of $\Delta\Gamma_s$ as a function of ϕ_s are shown in Fig. 4.25. From this it is observed there is a 6.6% probability to find the fitted value of ϕ_s equal to or lower

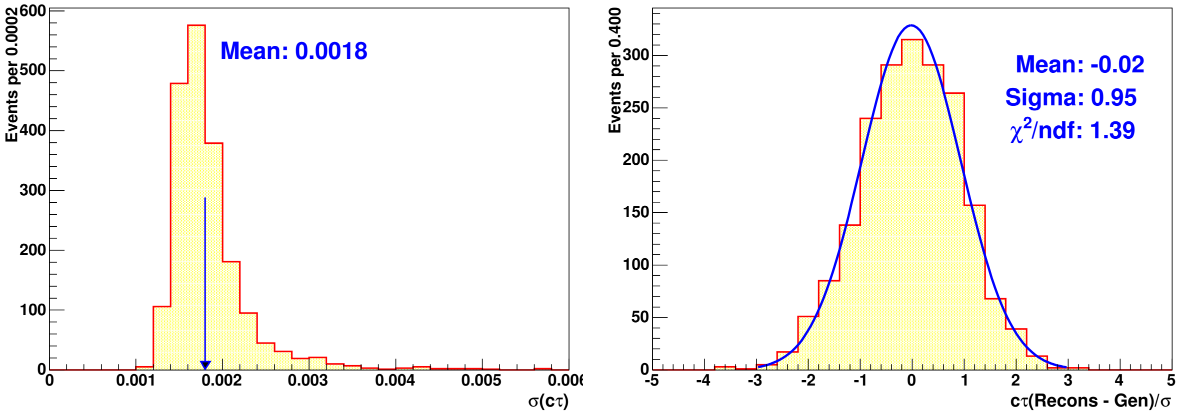

Figure 4.19. The distribution of error (left) and pull (right) for $c\tau$ returned by fits to pseudo-experiments.

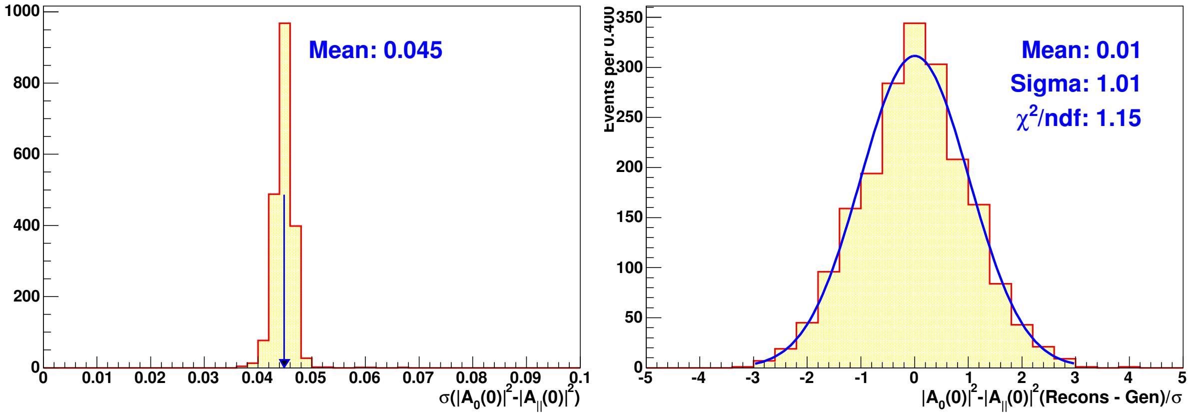

Figure 4.20. The distribution of error (left) and pull (right) for $|A_0(0)|^2 - |A_{||}(0)|^2$ returned by fits to pseudo-experiments.

than -0.57. From an ensemble generated with $\phi_s = \Delta\Gamma_s = 0$, there is a 2% probability to find the fitted value of $\Delta\Gamma_s = 0.19$ ps^{-1} or higher, as shown in Fig. 4.26.

Setting $\phi_s = -0.04$, as predicted by the SM, the value $\Delta\Gamma_s = 0.14 \pm 0.07$ ps^{-1} is obtained, which is consistent with the theoretical prediction of 0.088 ± 0.017 ps^{-1} [**45**]. The results for this fit are shown in the second column in Table 4.9.

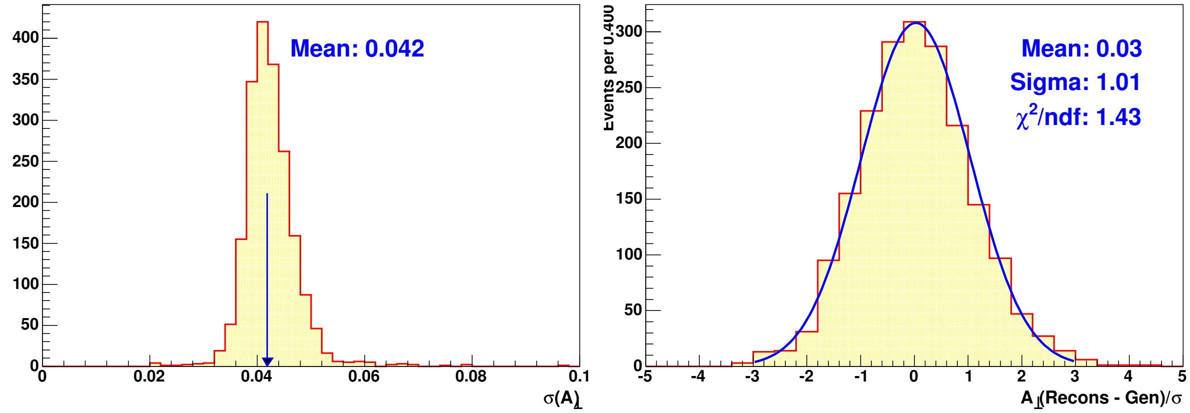

Figure 4.21. The distribution of error (left) and pull (right) for $A_\perp(0)$ returned by fits to pseudo-experiments.

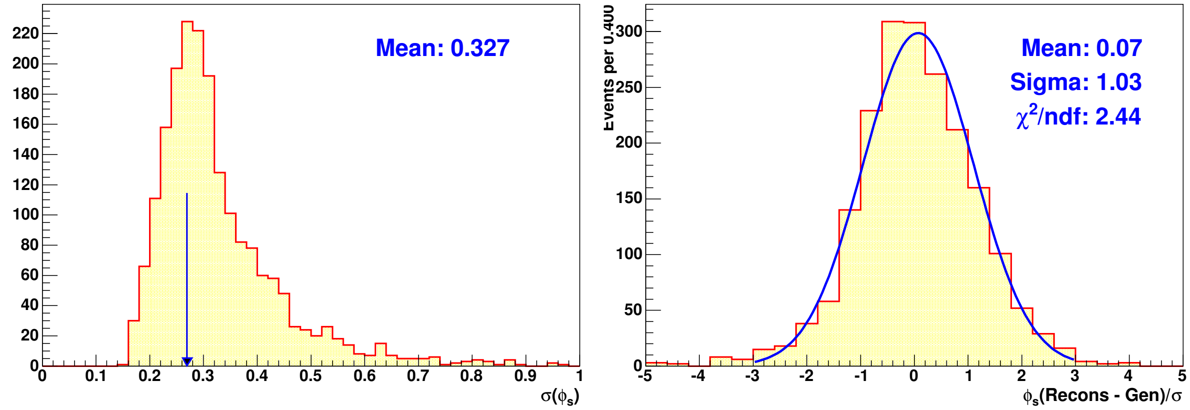

Figure 4.22. The distribution of error (left) and pull (right) for ϕ_s returned by fits to pseudo-experiments.

4.9.3. Case 3: $\Delta\Gamma_s$ Constrained by $\Delta\Gamma_s^{SM}|\cos(\phi_s)|$

In the case where ϕ_s is not equal to zero, $\Delta\Gamma_s$ is expected to be reduced by the factor of $|\cos(\phi_s)|$ compared to its SM value $\Delta\Gamma_s^{SM}$ [**18**]. The third column of Table 4.9 shows the results of a fit with $\Delta\Gamma_s$ constrained by this expected behavior. For a comparison with the previous untagged study performed at DØ (Ref. [**46**]), tagging information was ignored in this case. A comparison of these studies is presented in Appendix D. The

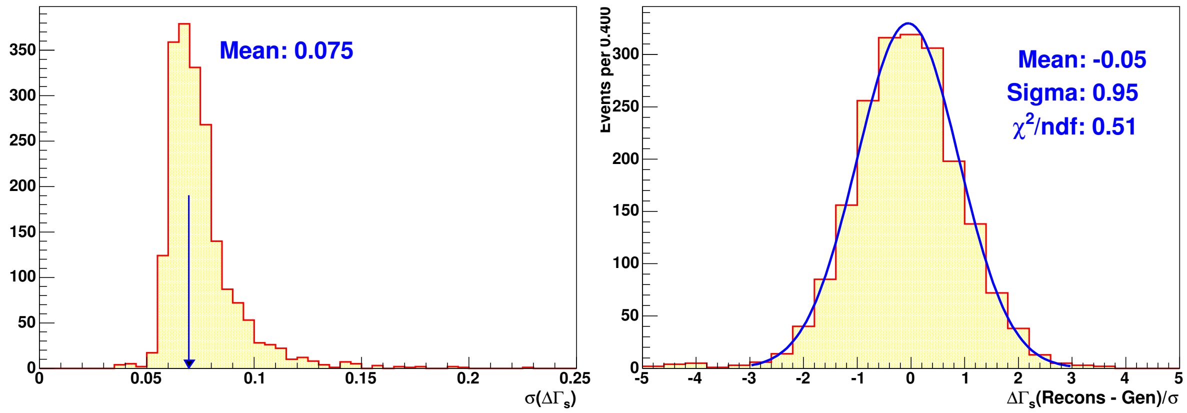

Figure 4.23. The distribution of error (left) and pull (right) for $\Delta\Gamma_s$ returned by fits to pseudo-experiments.

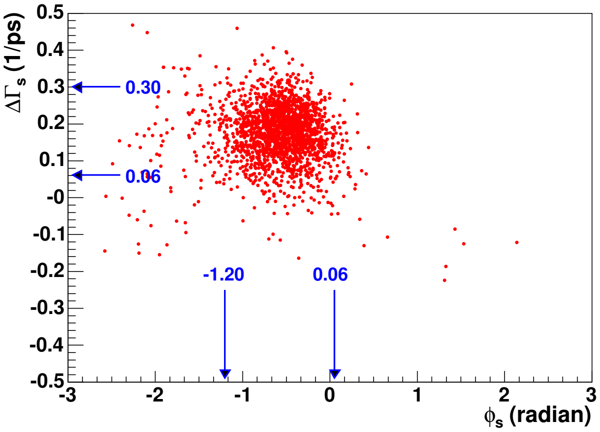

Figure 4.24. The scatter plot of the fitted values of the $\Delta\Gamma_s$ and ϕ_s for an ensemble of simulated experiments.

results for this fit are found to be consistent with the results obtained by Ref. [**46**], and are listed in the third column in Table 4.9.

4.9.4. Fit Projections

The fit projections on the proper decay length distribution for events in the signal mass region $(5.26 - 5.46)$ GeV/c^2 are shown in Fig. 4.27 (left). The fit projections on the transversity $(\cos\theta)$ angle distribution for signal dominated events (mass window $(5.26 -$

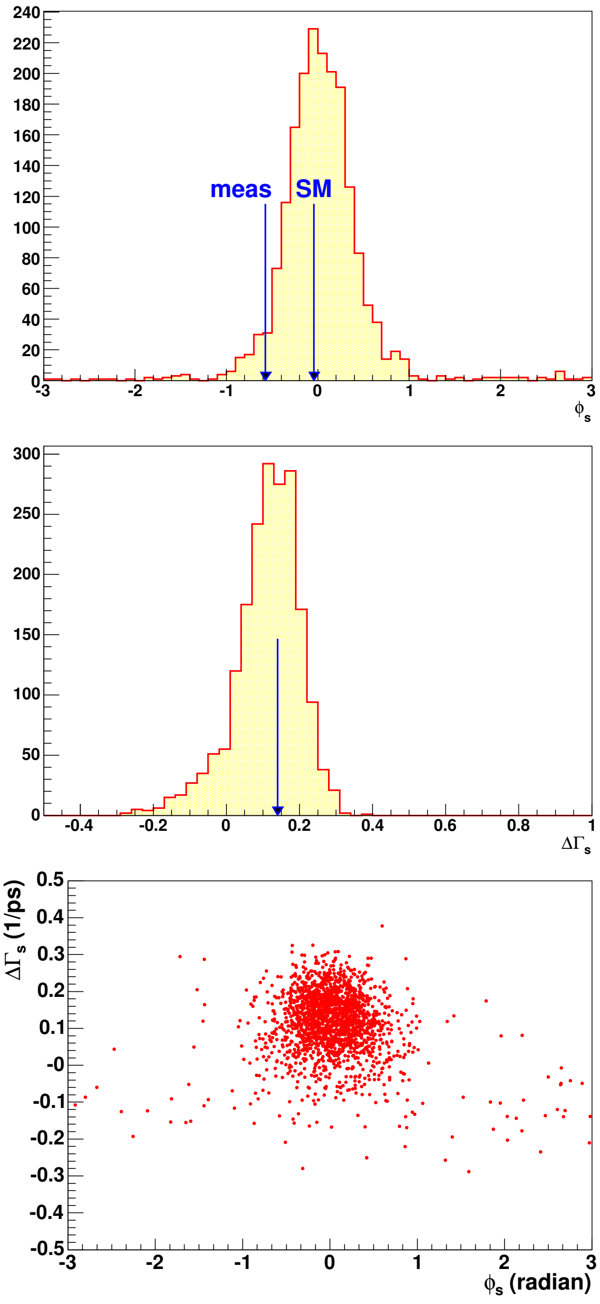

Figure 4.25. Results of an ensemble test under the hypothesis $\phi_s = -0.04$, $\Delta\Gamma_s = 0.14$ ps^{-1}. Top: The distribution of ϕ_s. With the measured value of -0.57, the P-value for the SM hypothesis is 5%. Middle: $\Delta\Gamma_s$. Bottom: The scatter plot of the fitted values of the $\Delta\Gamma_s$ and ϕ_s for the same ensemble.

5.46) GeV/c^2 and ct/$\sigma(ct) > 5$) are shown in Fig. 4.27 (right). The fit projections on the φ and $\cos\psi$ angle distributions for signal dominated events are shown in Fig. 4.28.

4.9.5. Comparisons

Table 4.12 shows the consistency of results obtained for two subsamples: One with positive flavor tag values ($\mathcal{D} > 0$) and one with negative values.

	$\mathcal{D} > 0$	$\mathcal{D} < 0$
$\bar{\tau}_s$ (ps)	1.59±0.08	1.40±0.08
$\Delta\Gamma_s$ (ps^{-1})	0.14±0.10	0.25±0.10
$A_\perp(0)$	0.43±0.06	0.40±0.05
$\|A_0(0)\|^2 - \|A_{\|\|}(0)\|^2$	0.37±0.06	0.29±0.07
δ_1	-0.40±0.50	-0.70±0.44
δ_2	2.96±0.50	3.25±0.41
ϕ_s	0.02 ± 0.42	-0.93 ± 0.30
ΔM_s (ps^{-1})	$\equiv 17.77$	$\equiv 17.77$

Table 4.12. Comparison of the likelihood fit results for positive and negative flavor tags.

A plot showing a comparison of results for ϕ_s obtained for various fits is shown in Fig. 4.29. Starting from the top, the first line corresponds to the default fit letting ϕ_s be free, as described in 4.9.1. The next two lines show the result for positive tag ($\mathcal{D} > 0$) and negative tag ($\mathcal{D} < 0$) variables. The next line shows the case using only the opposite-side lepton tag. The next lines shows the result when the strong phases $\delta_1(\delta_2)$ are fixed to $0(\pi)$. The next two lines are the case when the z coordinate of the vertex is negative (positive). The next two show the results for Run IIa and Run IIb data separately. Next is the case for unconstrained δ_1 and δ_2. Finally the result from the "untagged" fit is shown. The vertical line at -0.04 indicates the SM prediction.

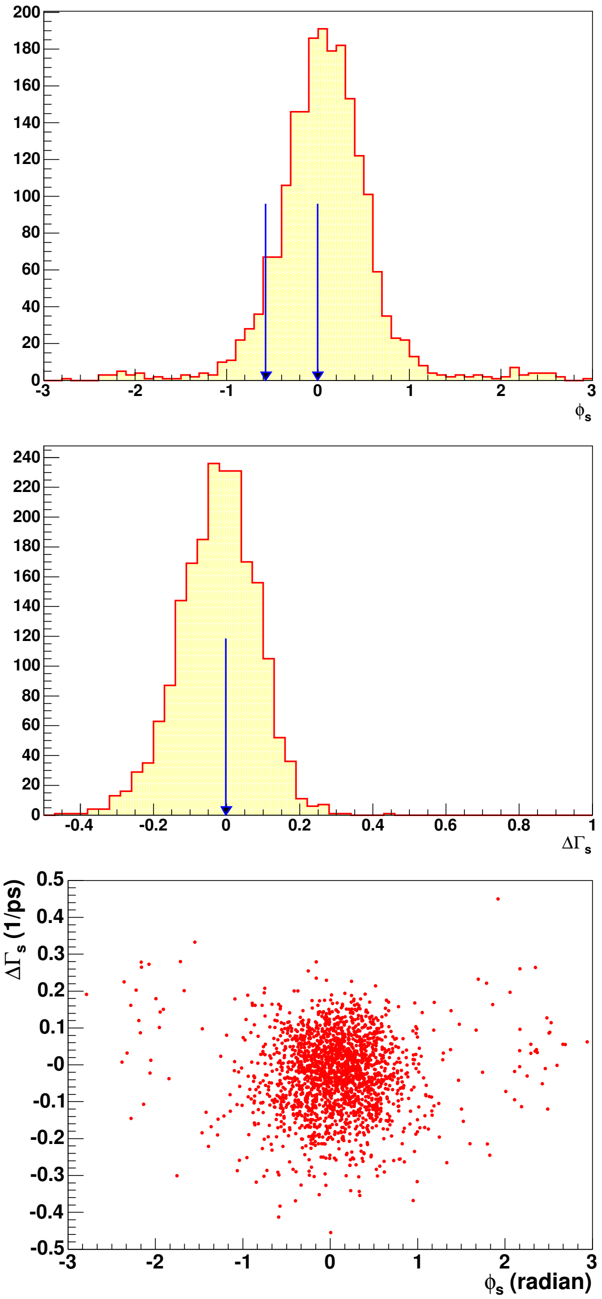

Figure 4.26. Results of an ensemble test under the hypothesis $\phi_s = 0$, $\Delta\Gamma_s = 0$. Top: The distribution of ϕ_s. Middle: The distribution of $\Delta\Gamma_s$. The probability of obtaining the measured value equal or higher than the DØ result, 0.19 ps^{-1}, is 2%. Bottom: The scatter plot of the fitted values of the $\Delta\Gamma_s$ and ϕ_s for the same ensemble.

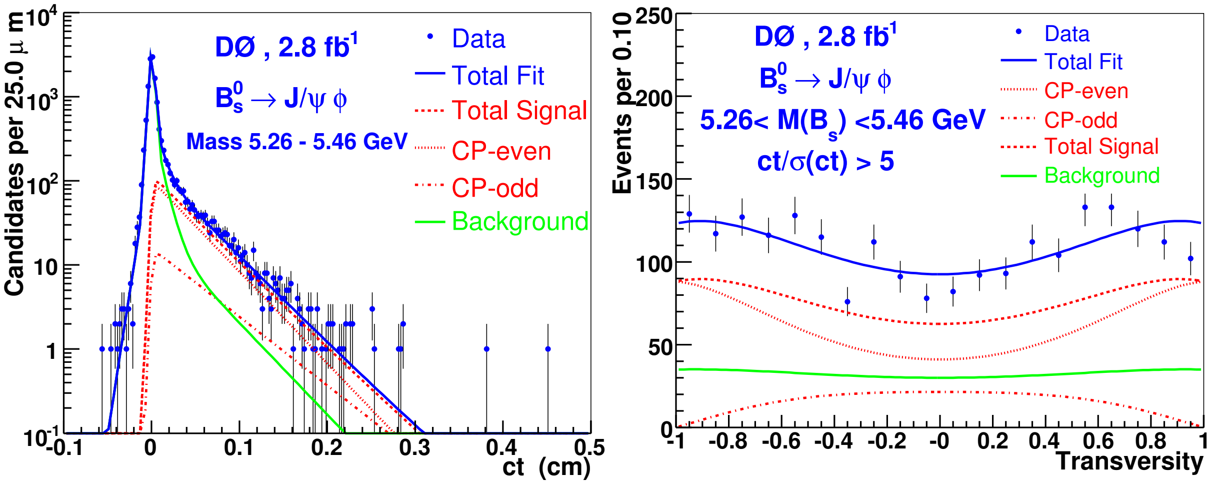

Figure 4.27. Left: The proper decay length, ct, of the B_s^0 candidates for the signal mass region. Right: The transversity distribution for the signal-enhanced subsample: "non-prompt" and signal mass region. The curves show: the signal contribution, dotted(red); the background, light solid (green); and total, solid(blue).

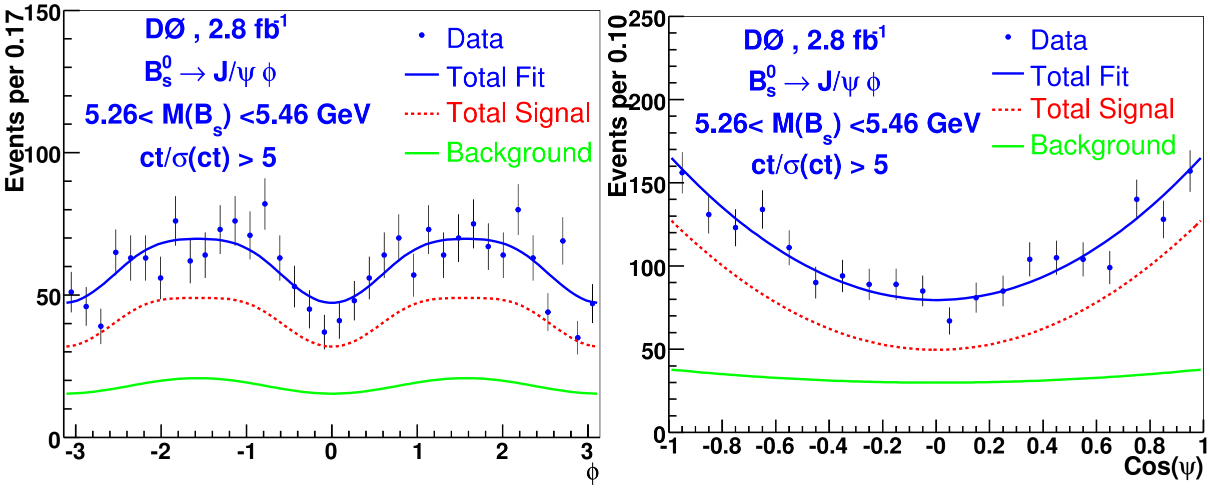

Figure 4.28. Left: The distribution in the angle φ for the signal-enhanced subsample: "non-prompt" and signal mass region. Right: The distribution in the angle $\cos\psi$ for the signal-enhanced subsample: "non-prompt" and signal mass region. The curves show: the signal contribution, dotted(red); the background, light solid (green); and total, solid(blue).

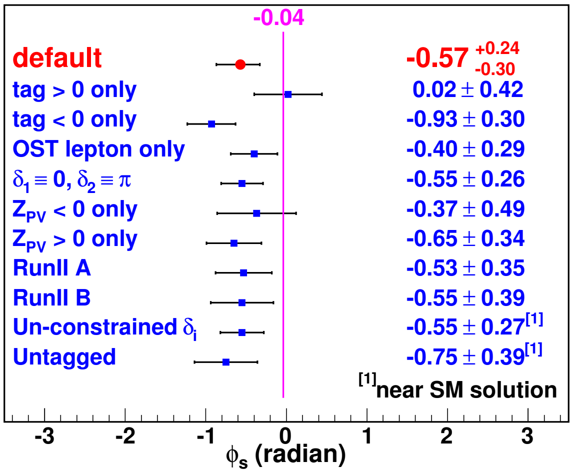

Figure 4.29. Comparison of fit results for ϕ_s for various fits. From above, the first line corresponds to the default fit, followed by $\mathcal{D} > 0$, $\mathcal{D} < 0$, opposite-side lepton tag only, $\delta_1(\delta_2)$ fixed to $0(\pi)$, the z coordinate of the vertex negative (positive), Run IIa (Run IIb) data, and “untagged” fit. Note the sign ambiguity for the latter. The vertical line at -0.04 indicates the SM prediction.

4.10. Systematic Uncertainties

Systematic uncertainties must be taken into account in this study to account for possible sources of error. The sources of systematic uncertainty relevant in this study are presented here.

The first source of systematic uncertainty comes from the limited detector fiducial volume and the kinematic cuts applied to enhance the signal shape and acceptance of the signal as a function of the three decay angles (θ, φ, and ψ). In this study, the acceptance is parameterized as a product of the acceptance in each of the three decays angles, obtained from the weighted MC (MC distributions corrected by a weight derived by forcing the match between the J/ψ p_T distribution in data and MC).

A factorized approximation is used in this study as the default approach, shown in the first column of Table 4.9. The real acceptance in the 3-angle space may deviate from this approach. For instance, the acceptance as a function of the transversity azimuthal angle φ may depend on the polar angle θ. To quantify the sensitivity of the physics results to the acceptance parameterization, the maximum likelihood fits were repeated for two cases: (a) The acceptance distribution described as a uniform function of φ. (b) The acceptance distribution described as an exaggerated shape obtained by setting the parameters to two times the default values. The fit results for these two cases are shown in Table 4.13. The systematic uncertainty is taken as half the difference between (a) and (b) due to the acceptance shape. The effects are small compared to the statistical uncertainties.

A rigorous treatment of the acceptance as a function of the three angles would require allowing for a nonfactorized three-angle background. Background, especially its prompt component, is expected to be independent of the angles, and any apparent dependence in the accepted sample may be due to the acceptance effects. By allowing for a deviation of the background angular distribution from a factorized form, a negligible effect on the physics parameters is found in this study.

	Acceptance alternative a	alternative b
$\bar{\tau}_s$ (ps)	1.517±0.06	1.521±0.06
$\Delta\Gamma_s$ (ps^{-1})	0.187±0.07	0.192±0.07
$A_\perp(0)$	0.419±0.04	0.409±0.04
$\|A_0(0)\|^2 - \|A_{\|\|}(0)\|^2$	0.366±0.05	0.307±0.04
δ_1	-0.488 ± 0.42	-0.544 ± 0.45
δ_2	3.167±0.39	3.180±0.43
ϕ_s	$-0.561^{+0.24}_{-0.30}$	$-0.571^{+0.24}_{-0.30}$
ΔM_s (ps^{-1})	$\equiv 17.77$	$\equiv 17.77$

Table 4.13. Summary of the likelihood fit results for two alternative shapes of the acceptance as a function of the angle ϕ.

A single Gaussian function is used to describe the signal mass distribution in this study. Alternatively, a sum of two Gaussian functions was used to describe the distribution. The shape was obtained from a high-statistics MC study with the width ratio of the two components equal to 2.2 and the weights equal to 0.35 and 0.65. The two Gaussian signal parameterization gives an improved mass fit (KS probability 47%) and a higher signal yield (2090 ± 68 events). The physics results using this approach remain stable, therefore the contribution to the total systematic uncertainty is negligible.

Effects of the imperfect knowledge of the tagging dilution are estimated by varying the dilution parameterization of Eq. (4.12) by $\pm 1\sigma$.

Unlike the signal, the background time evolution is not expected to have a significant oscillatory behavior. Possible effects on the ϕ_s measurement from the B_s^0 decays to CP eigenstates, passing the criteria for $J/\psi\phi$ candidates, are estimated by adding an oscillatory term with frequency of Δm_s to the long-lived background. Assuming the presence of CP-even (CP-odd) only states, constituting the overall fraction as large as $f_s = 0.2$ of the total long-lived background, the variation in ϕ_s is found to be less than 0.01 (all other fit results remain unchanged). The real effect on ϕ_s is likely to be considerably smaller. A B_s^0 decay to another channel, interpreted as $B_s^0 \to J/\psi\phi$, and contributing to the mass distribution, has a mismeasured p_T and proper lifetime. The resulting oscillations are additionally diluted.

The "interference" term in the background model accounts for the collective effect of various physics processes. However, its presence may be partially due to the detector acceptance effects.

Finally, the difference between fits with and without including an "interference" term and a "long lived background oscillations" term are associated with the background model.

A summary of contributions to systematic uncertainties is given in Table 4.14.

Source	$\bar{\tau}_s$ ps	$\Delta\Gamma_s$ ps^{-1}	$A_\perp(0)$	$\lvert A_0(0)\rvert^2 - \lvert A_{\vert\vert}(0)\rvert^2$	ϕ_s
Acceptance	±0.003	±0.003	±0.005	±0.03	±0.005
signal mass model	-0.01	$+0.006$	-0.003	-0.001	-0.006
Flavor tagging	±0.001	±0.001	±0.001	±0.001	±0.01
Background model	$+0.003$	$+0.02$	-0.02	-0.01	$+0.02$
Δm_s input	±0.01	±0.001	±0.001	±0.001	$+0.06, -0.01$
Total	±0.01	$+0.02, -0.01$	$+0.01, -0.02$	±0.03	$+0.07, -0.02$

Table 4.14. Sources of systematic uncertainty in the results of the study of the decay $B_s^0 \to J/\psi\phi$.

CHAPTER 5

Summary

This chapter provides a summary of the main results obtained in this study of CP violation in the B_s^0 system at the DØdetector. The measurement of the width difference $\Delta\Gamma_s$ and CP-violating phase ϕ_s in the B_s^0 system provides a good test of the CKM mechanism in the SM and a probe for new physics. In the SM, the two physical eigenstates B_s^L and B_s^H (known as the "Light" and "Heavy" mass eigenstates) are not the same as the flavor eigenstates B_s^0 and $\bar{B}_s^0$ and are expected to have sizeable mass and width differences. Assuming the CP-violating phase is small ($\phi_s^{SM} = -0.04$), the mass eigenstates are also expected to be CP eigenstates. These results were published in Physical Review Letters [**4**].

The decay amplitude of $B_s^0 \to J/\psi\phi$ is written in terms of time dependent linear polarization states of the J/ψ and ϕ vector mesons, which have well defined CP states. The time-dependent angular analysis of the decay $B_s^0 \to J/\psi(\mu^+\mu^-)\phi(K^+K^-)$ in the transversity basis provides an elegant means for separating the CP-even and CP-odd components. Once the CP components are separated, their lifetimes can be determined and the width difference, $\Delta\Gamma_s = \Gamma_L - \Gamma_H$, between the mass eigenstates can be measured. With a sizeable width difference, there is sensitivity to the CP-violating phase through interference terms between the CP-even and CP-odd states.

This analysis uses 48047 flavor tagged B_s^0 candidates obtained from a 2.8 fb^{-1} data sample collected by the DØ Run II detector at Fermilab. B_s^0 candidates were reconstructed in the decay chain $B_s^0 \to J/\psi(\mu^+\mu^-)\phi(K^+K^-)$. A flavor tag was applied to the sample to determine the initial state of the B_s^0 meson candidates. From a maximum likelihood fit to the time-dependent angular distribution of the flavor-tagged decays $B_s^0 \to J/\psi\phi$, the following measurements were made: The average lifetime of the B_s^0–$\bar{B}_s^0$ system was measured to be $\bar{\tau}(B_s^0) = 1.52 \pm 0.05 \pm 0.01$ ps. The width difference between the light and heavy B_s^0 eigenstates was measured to be $\Delta\Gamma_s = 0.19 \pm 0.07(\text{stat})^{+0.02}_{-0.01}(\text{syst})\ \text{ps}^{-1}$. Finally, the CP-violating phase was measured to be $\phi_s = -0.57^{+0.24}_{-0.30}(\text{stat})^{+0.07}_{-0.02}(\text{syst})$. Another solution, with $\Delta\Gamma_s < 0$, was also found in this study and determined to be disfavored by a likelihood ratio of 1:29. The magnitude of the decay amplitudes were also measured. In the maximum likelihood fits, the oscillation frequency was set to $\Delta m_s = 17.77\ \text{ps}^{-1}$, as measured in Ref. [**41**]. In addition, a Gaussian constraint was imposed on the strong phases allowing them to deviate by a width of $\pi/5$ from the values $\delta_1 = -0.46$ and $\delta_2 = 2.92$, as measured in Ref. [**42**]. The allowed 90% C.L. intervals of $\Delta\Gamma_s$ and of ϕ_s are $0.06 < \Delta\Gamma_s < 0.30\ \text{ps}^{-1}$ and $-1.20 < \phi_s < 0.06$. The SM hypothesis for ϕ_s has a P-value of 6.6%. Finally, assuming the standard model scenario (fixing ϕ_s at -0.04), the results are $\Delta\Gamma_s = 0.14 \pm 0.07(\text{stat})^{+0.02}_{-0.01}(\text{syst})\ \text{ps}^{-1}$, $\bar{\tau}(B_s^0) = 1.53 \pm 0.06 \pm 0.01$ ps.

This measurement is in agreement with a similar measurement recently performed by the CDF Collaboration at the Tevatron [**47**]. Using a 2.8 fb^{-1} data set, and assuming the SM predictions for the width difference and CP-violating phase, CDF determines the probability of a deviation as large as the level observed in their data to be 7%, corresponding to a 1.8σ deviation. Interestingly, this deviation is seen in the same direction as the results reported in the DØ analysis analysis.

The Tevatron is expected to operate until the year 2010, and DØ expects to collect data totalling up to 8 fb^{-1}. With the full available data set, in addition to further improvements in flavor tagging and signal selection techniques, DØ expects an enhancement in the sensitivity to the CP-violating parameter ϕ_s.

References

[1] H. Goldstein, C. Poole, J. Safko, *Classical Mechanics Third Edition*, San Fransisco, California: Addison Wesley, (2002).

[2] A.D. Sakharov: *Violation of CP Symmetry, C-Asymmetry and Baryon Asymmetry of the Universe*, Pisma Zh. Eksp. Teor. Fiz. 5: 32-35 (1967); JETP Lett. 5: 24-27 (1967).

[3] M. Kobayashi, T. Maskawa, *CP Violation in the Renormalizable Theory of Weak Interaction*, Prog. Theor. Phys. 49, 652 (1973).

[4] *Measurement of the B_s^0 mixing parameters from the flavor-tagged decay $B_s^0 \rightarrow J/\psi\phi$*, V. M. Abazov *et al.*, Phys. Rev. Lett. **101** 241801 (2008); arXiv:08022255 [hep-ex].

[5] C. Amsler et al., Physics Letters B667, 1 (2008).

[6] J.H. Christensen et al., Phys. Rev. Lett. 13, 138 (1964).

[7] S.W. Herb et al., *Observation of a Dimuon Resonance at 9.5 Gev in 400-GeV Proton-Nucleus Collisions*, Phys. Rev. Lett. 39 (1977).

[8] D. Griffiths, *Introduction to Elementary Particles*, Heppenheim, Germany: Wiley-VCH, (2004).

[9] *B Physics at the Tevatron: Run II and Beyond*, Fermilab-Pub-01/197 (2001).

[10] R. Waldi, *Lectures on Flavour Oscillation and CP Asymmetry in B Meson Decays*, Maria Lach Herbstschule 1997, TUD-IKTP/97/03.

[11] L. Wolfenstein, Phys. Rev. Lett. 51 1945 (1983).

[12] R. Aleksan, B. Kayser and D. London, Phys. Rev. Lett.73181994.

[13] Heavy Flavor Averaging Group (HFAG), *Averages of b-hadron Properties at the end of 2007*, [arXiv:0808.1297v1 [hep-ex]].

[14] A. G. Grozin, *Introduction to the Heavy Quark Effective Theory*, hep-ph/9908366.

[15] B. Grinstein, *An Introduction to Heavy Mesons*, hep-ph/9508227.

[16] Isard Dunietz, *B_s–$\bar{B}_s$ Mixing, CP Violation and Extraction of CKM Phases from Untagged Bs Data Samples*, hep-ph/9501287.

[17] Y. Nir and D. Silverman, Nucl. Phys. **B345**, 301 (1990).

[18] I. Dunietz, R. Fleischer, U. Nierste, *In Pursuit of New Physics with B_s Decays*, [hep–ph/0012219]

[19] A. Dighe, I. Dunietz, H. Lipkin, J. Rosner, Phys. Lett. **B369**, 1996 (p. 144-150).

[20] A. S. Dighe, I. Dunietz, and R. Fleischer, *Extracting CKM Phases and B_s – $\bar{B}_s$ Mixing Parameters from Angular Distributions of Non-Leptonic B Decays*, hep-ph/9804253.

[21] Particle Data Group (see webpage http://pdg.lbl.gov).

[22] Fermi National Accelerator Laboratory (see webpage http://www.fnal.gov/).

[23] V. Shiltsev, *Status of Tevatron Collider Run II and Novel Technologies for Luminosity Upgrades*, in: Proc. 2004 European Particle Accelerator Conference, Lucern, Switzerland, Vol. 1, 2004, p. 239.

[24] D0 Collaboration, V.M. Abazov *et al.* Nucl. Instrum. Methods Phys. Res. A **565**, 463 (2006).

[25] DØ Collaboration, *The Upgraded DØ Detector*, physics/0507191.

[26] R. Yarema, et al., Fermilab-TM-1892 (1994, revised 1996).

[27] J. Brzenziak, et al., Fermilab-TM-1886 (1994).

[28] B. Squires, et al., *Design of the 2 Tesla Superconducting Solenoid for the Fermilab DØ Detector Upgrade*, in: P. Kittel, et al. (Eds.), Advances in Cryogenic Engineering, Plenum Press, New York, New York, 1994, p. 301.

[29] B. Acharya, et al., Nucl. Instrum. Methods Phys. Res. A 401 (1997) 45.

[30] R. D. Fields, *The Sources of b-Quarks at the Tevatron and their Correlations*, Phys. Rev. D **65**, (2002).

[31] The CDF Collaboration, *Measurement of b-quark fragmentation fractions in $p\bar{p}$ collisions at $\sqrt{s} = 1.8$ TeV*, Phys. Rev. Lett. **84**, p.1663 – 1668, (2001).

[32] BANA package (see webpage http://www-d0.fnal.gov/Run2Physics/ckm/d0_private/bgv/aa/bana.htm).

[33] A. Ryd, D. Lange, http://www.slac.stanford.edu/˜lange/ EvtGen/

[34] H. U. Bengtsson and T. Sjostrand, Comp. Phys. Comm. **46**, 43 (1987).

[35] J. Abdallah et al., DELPHI Collaboration, Eur. Phys. J. **C32**, 185 (2004).

[36] W. M. Yao *et al.* (Particle Data Group), J. Phys. G **33**, 1(2006) (URL:http://pdg.lbl.gov).

[37] D0 Collaboration, V. Abazov *et al.*, Phys. Rev. **D74**, 112002 (2006).

[38] OPAL Collaboration, R. Akers *et al.*, Z. Phys. **C 66**, 19 (1995).

[39] "ROOT, An Object Oriented Data Analysis Framework" see `http://root.cern.ch/`.

[40] "MINUIT, Function Minimization and Error Analysis" see `http://wwwasdoc.web.cern.ch/wwwasdoc/minuit/minmain.html`.

[41] CDF Collaboration, hep-ex/0606027.

[42] E. Barberio et al., Heavy Flavor Averaging Group, http://arxiv.org/abs/0704.3575, page 153.

[43] M. Suzuki, hep-ph/0106354.

[44] BaBar Collaboration, hep-ex/0607081.

[45] A. Lenz, and U. Nierste, hep-ph/0612167.

[46] D0 Collaboration, V. M. Abazov et al., *Lifetime difference and CP-violating phase in the B_s^0 system*. Phys. Rev. Lett. **98**, 121801 (2007).

[47] *First Flavor-Tagged Determination of Bounds on Mixing Induced CP Violation in $B_s^0 \to J/\psi\phi$ Decays*, T. Aaltonen *et al.*, Phys. Rev. Lett. **100** 161802 (2008); arXiv:0712.2397v1 [hep-ex].

APPENDIX A

Data and MC Signal Matching

A.1. Background-subtracted p_T Distributions in the Central Region

The following seven figures show the background-subtracted p_T distributions of the leading and trailing muon, J/ψ, ϕ, B_s^0, and leading and trailing kaon, in the central region ($|\eta| < 1$) after applying the weight factor derived by forcing an agreement between the J/ψ p_T spectra in data and MC.

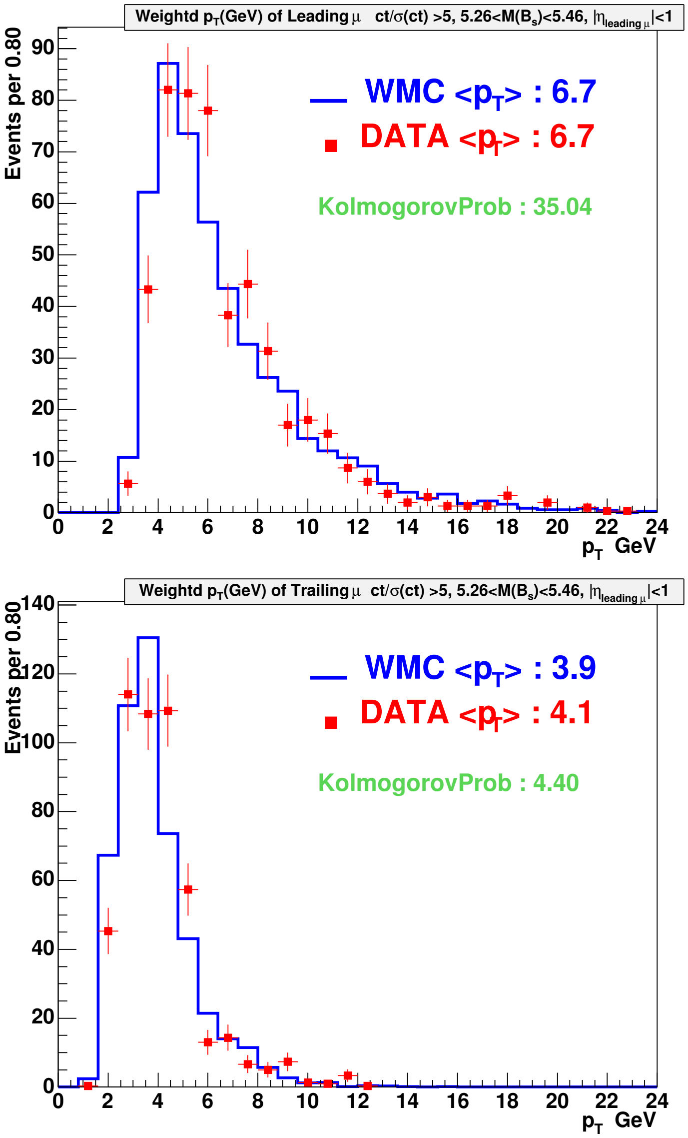

Figure A.1. p_T distribution of the leading muon (top) and the trailing muon (bottom), in the central rapidity region, in data (points) and MC (solid histogram).

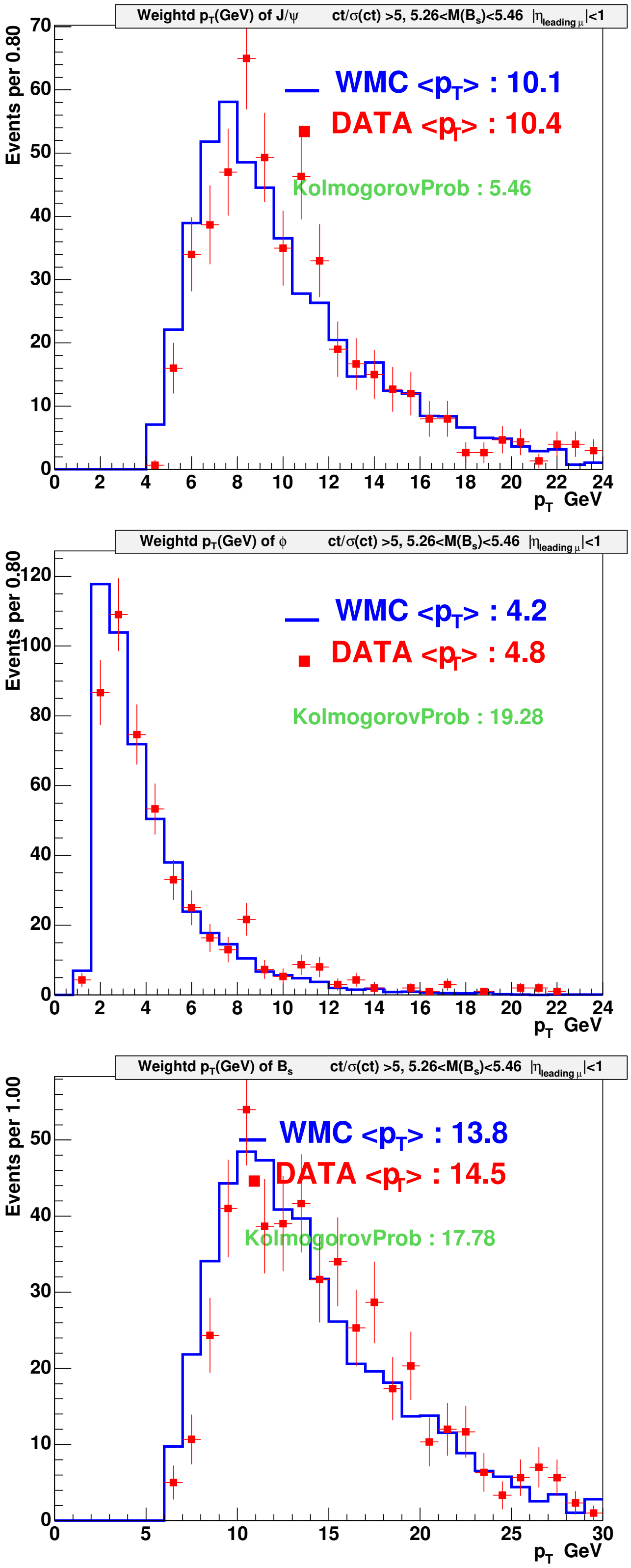

Figure A.2. p_T distribution of J/ψ (top), ϕ (middle), and B_s^0 (bottom), in the central rapidity region, in data (points) and MC (solid histogram).

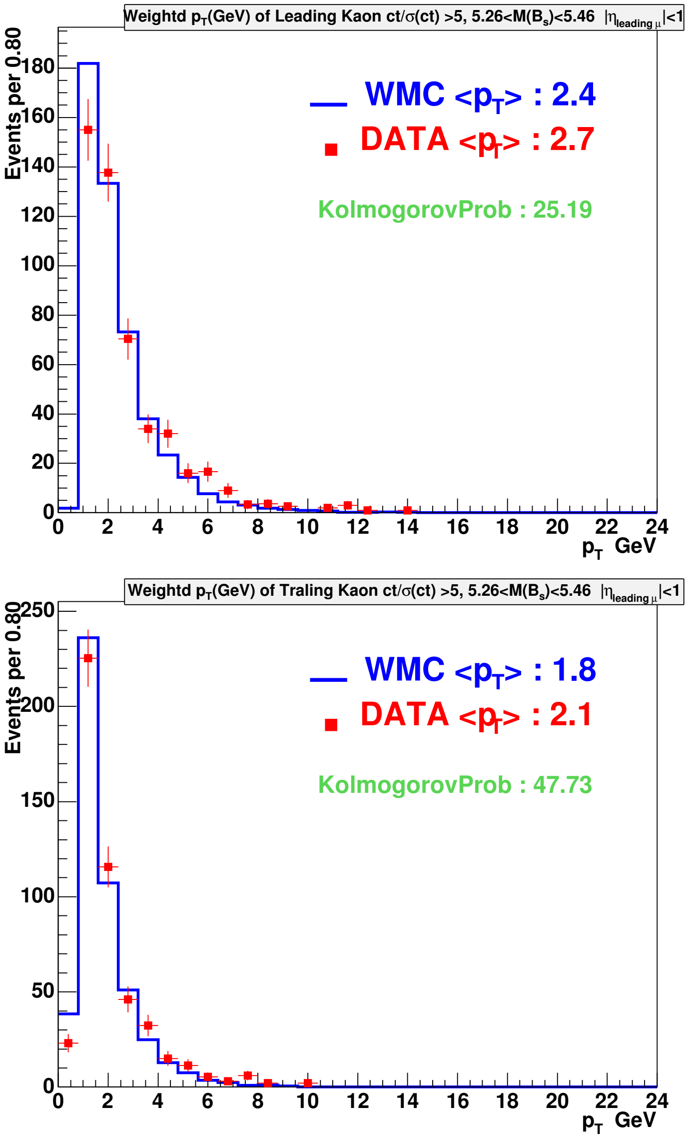

Figure A.3. p_T distribution of the leading kaon (top) and the trailing kaon (bottom), in the central rapidity region, in data (points) and MC (solid histogram).

A.2. Background-subtracted p_T Distributions in the Forward Region

The following seven figures show the background-subtracted p_T distributions of the leading and trailing muon, J/ψ, ϕ, B_s^0, and leading and trailing kaon, in the forward region ($|\eta| > 1$) after applying the weight factor derived by forcing an agreement between the J/ψ p_T spectra in data and MC.

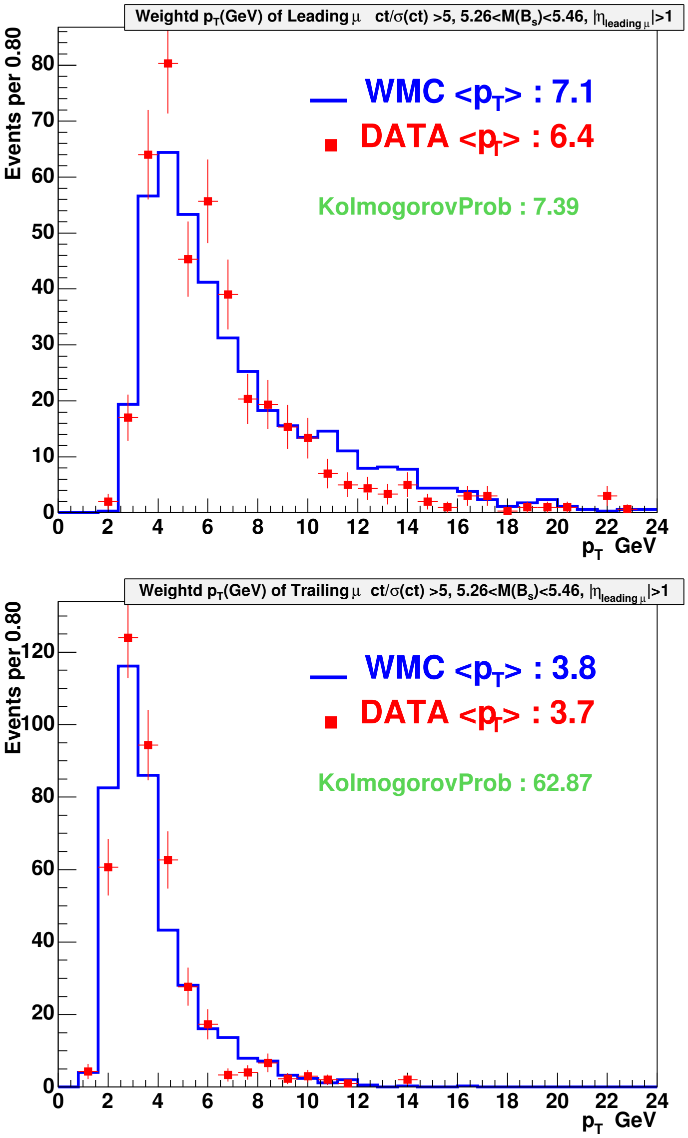

Figure A.4. p_T distribution of the leading muon (top) and the trailing muon (bottom), in the forward rapidity region, in data (points) and MC (solid histogram).

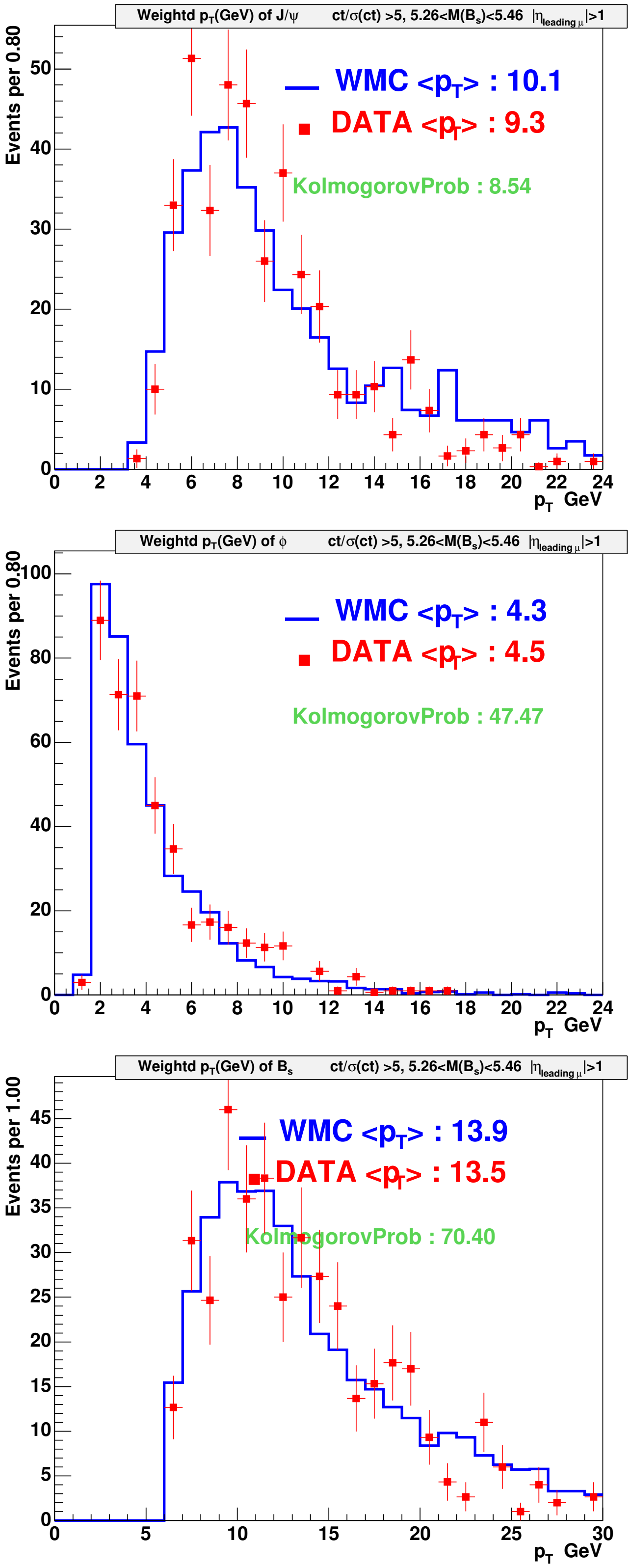

Figure A.5. p_T distribution of J/ψ (top), ϕ (middle), and B_s^0 (bottom), in the forward rapidity region, in data (points) and MC (solid histogram).

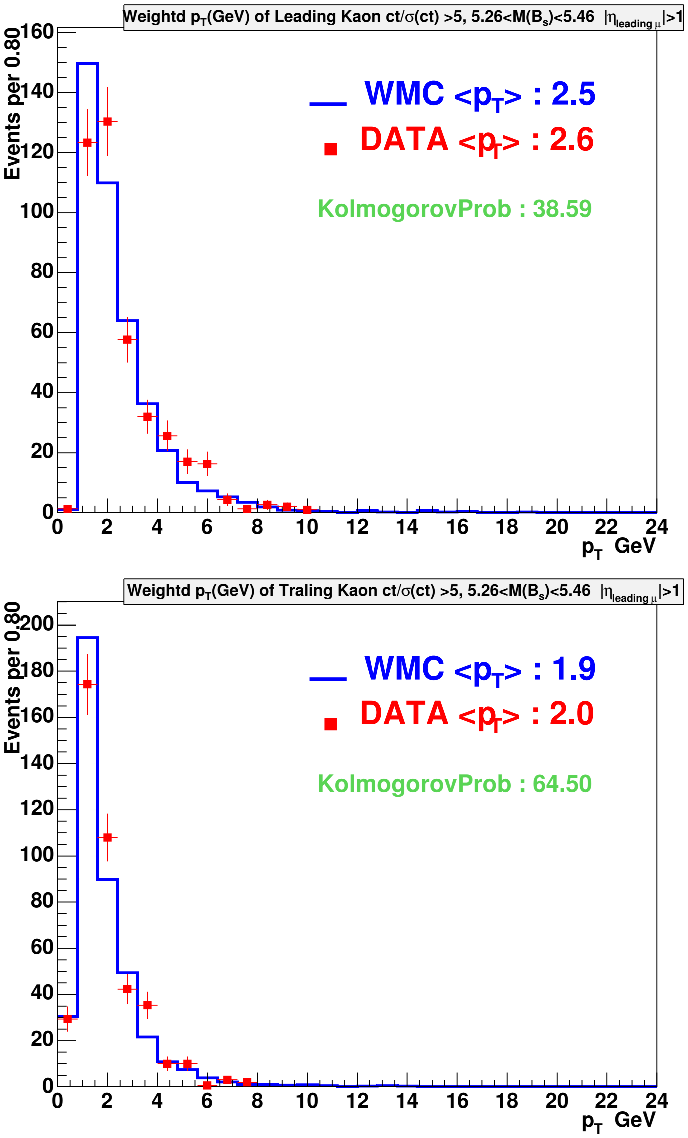

Figure A.6. p_T distribution of the leading kaon (top) and the trailing kaon (bottom), in the forward rapidity region, in data (points) and MC (solid histogram).

A.3. Background-subtracted p_T Distributions in the Central Region for Run IIa and RunIIb Separately

The following fourteen figures show the background-subtracted p_T distributions of the leading and trailing muon, J/ψ, ϕ, B_s^0, and leading and trailing kaon, in the central region ($|\eta| < 1$) after applying the weight factor derived by forcing an agreement between the J/ψ p_T spectra in data and MC for the Run IIa and Run IIb data separately.

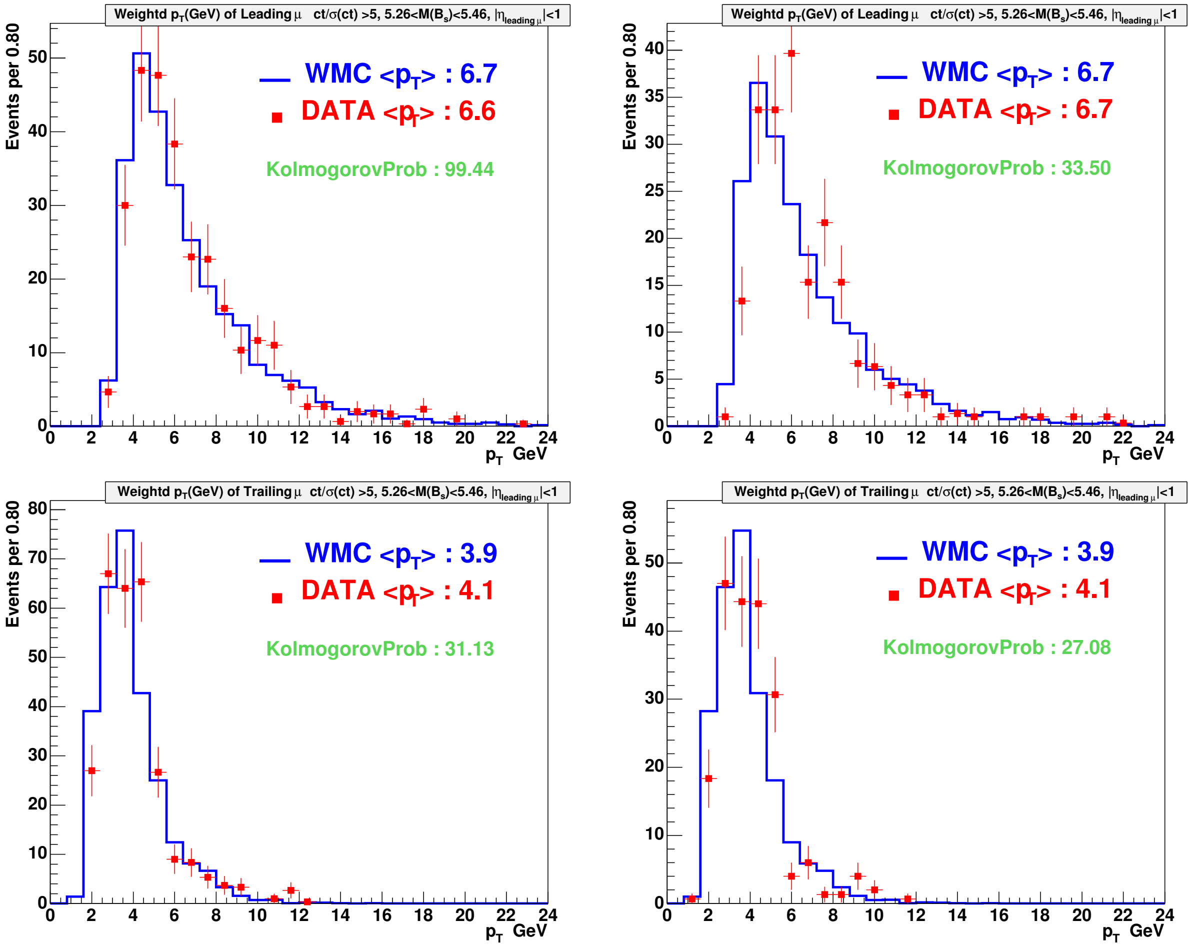

Figure A.7. p_T distribution of the leading muon (top) and the trailing muon (bottom), in the central rapidity region, in data (points) and MC (solid histogram) for the Run IIa data (left) and Run IIb data (right).

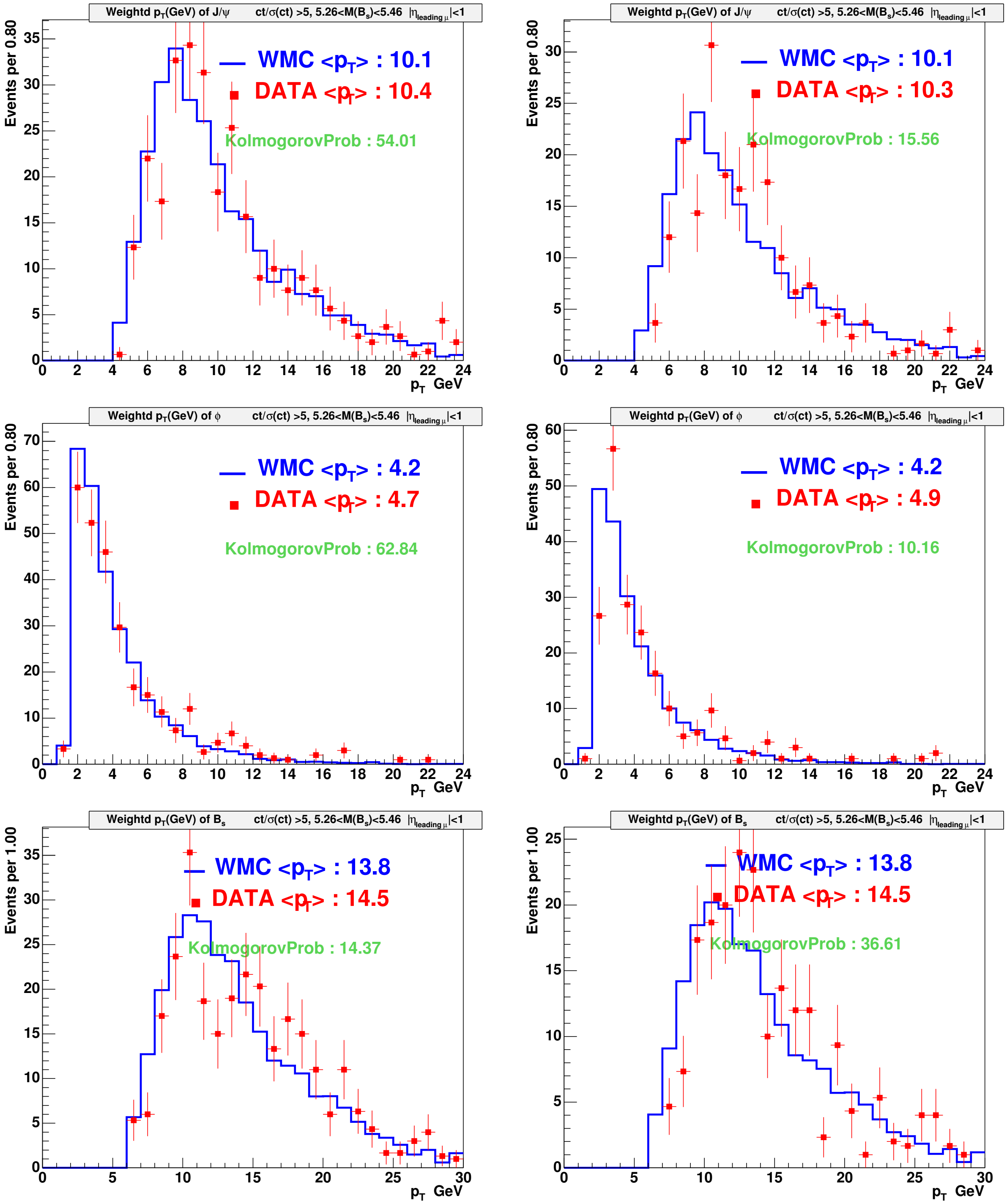

Figure A.8. p_T distribution of J/ψ (top), ϕ (middle), and B_s^0 (bottom), in the central rapidity region, in data (points) and MC (solid histogram), for the Run IIa data (left) and Run IIb data (right).

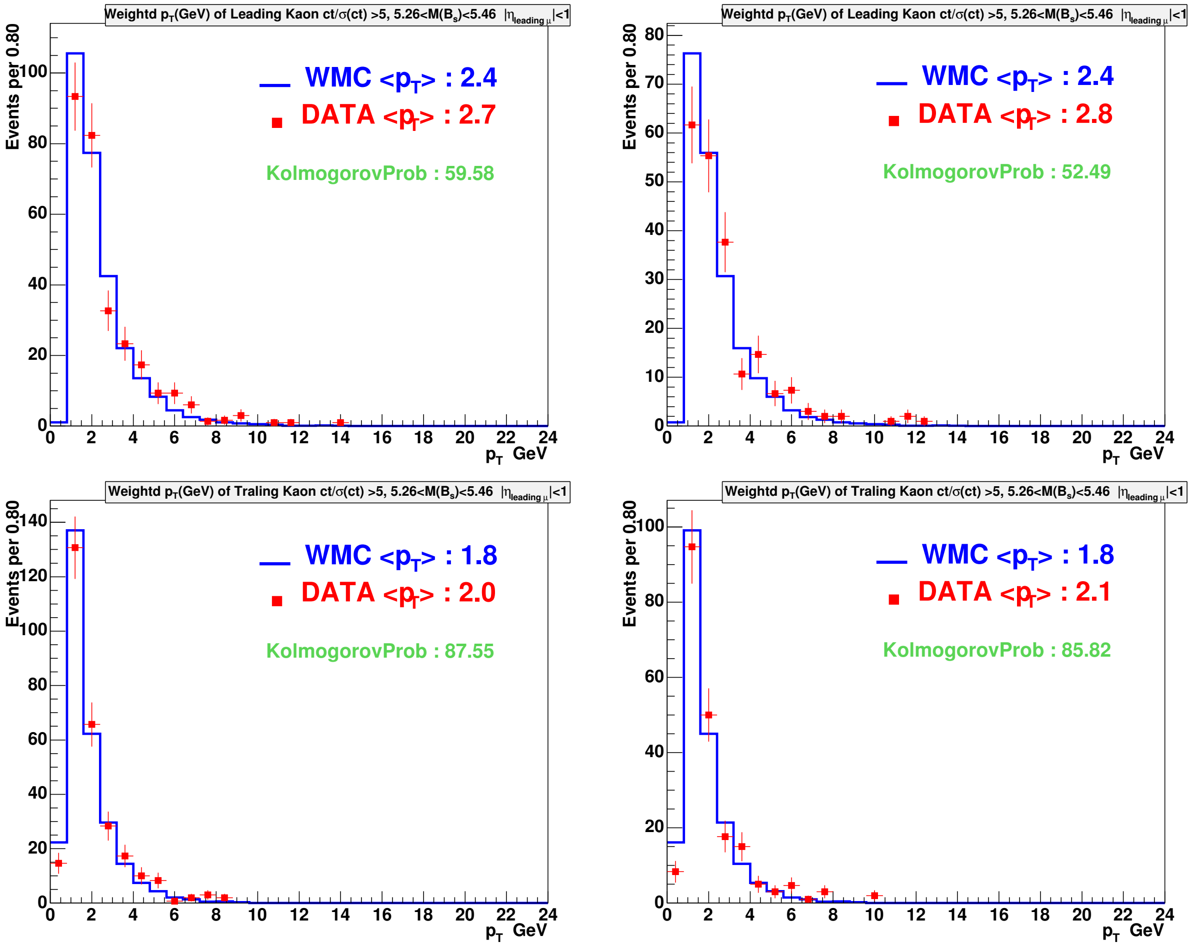

Figure A.9. p_T distribution of the leading kaon (top) and the trailing kaon (bottom), in the central rapidity region, in data (points) and MC (solid histogram), for the Run IIa data (left) and Run IIb data (right).

A.4. Background-subtracted p_T Distributions in the Forward Region for Run IIa and RunIIb Separately

The following fourteen figures show the background-subtracted p_T distributions of the leading and trailing muon, J/ψ, ϕ, B_s^0, and leading and trailing kaon, in the forward region ($|\eta| > 1$) after applying the weight factor derived by forcing an agreement between the J/ψ p_T spectra in data and MC for the Run IIa and Run IIb data separately.

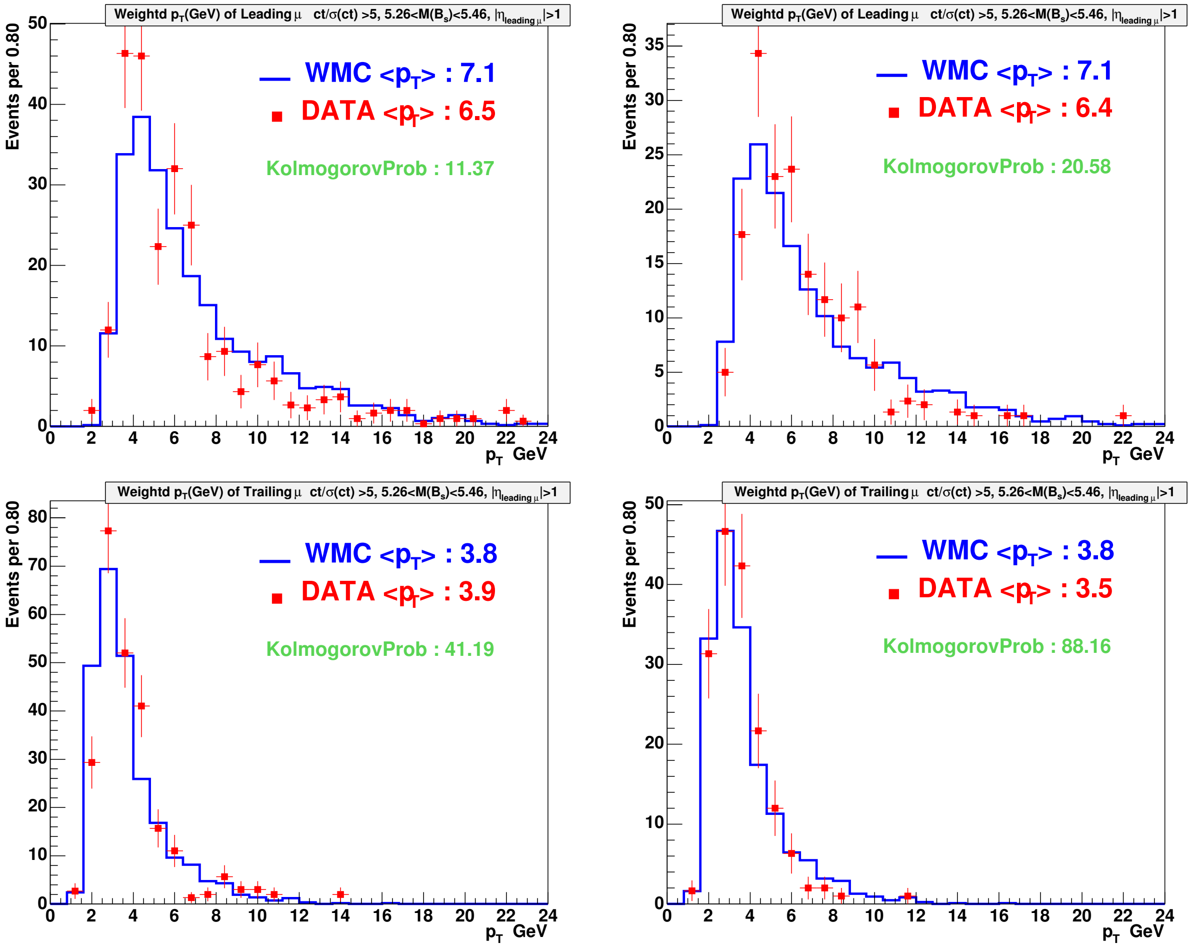

Figure A.10. p_T distribution of the leading muon (top) and the trailing muon (bottom), in the forward rapidity region, in data (points) and MC (solid histogram), for the Run IIa data (left) and Run IIb data (right).

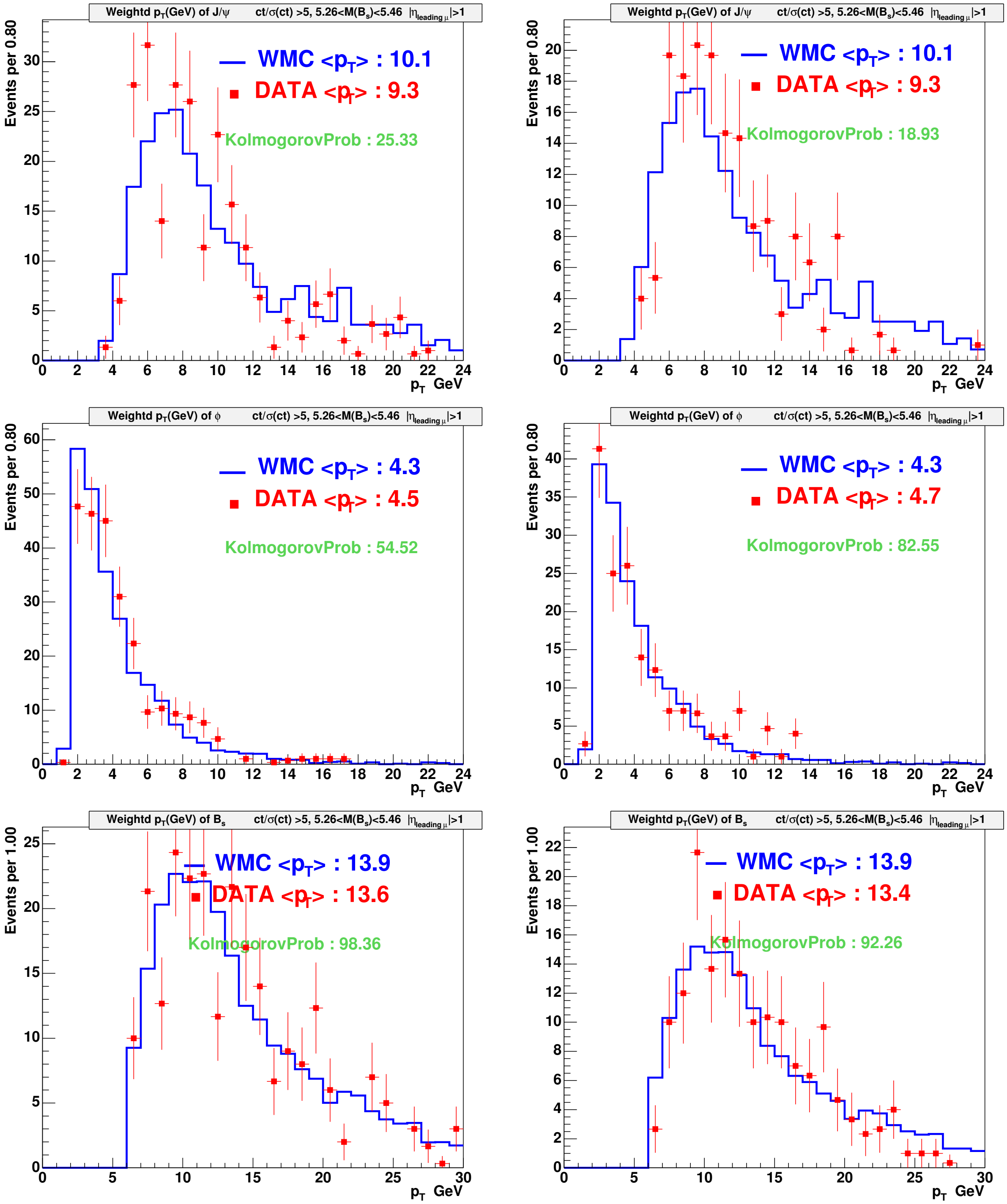

Figure A.11. p_T distribution of J/ψ (top), ϕ (middle), and B_s^0 (bottom), in the forward rapidity region, in data (points) and MC (solid histogram) for the Run IIa data (left) and Run IIb data (right).

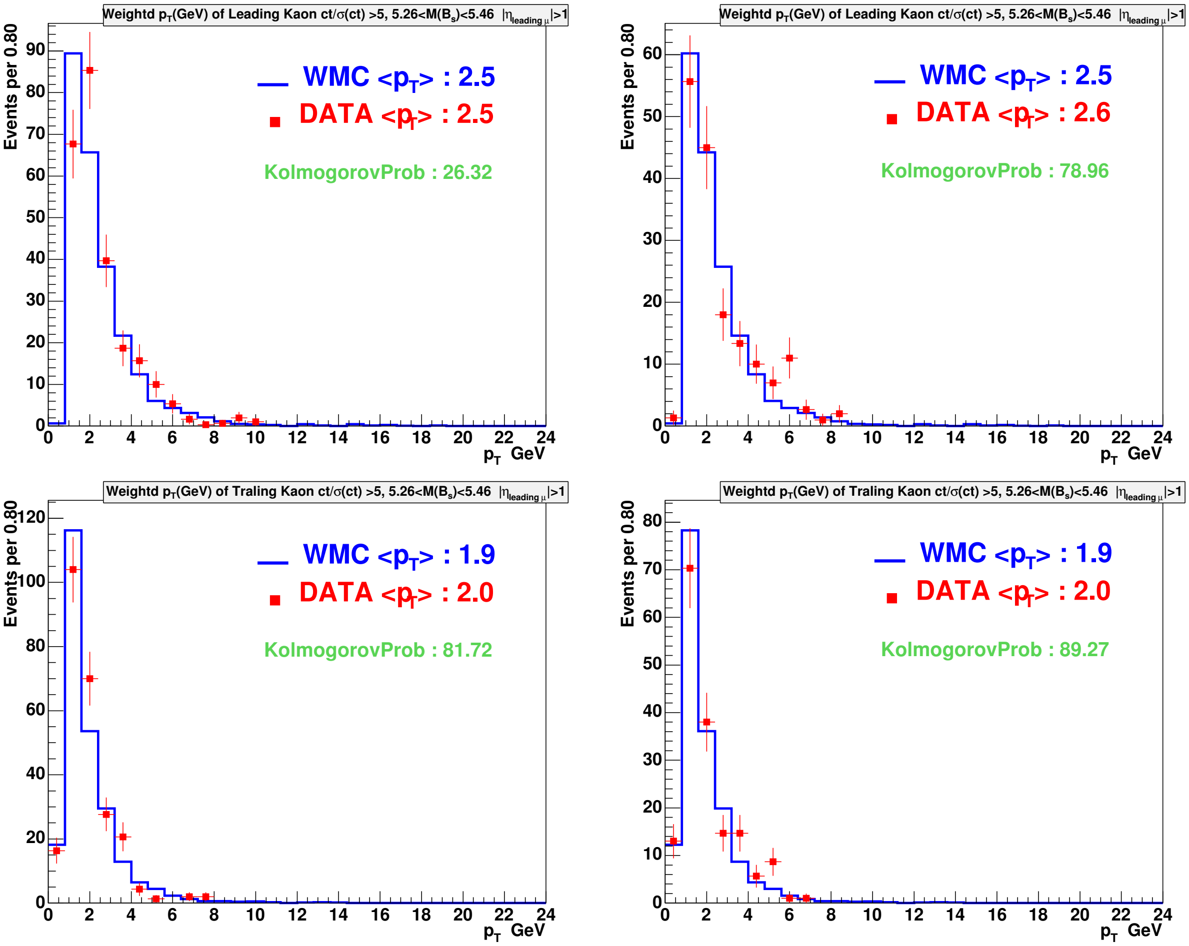

Figure A.12. p_T distribution of the leading kaon (top) and the trailing kaon (bottom), in the forward rapidity region, in data (points) and MC (solid histogram) for the Run IIa data (left) and Run IIb data (right).

APPENDIX B

Study of the Cut on $\sigma(ct)$

Table B.1 compares the results of the default fit (same as the 1st column in Table 4.9) and the results of the fit with the cut on $\sigma(ct)$ lowered from 0.006 cm to 0.0035 cm and raised to 0.01 cm. The results are found to be stable, and the measurement uncertainties are comparable to the default results found when ϕ_s is free.

	$\sigma(ct) < 0.006$ cm	$\sigma(ct) < 0.0035$ cm	$\sigma(ct) < 0.01$ cm
$\bar{\tau}_s$ (ps)	1.52±0.05	1.53±0.05	1.52±0.05
$\Delta\Gamma_s$ (ps^{-1})	0.19±0.07	0.22±0.07	0.19±0.06
$A_\perp(0)$	0.41±0.04	0.41±0.04	0.43±0.04
$\|A_0(0)\|^2 - \|A_{\|\|}(0)\|^2$	0.34±0.05	0.37±0.05	0.34±0.04
δ_1	-0.52±0.42	-0.53±0.41	-0.53±0.37
δ_2	3.17±0.39	3.22±0.39	3.18±0.32
ϕ_s	-0.57±0.27	-0.57±0.25	-0.57±0.27
Δm_s (in ps^{-1})	$\equiv 17.77$	$\equiv 17.77$	$\equiv 17.77$

Table B.1. Comparison of the likelihood fit results for $\sigma(ct) < 0.006$ cm (default), $\sigma(ct) < 0.0035$ cm and for $\sigma(ct) < 0.01$ cm.

APPENDIX C

Angular Probability Distribution Function Normalization

We start with the time-dependent angular distribution decay rate function:

$$\frac{d^3\Gamma(t)}{d\cos\theta\ d\varphi\ d\cos\psi} = Norm\Big\{|A_0(t)|^2 \quad TT^1_{\psi\varphi\theta} \quad + |A_\parallel(t)|^2 \quad TT^2_{\psi\varphi\theta}$$

$$+|A_\perp(t)|^2 \quad TT^3_{\psi\varphi\theta} \quad + Re\{A_0^*(t)A_\parallel(t)\} \quad TT^4_{\psi\varphi\theta}$$

$$+Im\{A_\parallel(t)A_\perp(0)\} \quad TT^6_{\psi\varphi\theta} \quad + Im\{A_0^*(t)A_\perp(t)\} \quad TT^7_{\psi\varphi\theta}\Big\}$$

where,

$$TT^1_{\psi\varphi\theta} = 2\ cos^2\psi\ (1 -\ sin^2\theta\ cos^2\varphi)$$

$$TT^2_{\psi\varphi\theta} =\ sin^2\psi(1 -\ sin^2\theta\ sin^2\varphi)$$

$$TT^3_{\psi\varphi\theta} =\ sin^2\psi\ sin^2\theta$$

$$TT^4_{\psi\varphi\theta} = \frac{1}{\sqrt{2}}\ sin2\psi\ sin^2\theta\ sin2\varphi$$

$$TT^6_{\psi\varphi\theta} = -\ sin^2\psi\ sin2\theta\ sin\varphi$$

$$TT^7_{\psi\varphi\theta} = \frac{1}{\sqrt{2}}\ sin2\psi\ sin2\theta\ cos\varphi$$

$$
\begin{aligned}
|A_0(t)|^2 &= |A_0(0)|^2 \left[\frac{1}{2}\{ \; (1+\cos\phi_s)\, e^{-\Gamma_{\rm L}t} + (1-\cos\phi_s)\, e^{-\Gamma_{\rm H}t} \; \} \mp e^{-\overline{\Gamma}t} \sin(\Delta M_s t) \sin\phi_s \right] \\
|A_\parallel(t)|^2 &= |A_\parallel(0)|^2 \left[\frac{1}{2}\{ \; (1+\cos\phi_s)\, e^{-\Gamma_{\rm L}t} + (1-\cos\phi_s)\, e^{-\Gamma_{\rm H}t} \; \} \mp e^{-\overline{\Gamma}t} \sin(\Delta M_s t) \sin\phi_s \right] \\
|A_\perp(t)|^2 &= |A_\perp(0)|^2 \left[\frac{1}{2}\{ \; (1-\cos\phi_s)\, e^{-\Gamma_{\rm L}t} + (1+\cos\phi_s)\, e^{-\Gamma_{\rm H}t} \; \} \pm e^{-\overline{\Gamma}t} \sin(\Delta M_s t) \sin\phi_s \right]
\end{aligned}
$$

$$
\begin{aligned}
{\rm Re}\{A_0^*(t) A_\parallel(t)\} &= |A_0(0)||A_\parallel(0)| \cos(\delta_2 - \delta_1) \\
&\times \left[\frac{1}{2}\{ \; (1+\cos\phi_s)\, e^{-\Gamma_{\rm L}t} + (1-\cos\phi_s)\, e^{-\Gamma_{\rm H}t} \; \} \mp e^{-\overline{\Gamma}t} \sin(\Delta M_s t) \sin\phi_s \right] \\
{\rm Im}\{A_\parallel^*(t) A_\perp(t)\} &= |A_\parallel(0)||A_\perp(0)| \Big[e^{-\overline{\Gamma}t} \{ \pm \sin\delta_1 \cos(\Delta M_s t) \; \mp \cos\delta_1 \sin(\Delta M_s t) \cos\phi_s \} \\
&+ \frac{1}{2} \left(e^{-\Gamma_{\rm H}t} - e^{-\Gamma_{\rm L}t} \right) \cos\delta_1 \sin\phi_s \Big] \\
{\rm Im}\{A_0^*(t) A_\perp(t)\} &= |A_0(0)||A_\perp(0)| \Big[e^{-\overline{\Gamma}t} \{ \pm \sin\delta_2 \cos(\Delta M_s t) \; \mp \cos\delta_2 \sin(\Delta M_s t) \cos\phi_s \} \\
&+ \frac{1}{2} \left(e^{-\Gamma_{\rm H}t} - e^{-\Gamma_{\rm L}t} \right) \cos\delta_2 \sin\phi_s \Big].
\end{aligned}
$$

If,

$$L^t_{evn} = \frac{1}{2}\{ \; (1+\cos\phi_s)\, GausExp(t, \Gamma_{\rm L}, \sigma_t) + (1-\cos\phi_s)\, GausExp(t, \Gamma_{\rm H}, \sigma_t) \; \}$$

$$L^t_{odd} = \frac{1}{2}\{ \; (1-\cos\phi_s)\, GausExp(t, \Gamma_{\rm L}, \sigma_t) + (1+\cos\phi_s)\, GausExp(t, \Gamma_{\rm H}, \sigma_t) \; \}$$

$$smear \;=\; cos\left(\frac{\Delta_m \sigma_t}{2}\right) \quad for \;\; \Delta_m\sigma_t \le \pi \;\; ; \quad else \; 0$$

$$
\begin{aligned}
NN_S^t &= GausExp(t, \overline{\Gamma}, \sigma_t) * sin\,(\Delta_m t) * smear \\
NN_C^t &= GausExp(t, \overline{\Gamma}, \sigma_t) * cos\,(\Delta_m t) * smear
\end{aligned}
$$

$$
LDET = \frac{1}{2}\{\ GausExp(t, \Gamma_{\rm H}, \sigma_t) - GausExp(t, \Gamma_{\rm L}, \sigma_t)\ \},
$$

then for $B_s^0 \to J/\psi\phi$ decay;

$$
\begin{aligned}
XX_1 = |A_0(t)|^2 &= |A_0(0)|^2 \left[L^t_{evn} - NN_S^t \sin\phi_s\right] \\
XX_2 = |A_\parallel(t)|^2 &= |A_\parallel(0)|^2 \left[L^t_{evn} - NN_S^t \sin\phi_s\right] \\
XX_3 = |A_\perp(t)|^2 &= |A_\perp(0)|^2 \left[L^t_{odd} + NN_S^t \sin\phi_s\right]
\end{aligned}
$$

$$
\begin{aligned}
XX_4 = \mathrm{Re}\{A_0^*(t)A_\parallel(t)\} &= |A_0(0)||A_\parallel(0)|\cos(\delta_2 - \delta_1)\left[L^t_{evn} - NN_S^t \sin\phi_s\right] \\
XX_6 = \mathrm{Im}\{A_\parallel^*(t)A_\perp(t)\} &= |A_\parallel(0)||A_\perp(0)|\Big[\sin\delta_1 NN_C^t\ - \cos\delta_1\cos\phi_s NN_S^t \\
&\quad + LDET\cos\delta_1\sin\phi_s\Big] \\
XX_7 = \mathrm{Im}\{A_0^*(t)A_\perp(t)\} &= |A_0(0)||A_\perp(0)|\Big[\sin\delta_2 NN_C^t\ - \cos\delta_2\cos\phi_s NN_S^t \\
&\quad + LDET\cos\delta_2\sin\phi_s\Big],
\end{aligned}
$$

and for $\overline{B}_s^0 \rightarrow J/\psi\phi$ decay;

$$\begin{aligned}
YY_1 = |A_0(t)|^2 &= |A_0(0)|^2 \left[L^t_{evn} + NN^t_S \sin\phi_s\right] \\
YY_2 = |A_\parallel(t)|^2 &= |A_\parallel(0)|^2 \left[L^t_{evn} + NN^t_S \sin\phi_s\right] \\
YY_3 = |A_\perp(t)|^2 &= |A_\perp(0)|^2 \left[L^t_{odd} - NN^t_S \sin\phi_s\right]
\end{aligned}$$

$$\begin{aligned}
YY_4 = \mathrm{Re}\{A_0^*(t)A_\parallel(t)\} &= |A_0(0)||A_\parallel(0)|\cos(\delta_2-\delta_1)\left[L^t_{evn} + NN^t_S \sin\phi_s\right] \\
YY_6 = \mathrm{Im}\{A_\parallel^*(t)A_\perp(t)\} &= |A_\parallel(0)||A_\perp(0)|\Big[-\sin\delta_1 NN^t_C \; + \cos\delta_1\cos\phi_s NN^t_S \\
&\quad +LDET\cos\delta_1\sin\phi_s\Big] \\
YY_7 = \mathrm{Im}\{A_0^*(t)A_\perp(t)\} &= |A_0(0)||A_\perp(0)|\Big[-\sin\delta_2 NN^t_C \; + \cos\delta_2\cos\phi_s NN^t_S \\
&\quad +LDET\cos\delta_2\sin\phi_s\Big].
\end{aligned}$$

The probability distribution function will be;

$$\begin{aligned}
PDF &= Norm\Big[pBs(XX_1TT^1 + XX_2TT^2 + XX_3TT^3 \\
&\qquad +XX_4TT^4 + XX_6TT^6 + XX_7TT^7) + \\
&\quad (1-pBs)(YY_1TT^1 + YY_2TT^2 + YY_3TT^3 \\
&\qquad +YY_4TT^4 + YY_6TT^6 + YY_7TT^7)\Big].
\end{aligned}$$

To get $Norm$, we first integrate with respect to time, and then for the three angles with Simpson's Rule.

If,

$$L^p_{evn} = \frac{1}{2}\{\ (1+\cos\phi_s)\,\Gamma_{\rm L} + (1-\cos\phi_s)\,\Gamma_{\rm H}\ \}$$
$$L^p_{odd} = \frac{1}{2}\{\ (1-\cos\phi_s)\,\Gamma_{\rm L} + (1+\cos\phi_s)\,\Gamma_{\rm H}\ \}$$

$$smear \;=\; cos\left(\frac{\Delta_m\sigma_t}{2}\right) \quad for\ \ \Delta_m\sigma_t \le \pi \ \ ; \quad else\ 0$$

$$NN_S = smear * \frac{\Delta_m}{\overline{\Gamma}^2 + \Delta_m^2}$$
$$NN_C = smear * \frac{\overline{\Gamma}}{\overline{\Gamma}^2 + \Delta_m^2}$$

$$LDET = \frac{1}{2}\{\ \Gamma_{\rm H} - \Gamma_{\rm L}\ \},$$

then for $B^0_s \to J/\psi\phi$ decay;

$$XX_1 = \int |A_0(t)|^2 \;=\; |A_0(0)|^2\,[L^p_{evn} - NN_S\sin\phi_s]$$
$$XX_2 = \int |A_\parallel(t)|^2 \;=\; |A_\parallel(0)|^2\,[L^p_{evn} - NN_S\sin\phi_s]$$
$$XX_3 = \int |A_\perp(t)|^2 \;=\; |A_\perp(0)|^2\,[L^p_{odd} + NN_S\sin\phi_s]$$

$$\begin{aligned}
XX_4 = \int \mathrm{Re}\{A_0^*(t)A_\parallel(t)\} &= |A_0(0)||A_\parallel(0)|\cos(\delta_2-\delta_1)\,[L_{evn}^p - NN_S\sin\phi_s] \\
XX_6 = \int \mathrm{Im}\{A_\parallel^*(t)A_\perp(t)\} &= |A_\parallel(0)||A_\perp(0)|\Big[\sin\delta_1 NN_C^p \ -\cos\delta_1\cos\phi_s NN_S \\
&\quad +LDET\cos\delta_1\sin\phi_s\Big] \\
XX_7 = \int \mathrm{Im}\{A_0^*(t)A_\perp(t)\} &= |A_0(0)||A_\perp(0)|\Big[\sin\delta_2 NN_C^p \ -\cos\delta_2\cos\phi_s NN_S \\
&\quad +LDET\cos\delta_2\sin\phi_s\Big],
\end{aligned}$$

and for $\overline{B}_s^0 \to J/\psi\phi$ decay;

$$\begin{aligned}
YY_1 = \int |A_0(t)|^2 &= |A_0(0)|^2\,[L_{evn}^p + NN_S\sin\phi_s] \\
YY_2 = \int |A_\parallel(t)|^2 &= |A_\parallel(0)|^2\,[L_{evn}^p + NN_S\sin\phi_s] \\
YY_3 = \int |A_\perp(t)|^2 &= |A_\perp(0)|^2\,[L_{odd}^p - NN_S\sin\phi_s]
\end{aligned}$$

$$\begin{aligned}
YY_4 = \int \mathrm{Re}\{A_0^*(t)A_\parallel(t)\} &= |A_0(0)||A_\parallel(0)|\cos(\delta_2-\delta_1)\,[L_{evn}^p + NN_S\sin\phi_s] \\
YY_6 = \int \mathrm{Im}\{A_\parallel^*(t)A_\perp(t)\} &= |A_\parallel(0)||A_\perp(0)|\Big[-\sin\delta_1 NN_C \ +\cos\delta_1\cos\phi_s NN_S \\
&\quad +LDET\cos\delta_1\sin\phi_s\Big] \\
YY_7 = \int \mathrm{Im}\{A_0^*(t)A_\perp(t)\} &= |A_0(0)||A_\perp(0)|\Big[-\sin\delta_2 NN_C \ +\cos\delta_2\cos\phi_s NN_S \\
&\quad +LDET\cos\delta_2\sin\phi_s\Big].
\end{aligned}$$

Now we integrate following function:

$$pBs(XX_1TT^1 + XX_2TT^2 + XX_3TT^3 + XX_4TT^4 + XX_6TT^6 + XX_7TT^7) +$$
$$(1 - pBs)(YY_1TT^1 + YY_2TT^2 + YY_3TT^3 + YY_4TT^4 + YY_6TT^6 + YY_7TT^7)$$

for the XX_i and YY_i for three angles using Simpson's Rule, which returns the inverse of normalization factor ($\frac{1}{Norm}$).

The acceptance functions are defined as:

$$H(cos\psi) = 1$$

$$F(\varphi) = 1 + Jcos2\varphi + Kcos^2 2\varphi$$

$$G(cos\theta) = 1 + Bcos^2\theta + Ccos^4\theta.$$

Integration with respect to $cos\psi$ will be:

$\int cos^2\psi = \frac{2}{3} \quad ; \quad \int sin^2\psi = \frac{4}{3} \quad ; \quad \int sin2\psi = 0$

$$TT^1_{\varphi\theta} = \int TT^1_{\psi\varphi\theta} = \frac{4}{3}\ (1 - \ sin^2\theta\ cos^2\varphi)$$

$$TT^2_{\varphi\theta} = \int TT^2_{\psi\varphi\theta} = \frac{4}{3}\ (1 - \ sin^2\theta\ sin^2\varphi)$$

$$TT^3_{\varphi\theta} = \int TT^3_{\psi\varphi\theta} = \frac{4}{3}\ sin^2\theta$$

$$TT^4_{\varphi\theta} = \int TT^4_{\psi\varphi\theta} = 0$$

$$TT^6_{\varphi\theta} = \int TT^6_{\psi\varphi\theta} = -\frac{4}{3}\ sin2\theta\ sin\varphi$$

$$TT^7_{\varphi\theta} = \int TT^7_{\psi\varphi\theta} = 0.$$

Integration with respect to φ will be:

$\int \varphi = 2\pi \quad ; \quad \int cos^2\varphi = \int sin^2\varphi = \pi \quad ; \quad \int cos2\varphi = 0 \quad ; \quad \int cos^2 2\varphi = \pi$
$\int cos2\varphi cos^2\varphi = \frac{\pi}{2} \quad ; \quad \int cos^2 2\varphi cos^2\varphi = \frac{\pi}{2}$

$\int F(\varphi) = 2\pi(1 + \frac{K}{2}) \ = 2\pi F_0$
$\int F(\varphi) cos^2\varphi = \pi(1 + \frac{J}{2} + \frac{K}{2}) \ = \pi F_c$
$\int F(\varphi) sin^2\varphi = \pi(1 - \frac{J}{2} + \frac{K}{2}) \ = \pi F_s$
$\int F(\varphi) sin\varphi = 0$

$$TT^1_{\theta} = \int TT^1_{\varphi\theta} = \frac{4\pi}{3}\ (2F_0 - \ sin^2\theta\ F_c)$$

$$TT^2_{\theta} = \int TT^2_{\varphi\theta} = \frac{4\pi}{3}\ (2F_0 - \ sin^2\theta\ F_s)$$

$$TT^3_{\theta} = \int TT^3_{\varphi\theta} = \frac{4\pi}{3}\ 2F_0\ sin^2\theta$$

$$TT^4_{\theta} = \int TT^4_{\varphi\theta} = 0$$

$$TT^6_{\theta} = \int TT^6_{\varphi\theta} = 0$$

$$TT_\theta^7 = \int TT_{\varphi\theta}^7 = 0.$$

Integration with respect to $cos\psi[-1,1]$ will be:

if, $cos\theta = X$

$\int 1 = 2 \quad ; \quad \int X^n = \frac{2}{n+1} \quad if\ n\ is\ even \quad ; \quad \int X^n = 0 \quad if\ n\ is\ odd$

$\int G(X) = 2(1 + \frac{B}{3} + \frac{C}{5}) = 2G_0$ (say)

$\int (1 - X^2) G(X) = 4(\frac{1}{3} + \frac{B}{15} + \frac{C}{35}) = 4G_1$ (say)

$$TT^1 = \int TT_\theta^1 = \frac{16\pi}{3}\ (F_0G_0 - F_cG_1)$$

$$TT^2 = \int TT_\theta^2 = \frac{16\pi}{3}\ (F_0G_0 - F_sG_1)$$

$$TT^3 = \int TT_\theta^3 = \frac{32\pi}{3}\ F_0G_1$$

$$TT^4 = \int TT_\theta^4 = 0$$

$$TT^6 = \int TT_\theta^6 = 0$$

$$TT^7 = \int TT_\theta^7 = 0.$$

For φ distribution:

$$\int TT^1_{\varphi\theta} = TT^1_{\varphi} = \frac{8}{3}\ (G_0 -\ 2G_1\ cos^2\varphi)$$

$$\int TT^2_{\varphi\theta} = TT^2_{\varphi} = \frac{8}{3}\ (G_0 -\ 2G_1\ sin^2\varphi)$$

$$TT^3_{\varphi\theta} = \int TT^3_{\psi\varphi\theta} = \frac{8}{3}\ 2G_1$$

$$TT^4_{\varphi\theta} = \int TT^4_{\psi\varphi\theta} = 0$$

$$TT^6_{\varphi\theta} = \int TT^6_{\psi\varphi\theta} = 0$$

$$TT^7_{\varphi\theta} = \int TT^7_{\psi\varphi\theta} = 0.$$

For $cos\psi$ distribution, integration for $cos\theta$ will be $\int sin2\theta G(\theta) = 0$

$$TT^1_{\psi\varphi} = 4\ cos^2\psi\ (G_0 -\ 2G_1\ cos^2\varphi)$$

$$TT^2_{\psi\varphi} = 2\ sin^2\psi(G_0 -\ 2G_1\ sin^2\varphi)$$

$$TT^3_{\psi\varphi} = 4\ sin^2\psi\ G_1$$

$$TT^4_{\psi\varphi} = \frac{1}{\sqrt{2}}\ 4\ sin2\psi\ G_1\ sin2\varphi$$

$$TT^6_{\psi\varphi} = 0$$

$$TT^7_{\psi\varphi} = 0.$$

Now integrating with respect to ϕ will give: $\int sin2\phi F(\phi) = 0$

$$TT^1_{\psi} = 8\pi\ cos^2\psi\ (F_0G_0 -\ G_1F_c)$$

$$TT^2_{\psi} = 4\pi\ sin^2\psi(F_0G_0 -\ G_1F_s)$$

$$TT^3_{\psi} = 8\pi\ sin^2\psi\ G_1F_0$$

$$TT^4_{\psi} = 0$$

$$TT^6_{\psi} = 0$$

$$TT^7_{\psi} = 0.$$

APPENDIX D

Comparison to Study of Untagged Decays

Table D.1 compares the results of the untagged study of the data presented in this analysis with the results obtained in the untagged study in Ref. [**46**]. In both cases there is a four-fold ambiguity. For an easy comparison, the table presents fit results for the same scenario. The sign convention of Ref. [**18**] is used for both columns. (Note that in Ref. [**46**] an opposite sign convention was used for ϕ_s.) The results of the untagged study of the data presented in this disseration was found to be fully consistent with the results of Ref. [**46**].

	Present data	PRL data
$\bar{\tau}_s$ (ps)	1.49±0.06	1.49±0.08
$\Delta\Gamma_s$ (ps^{-1})	0.18±0.07	0.16 ± 0.09
$A_\perp(0)$	0.43±0.04	0.46±0.06
$\|A_0(0)\|^2 - \|A_{\|\|}(0)\|^2$	0.34±0.05	0.38±0.06
δ_1	-0.62±0.45	-0.45±0.47
δ_2	3.01±0.43	3.07±0.54
ϕ_s	-0.75 ± 0.39	-0.71 ± 0.54

Table D.1. Comparison of the likelihood fit results for the untagged decays for the present data and the data sample used in (Ref. [**46**]).